CENTRO DE INVESTIGACIÓN Y DE ESTUDIOS AVANZADOS DEL INSTITUTO POLITÉCNICO NACIONAL

UNIDAD MÉRIDA

DEPARTAMENTO DE FÍSICA APLICADA

Electronic properties of graphene-based nanostructures: quantum confinement, edge magnetism, and hydrogen adsorption on transition metal cluster-monovacancy systems

Tesis que presenta

Carlos Manuel Ramos Castillo

Para obtener el grado de

Doctor en Ciencias

En Fisicoquímica

Director de tesis: Dr. Romeo de Coss Gómez

Mérida, Yucatán Junio 2016

Dedication

“ To my wife, family, and friends. Whithout whom none of my success would be possible. For their support, encouragement, and patience.”

— Thank you.

Acknowledgements

This research work could not have been done without the support and encouragement from numerous individuals.

First of all, I would like to express my gratitude to my thesis advisory, Dr. Romeo de Coss for his guidance, patience, motivation, and enthusiasm during my PhD studies. He gave me an opportunity and complete freedom to work on novel and interesting research topics. Thanks to my collaborators Dr. Ulises Reveles and Dr. Rajendra Zope who have been a significant support throughout my PhD work. Thanks to my thesis committee: Dr. Geonel Rodríguez, Dr. Oscar Ares, and Dr. Gabriel Merino, for reviewing my thesis and giving their insightful comments. Thanks to Tony, Monse and Zhirnay for all their administrative support. I would also like to thank especially Lalo, Betacho, Guille, Maryel and Pech for being such nice friends. I want to give my deepest appreciation to my whole family and for their support and love. I would like to especially thank the one who brings joy and happiness every day of my life: my wife Conchita.

Thanks to the Texas Advanced Computing Center (TAAC) from the National Science Foundation and NERSC for the computational time. Also, thanks to the High-Performance Supercomputing Center Xiuhcoatl at Cinvestav, México for the computational resources provided. Finally, I like to acknowledge to the CONACYT-México for a graduate scholarship funding.

— Carlos Manuel Ramos Castillo

Abstract

Graphene-based nanostructures has attracted great attention because they provide the opportunity to explore novel structural, electronic, optical, magnetic, and catalytic phenomena. In this way, the study of quantum confinement, edge magnetism and chemical doping of graphene are three of the most fundamental aspects linked by the electronic structure and that must be addressed in order to fill the gap between fundamental science and technological applications. Graphene is a zero bandgap semiconductor. Thus, inducing a gap in graphene is of interest for electronic applications, and quantum confinement in graphene nanostructures can be used to achieve this goal. Another phenomenom strongly linked to electronic structure of nanographene is the edge magnetism. The possibility that carbon materials could exhibit a novel type of *s-p* electron magnetism has attracted much attention over the years. Currently, there is intense discussion about the stability of magnetic order at the zigzag edge of graphene nanostructures. On the other hand, recent studies show that metal-decorated graphene is promising candidate for H_2 storage by combining the low density of carbon materials with the catalytic properties of transition metal atoms. In this thesis, size effects on electronic, optical, and magnetic properties of graphene nanoflakes with zigzag edges are studied using electronic structure calculations based on density functional theory. We found that the inclusion of spin polarization in the calculations for larger zigzag graphene nanoflakes is needed in order to obtain the singlet open-shell ground state. The edge magnetism of graphene nanoflakes with zigzag edges can be stable even at room temperature and have important influence on the size dependence of energy gap and the low-lying optical excitations. However, magnetic edge states do not exhibit influence on the π-plasmons energy in graphene nanoflakes. Furthermore, motivated by the hydrogen storage problem, we provide a detailed study about the adsorption of H_2 on Pd clusters supported on a defective graphene. Our results, about hydrogen adsorption, shows that the Pd clusters supported on graphene monovacancies are able to form dihydrogen complexes, with moderate adsorption energies, within the ideal energy range for efficient hydrogen storage. However, due to the large atomic mass of Pd, the gravimetric content of H_2 is limited to approximately 1%. Clusters of lighter transition metal atoms such as Ni and Ti were also studied. We found that Ti_4 cluster on graphene monovacancy is a promising candidate to increase the H_2 uptake in graphene-based systems. We hope that the findings of this thesis will have important implications in graphene-based materials design for electronics and hydrogen storage technologies.

Resumen

Las nanoestructuras basadas en el grafeno han atraído la atención de la comunidad científica, ya que proporcionan la oportunidad de explorar nuevas propiedades estructurales, electrónicas, ópticas, magnéticas y catalíticas. De esta manera, el estudio de confinamiento cuántico, magnetismo borde y el grafeno dopado químicamente son tres de los aspectos más fundamentales ligados a la estructura electrónica y que deben ser abordados con el fin de llenar la brecha entre la ciencia básica y las aplicaciones tecnológicas. El grafeno es un semiconductor con brecha de energía prohibida igual a cero. Por lo tanto, para considerar al grafeno para su aplicación en dispositivos electrónicos es necesario inducir una brecha de energía, y esto se puede lograr por medio del confinamiento cuaántico en nanoestructuras. Otro fenómeno fuertemente ligado a la estructura electrónica del nanografeno es el magnetismo de borde. La posibilidad de que materiales basados en carbono presenten magnetismo tipo *s-p* ha ocasionado una intensa discusión acerca de la estabilidad del orden magnético en nanoestructuras de grafeno con bordes tipo zigzag. Por otra parte, estudios recientes demuestran que el grafeno decorado con metales de transición es un candidato prometedor para el almacenamiento de hidrógeno debido a que combina la baja densidad del carbono con las propiedades catalíticas de los metales. Por medio de cálculos basados en la teoría del funcional de la densidad estudiamos el efecto del tamaño sobre la propiedades electrónicas, ópticas y magnéticas de nanohojuelas de grafeno con bordes zigzag. Encontramos que el estado base para nanohojuelas de grafeno más grandes es singulete de capa abierta por lo que es necesario incluir la polarización de espín en los cálculos de estructura electrónica. El magnetismo de borde es robusto por lo que es estable a temperatura ambiente, y tiene una fuerte influencia sobre la brecha de energía, pero no sobre la energía de los plasmones π en el espectro óptico. Además, motivados por el problema del almacenamiento de hidrógeno, estudiamos la adsorción de H_2 sobre cúmulos de Pd soportados en grafeno. Los resultados sobre adsorción de hidrógeno, muestran que los cúmulos de Pd soportados sobre vacancias de grafeno forman complejos de dihidrogeno con energias moderadas de adsorción. Sin embargo, el contenido gravimétrico de H_2 está limitado a 1% debido a la masa atómica del Pd. Con el objetivo de incrementar el contenido gravimétrico de H_2, proponemos utilizar cúmulos de metales de transición más ligeros tales como Ti y Ni. Esperamos que nuestros resultados tengan importantes implicaciones en el diseño de materiales basados en grafeno para electrónica y el almacenamiento de hidrógeno.

Contents

List of Tables

List of Figures

Introduction

After the experimental discovery in 2004 of the graphene [1]. This material has been a topic of intense research. Its extraordinary linear dispersion relation in the vicinity of the Fermi level allows the study of relativistic quantum mechanics in a condensed-matter system. The gapless spectrum is beneficial in, for instance, optical applications, as the absorption is nearly constant in the visible spectrum. In the case of transistor applications, however, the absence of a gap leads to poor on-off ratios due to leakgate current. Thus, inducing an energy gap in graphene is of interest for electronics. In this way quantum confinement in graphene nanoestructures can be used to achieve this goal [2–4]. The magnetic edge states in nanographene is other interesting issue that has motivated many studies [7–11]. Despite of theoretical evidence, for many years the stability of the magnetic order on real graphene edges at experimental conditions have been strongly debated. The random orientation of the edges and the influence of the substrate hybridization [10, 11] did not allow edge magnetism in graphene to be properly characterized. However, recently room-temperature magnetic order on well-defined zigzag edges GNRs on Au (111) was reported [11], raising hopes for graphene-based spintronic devices operating under ambient conditions. In similar way to quantum confinement and edge magnetism, the enhancement of catalytic properties of metal-doped graphene for hydrogen storage must be related with its electronic structure. The utilization of molecular hydrogen as energy carrier requires two basic steps to be accomplished, namely hydrogen production and hydrogen storage. The reversible hydrogen storage in appropriate materials or adsorbed on suitable surfaces still requires many issues to be solved before becoming economically viable for all envisioned applications. Carbon materials such as activated carbons [12] metal organic frameworks [13], carbon nanotubes [14], graphite nanofibers [15] and other carbon nanostructures [16, 17] are considered promising candidates in hydrogen storage technology because they have a number of remarkable properties such as high specific surface areas, tunable pore structure, low density, stability for large scale production, and fast kinetics [18] have been studied extensively for hydrogen storage. The big challenge for carbon nanoporous materials as hydrogen storage media is to find a structure with tunable porosity and very high specific surface area, where hydrogen adsorbs strongly enough on the surface as to form a thermodynamically stable arrangement but not too strongly so that reversible fast loading/unloading kinetics are possible [18]. In this way metal-functionalized graphene offers the posibility to enhance the hydrogen adsorption at ambient temperatures.

Graphene nanostructures (nanographene) constitute a new class of chemical compounds which can be used in different fields as diverse as plasmonics, optics, catalysis, hydrogen storage, medicine and biochemistry. The atomic structure of nanographene and its size usually determine their properties and chemical reactivity. Theoretical models like density functional theory, together with efficient computational modelling offer the opportunity to explore the physical and chemical properties of these interesting systems.

Also to understand the effects of parameters such as size, shape, and composition allowing one to derive some general trends. The great progress in the synthesis of metallic and semiconductor graphene nanoflakes (GNFs) enables to obtain samples with well-controlled size and shape for given applications. Computational modelling based on density functional theory offers a useful and complementary approach to experiments since dealing with GNFs does not represent a problem, except for the computational resources, which become significant for quantum mechanical calculations concerning nanostructures in the 1-20 nm range, which are involving hundreds to thousands of atoms. Theoretically, the structural and electronic properties of small GNFs have been previously studied [5]. However, for large GNFs with more than two hundred atoms, the theoretical studies are limited [6].

For these reasons, the present work was focused in the study of the electronic, optical and magnetic properties of graphene nanoflakes with zigzag edges of diferent size (1-7 nm) and shape. Furthermore, motivated by the challenge in developing hydrogen storage materials for practical applications, we provide a detailed description of the interaction of H_2 with atomic and small Pd, Ni, and Ti clusters adsorbed on a defective graphene surface.

In chapter 1 are presented introductory aspects about graphene-based materials, such as synthesis methods, atomic structure, electronic structure, edge magnetism and catalytic properties for hydrogen storage. Chapter 2 presents a brief introduction of the used computational methodologies which are relevant for the calculations in this thesis. In particular, the fundamental concepts about first principles calculations and density functional theory are discussed. Chapter 3 highlights the main results about electronic structure and optical properties for each of the studied nanographene systems, and gives some background from the literature. In Chapter 4, are summarized the main results about magnetic properties of GNFs with different size and shape in the framework of spin-polarized density functional theory and Mulliken population analysis. The results about hydrogen adsorption on metal-functionalized graphene are presented in the Chapter 5. Finally the conclusions, and future prospects are summarized in the last part of the thesis. Complementary information about the. resultsof the studied systems are included three appendices (A,B and C).

Chapter 1

Graphene-Based Materials

1.1 Graphene and its fascinating properties

Since the experimental characterization of its electronic properties in 2004, graphene [1–4] has generated an enormous amount of interest in the condensed matter community. Many extraordinary properties, such as its linear electronic spectrum $E \sim k$ [4], ballistic electronic transport [23], high Young's modulus [24] and excellent thermal conductivity [25], have all been reported. Because of its remarkable properties [2, 26], new applications using graphene in a wide range of areas, including high-speed electronics [27], optical devices [28], energy generation and storage [28, 29], and hybrid materials [30], have all been explored. Andre Geim and Konstantin Novoselov from the University of Manchester won the Nobel Prize in Physics 2010 for groundbreaking experiments regarding the two-dimensional material graphene.

Graphene can be viewed as structural model of other carbon-based materials, such as graphite, nanotubes, fullerenes polyaromatic hydrocarbons, nanoribbons, and even activated carbon. Graphite, the three-dimensional carbon allotrope with a layered structure, has been known for centuries, and is used for a wide scale of applications at the industrial level. Low-dimensional materials based on the same hexagonal carbon network were, discovered only recently. Fullerenes, zero-dimensional spherical carbon cages, were first reported in 1985 [19]. Their discovery was followed in 1991 by that of carbon nanotubes, the quasi-one-dimensional, all-carbon cylinders [20, 21]. Polyaromatic hydrocarbons (PAHs) has been studied by several years due to its toxicity and the ocurrence in the interstellar medium, nanoribbons were studied recently due to transport properties [29], even activated carbons present some of graphitic features in his atomic structure.

Before 2004, many experimentalists created graphene often as an unwanted byproduct in their experiments [42–46]. However, none of studies focussed on the extraordinary properties of graphene. Until 2001 the electronic properties and the potential applications of graphene had not been considered. By 2003 the ideas were fully developed and backed up with compelling scientific evidence that was finally published in 2004 [1].

Graphenes breakthrough came with the production of free-standing graphene flakes by exfoliation from graphite crystals by Novoselov *et al.* [1, 2]. Thus the extraordinary transport properties of graphene were measured in experiment for the first time [1]. Similar measurements to those of Novoselov and co-workers had been performed in the same year for graphene on SiC by Berger and co-workers [47] and nearly at the same time by Zhang and co-workers [41]. The experimental investigation of graphene as the revolutionary strictly two-dimensional material, as it is known nowadays in the scientific community, is

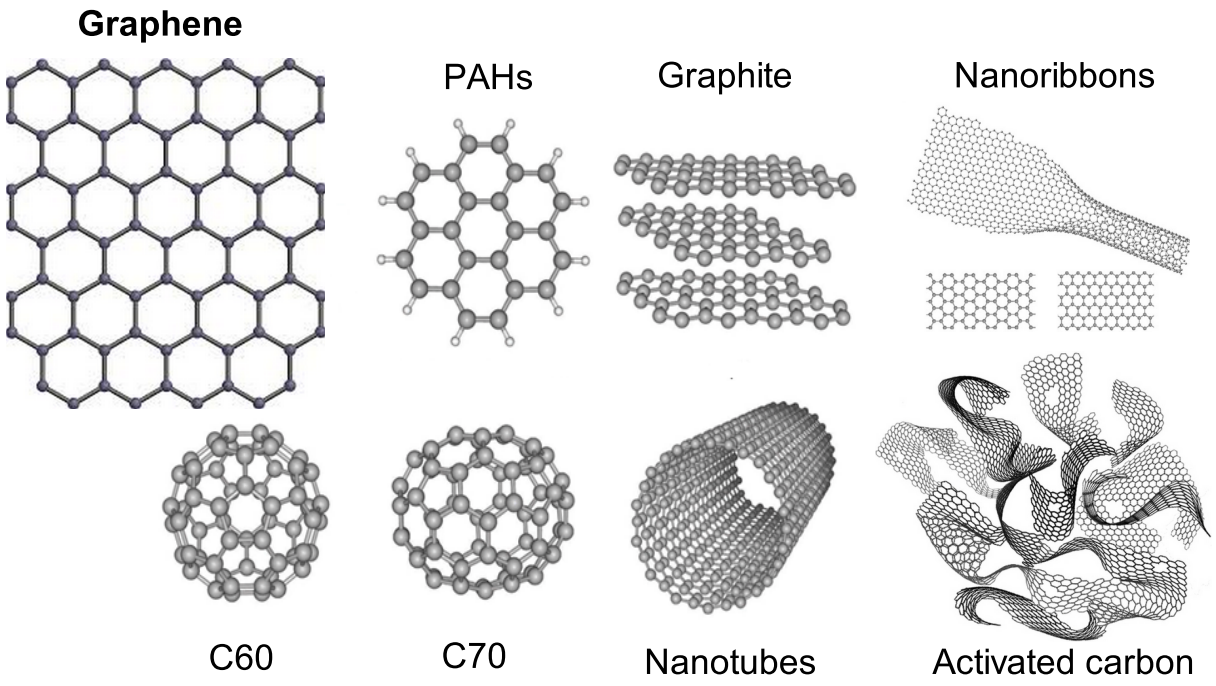

Figure 1.1: Examples of carbon-based materials with graphene-like atomic structure.

often attributed to the extraordinary experimental work of Novoselov and Geim [1, 2].

One of the most interesting aspects of graphene is that its low energy excitations are massless, chiral, Dirac fermions. In neutral graphene, the chemical potential crosses exactly the Dirac point. This particular dispersion, that is only valid at low energies, mimics the physics of quantum electrodynamics (QED) for massless fermions except by the fact that in graphene the Dirac fermions move with a speed v_F which is 300 times smaller than the speed of light, c. Hence, many of the unusual properties of QED can show up in graphene but at much smaller speeds. Dirac fermions behave in very unusual ways when compared to ordinary electrons if subjected to magnetic fields, leading to new physical phenomena [48] such as the anomalous integer quantum Hall effect (IQHE) measured experimentally [41, 49]. Besides being qualitatively different from the IQHE observed in Si and GaAlAs heterostructures devices, the IQHE in graphene can be observed at room temperature because of the large cyclotron energies for pseudo relativistic electrons [4]. In fact, the anomalous IQHE is the trademark of Dirac fermion behavior. Another particularly interesting feature of Dirac fermions is their insensitivity to external electrostatic potentials due to the so-called Klein paradox, that is, the fact that Dirac fermions can be transmitted with probability one through a classically forbidden region [48]. In fact, Dirac fermions behave in a very unusual way in the presence of confining potentials leading to the phenomenon of *zitterbewegung*, or jittery motion of the wavefunction [50].

Graphene is made out of carbon atoms arranged in hexagonal structure as shown in Fig. 1.2. The structure is not a Bravais lattice but can be seen as a triangular lattice with a basis of two atoms per unit cell. The lattice vectors can be written as:

$$\mathbf{a_1} = \frac{a}{2}(3, \sqrt{3})\,, \qquad \mathbf{a_2} = \frac{a}{2}(3, -\sqrt{3})\,, \tag{1.1}$$

where $a = 1.42$ Å is the carbon-carbon distance in graphene [4]. The reciprocal lattice vectors are given by:

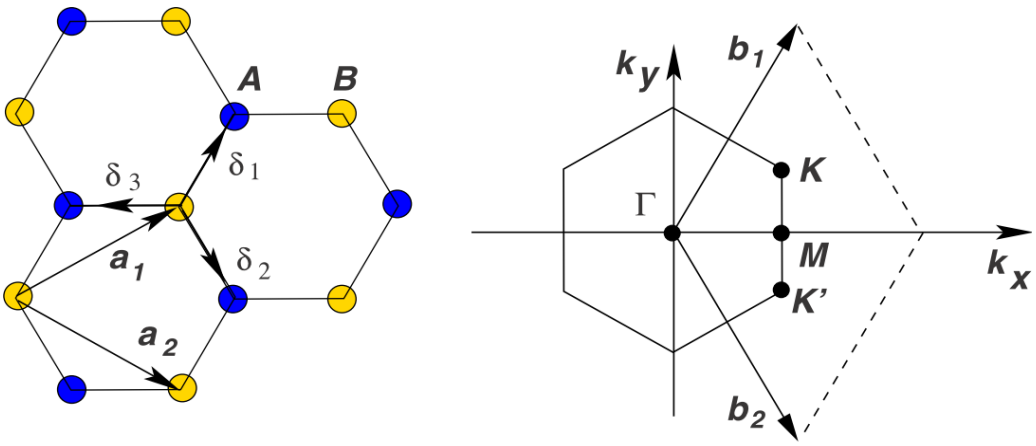

Figure 1.2: Honeycomb lattice and its corresponding Brillouin zone. Left: lattice structure of graphene, made out of two interpenetrating triangular lattices. Right: The corresponding Brillouin zone. The Dirac cones are located at $\mathbf{K}$ and $\mathbf{K}'$. Adapted from reference [4].

$$\mathbf{b_1} = \frac{2\pi}{3a}(1, \sqrt{3})\,, \qquad \mathbf{b_2} = \frac{2\pi}{3a}(1, -\sqrt{3})\,. \tag{1.2}$$

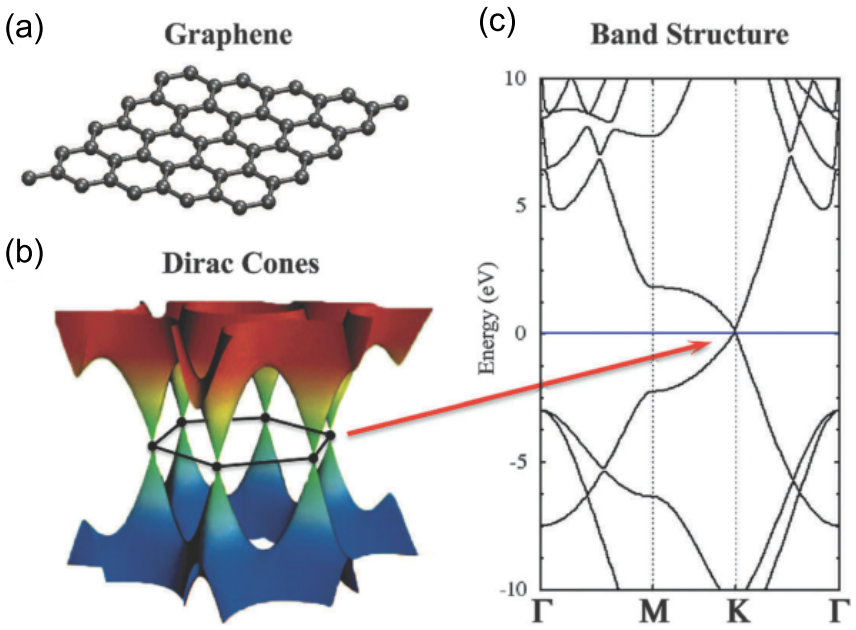

Figure 1.3: Electronic dispersion in the honeycomb lattice. (a) Atomic structure of graphene. (b) Energy spectrum in units of hopping parameter t. (c) Energy bands presenting the Dirac point at the Fermi level. Adapted from reference [51].

Of particular importance to describe the graphene physics are the two points $\mathbf{K}$ and $\mathbf{K}'$ in the graphene Brillouin zone (BZ). These are named Dirac points. Their positions in momentum space are given by:

$$\mathbf{K} = \left(\frac{2\pi}{3a}, \frac{2\pi}{3\sqrt{3}a}\right), \qquad \mathbf{K}' = \left(\frac{2\pi}{3a}, -\frac{2\pi}{3\sqrt{3}a}\right). \tag{1.3}$$

The three nearest neighbors vectors in real space are given by:

$$\delta_{\mathbf{1}} = \frac{a}{2}(1, \sqrt{3}) \qquad \delta_{\mathbf{2}} = \frac{a}{2}(1, -\sqrt{3}) \qquad \delta_{\mathbf{3}} = -a(1, 0) \tag{1.4}$$

while the six second-nearest neighbors are located at: $\delta'_{\mathbf{1}} = \pm\mathbf{a_1}, \delta'_{\mathbf{2}} = \pm\mathbf{a_2}, \delta'_{\mathbf{3}} = \pm(\mathbf{a_2} - \mathbf{a_1})$.

The tight-binding Hamiltonian for electrons in graphene considering that electrons can hop both to nearest and next nearest neighbor atoms has the form:

$$H = -t \sum_{\langle i,j\rangle,\sigma} \left(c^{\dagger}_{\sigma i} c_{\sigma j} + c_{\sigma j} c^{\dagger}_{\sigma i} + \text{h.c.}\right) \tag{1.5}$$

where $c_{i\sigma}$ ($c^{\dagger}_{i\sigma}$) annihilates (creates) an electron with spin σ ($\sigma = \uparrow, \downarrow$) on site $\mathbf{R}_i$ at sublattice A (an equivalent definition is used for sublattice B), and $t \approx 2.7$ eV is the nearest neighbor hopping energy.

The energy bands derived from this Hamiltonian have the form [38]:

$$\begin{aligned} E_{\pm}(\mathbf{k}) &= \pm t\sqrt{3 + f(\mathbf{k})}\,, \\ f(\mathbf{k}) &= 2\cos\left(\sqrt{3}k_y a\right) + 4\cos\left(\frac{\sqrt{3}}{2}k_y a\right)\cos\left(\frac{3}{2}k_x a\right), \end{aligned} \tag{1.6}$$

where the plus sign applies to the upper (π) and the minus sign the lower (π^*) band. Fig. 1.3. shows the full band structure of graphene. In the same figure we also show the band structure around the Fermi level and close to one of the Dirac points (at the $\mathbf{K}$ or $\mathbf{K}'$ point in the BZ). This dispersion can be obtained by expanding the full band structure, eq.(1.6), close to the $\mathbf{K}$ (or $\mathbf{K}'$) vector, eq.(1.3), as: $\mathbf{k} = \mathbf{K} + \mathbf{q}$, with $|\mathbf{q}| \ll |\mathbf{K}|$ [38]:

$$E_{\pm}(\mathbf{q}) \approx \pm v_F|\mathbf{q}| + \mathcal{O}((q/K)^2)\,, \tag{1.7}$$

where $\mathbf{q}$ is the momentum measured relatively to the Dirac points and v_F represents the Fermi velocity, given by $v_F = 3ta/2$, with a value $v_F \simeq 1 \times 10^6$ m/s. The energy dispersion (1.7) resembles the energy of ultra-relativistic particles; these particles are quantum mechanically described by the massless Dirac equation.

1.2 Nanographene

Nanographene have great potential for a variety of applications. Specially in optoelectronics and magnetic devices which differ from those of 3D and 1D counterparts [52]. Nanographene can be made by bottom-up and top-down approaches. In the bottom-up method, small molecular units are fused to form large aromatic hydrocarbons by a large variety of chemical reactions [53, 54] while in the top-down approach, nanographene are directly cut from a large piece of graphene sheet. Large graphene sheets are produced by a variety of methods, micromechanical exfoliation of a graphite single crystal [1], by chemical unzipping of carbon nanotubes (CNTs) [55], to mention a few.

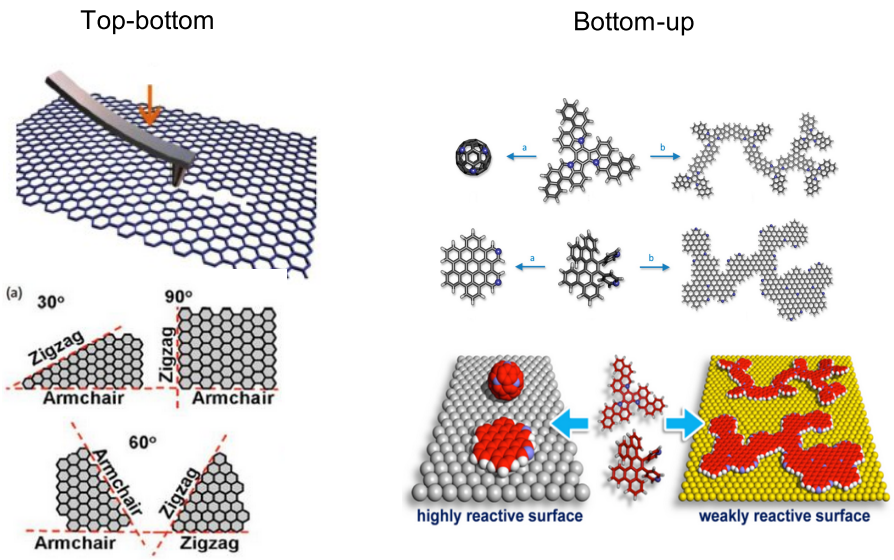

Figure 1.4: Ilustration of the both nanographene synthesis approches. Left: in the top-bottom approach nanographene is prepared from large graphene samples etching. Right: in the bottom-up approach nanographene is built from molecular precursors on different substrates.

Cutting graphene sheets into narrow strips yields graphene nanoribbons (GNRs). For many decades, GNRs have been of interest because of their theoretically predicted physical properties [56]. GNRs can be thought of as planar analogues of CNTs, with band gaps depending upon the ribbon width [56]. Thus, producing GNRs with defined widths and edge structures constitutes a great challenge that many chemists and materials scientists have sought to tackle. GNRs display a finite band gap when their width is less than 10 nm. In this context GNRs can be defined as a graphene strip with a width of less than 10 nm and with a large aspect ratio (generally, the length/width should be higher than 10); Nevertheless, there are a few papers reporting the fabrication of GNRs of widths of up to 50 nm while maintaining a large aspect ratio [58]. To avoid such confusion, those nanostructures are classified as quasi-GNRs. Also, it is very common using the term graphene nanoflake (GNF) as a large polyaromatic hydrocarbon (PAH) having sizes of 1-5 nm. Graphene fragments ranging from 10 to 100 nm are regarded as graphene quantum dots (GQDs). Once the size of the hexagonal sp^2 carbon network exceeds 100 nm, when can be properly regarded as graphene [54, 58].

The top-down methods for nanographene synthesis seem to suffer from drawbacks such as uncontrollable sizes and irregular edge structures. In contrast, the bottom-up organic synthesis is a usefull tool to create structurally well-defined graphenes. Nanographenes and GNRs of various sizes and shapes have been obtained in bulk scale, thus offering an opportunity for the additional solution/vacuum processing and device fabrication [53, 58].

The bottom-up synthesis of graphenes was initiated through the versatile organic chemistry of PAHs. According to the definition given in the introduction, graphene molecules with a size between 1 and 5 nm can be considered as the smallest nanographene. By far, the largest synthesized monodisperse nanographene molecule consists of 222 carbon atoms with a disk diameter of 3.2 nm, while one of the smallest and most frequently investigated graphene molecules, hexa-peri-hexabenzocoronene (HBC), has a size of approximately 1.4 nm [59]. More recently the synthesis of perfect hexagonal graphene

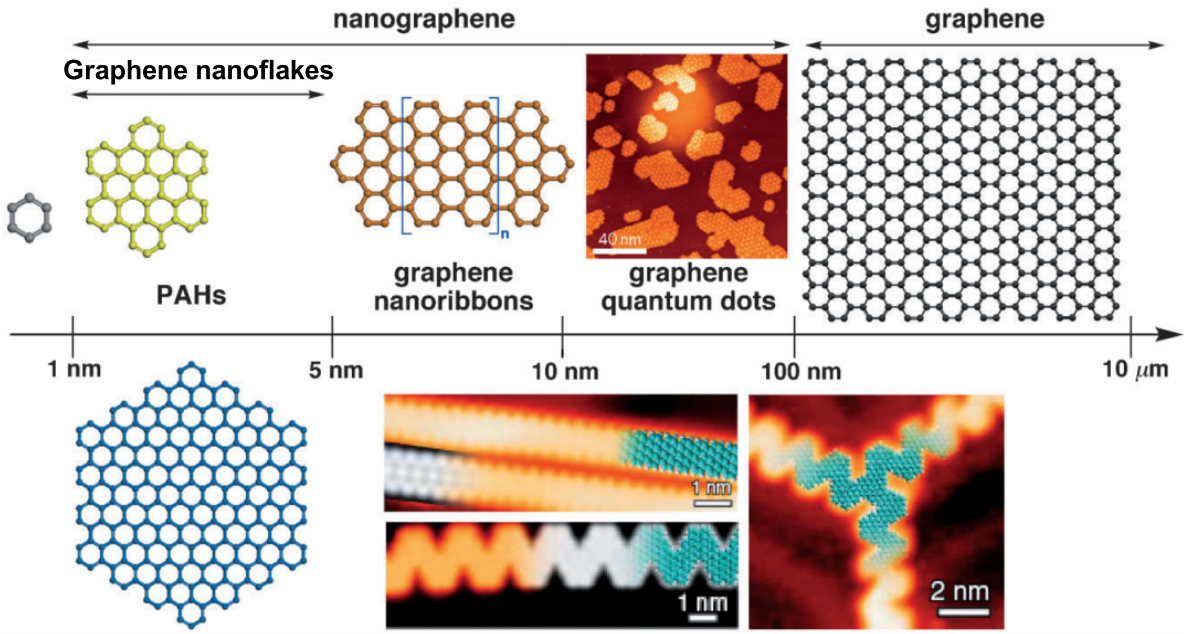

Figure 1.5: Schematic illustration of graphene terminology defined according to their size scale. Graphene molecules or nanoflakes are a subset of graphene with size between 1-5 nm; GNRs are defined as graphene strips with a width < 10 nm while maintaining a length/width ratio of > 10. GQDs are relatively regularly shaped graphene units with sizes ranging from 10 to 100 nm. Nanographene units are graphene fragments with diameters of < 100 nm, while graphene should exceed 100 nm in both directions. Adapted from reference [58].

nanoflake with well defined zigzag edges with 3.0 nm has been reported [60].

1.3 Edge states in graphene nanostructures

The surface structure of bulk crystalline semiconductors has profound consequences on the development and manufacturing of electronic devices. Bardeen explained that the presence of surface states results in binding of free carriers and induces the formation of Schottky barriers at semiconductor-metal interfaces [61]. A deeper understanding of surface states has enabled scientists and engineers to optimize the performance of integrated circuits for 50 years. Analogous to the surface states that exist in bulk crystals, the edge structure of nano-sized graphene can significantly influence their electronic structure.

Fig. 1.6(a) and 1.6(b) show respectively the STM and STS results for a uniform armchair edge. The STS spectrum indicates that the electronic structure in the vicinity of the Fermi level is the same as that of infinite graphene sheet with a feature of the massless Dirac fermion [10]. In contrast, zigzag edges have features that are different from armchair edges. Zigzag edges tend to be defective and short. They are observed frequently to be embedded between armchair edges, as shown in Fig 1.6(c). That behavior is a consequence of the energetically unstable structure of less-aromatic zigzag edges [10]. What is important in zigzag edges is the presence of edge states [10]. The STS spectrum (Fig. 1.6(d)) at the zigzag edge shows a sharp peak in the density of states at Fermi level, in addition to the linear π-bands, proving the presence of the edge state. The bright spots observed in the zigzag edge region (see Fig. 1.6(c)) are associated to the edge state.

The first reports of transport measurements [56, 62–64] and theoretical studies [7–9] for GNFs and GNRs elucidated their remarkable promise for future nanoelectronic applications. In spite of the first theoretical calculations that predicted a localized metallic state for the zigzag edge [65], all transport measurements of GNFs and GNRs revealated only semiconducting behaviour. Furthermore, the electronic properties of the graphene nanostructures were independent of crystallographic orientation [56] in contrast to theoretical predictions [56, 62–65]. Afterwards, theoretical studies show that transport effects such as Coulomb blockade [66] or a mobility gap induced by edge disorder [67, 68], may affect the accuracy of energy measured gaps under transport conditions and explain the independence of energy gap and crystallographic orientation.

Ritter and Lyding [69] determined by STS measurements the energy gap (E_g)-size (L) relation for GNFs with 2-20 nm lateral dimensions and correlate the E_g measurements with the GNFs edge structure. Predominantly zigzag-edge GNFs with 7-8 nm average dimensions are metallic and diverge from the E_g-L scaling law owing to the presence of metallic zigzag edge states, which spatially decay into the interior with a 1.0-1.2 nm decay length. For the GNFs exhibiting an energy gap, the experimental data were modelled with a power law, which resulted in E_g (eV) = 1.57/L for the least-squares fit. The experimental data are in close proximity to the predicted scaling trend E_g (eV) = 1.68/L [2, 47] resulting from a simple quantum confinement model and the linear dispersion of a graphene monolayer. In addition to GNFs, they studied the electronic structure of GNRs with 23 nm widths and 20-30 nm lengths. GNRs with a higher fraction of zigzag edges exhibited a smaller energy gap than a predominantly armchair-edge ribbon of similar width and the magnitudes of the measured GNR energy gaps agree with previous theoretical calculations [9].

More recently, Hämäläinen and co-workers studied by scanning tunneling microscopy (STM) and spectroscopy (STS) the quantum confined electronic states in atomically well-

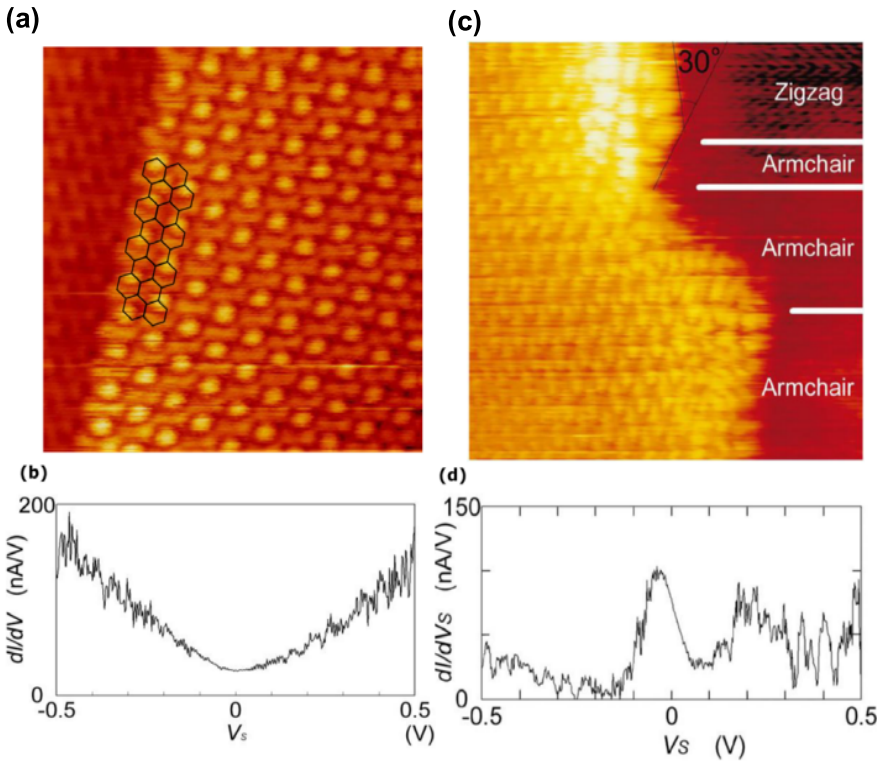

Figure 1.6: (a) Atomically resolved UHV-STM images (5.6×5.6 nm^2) of a homogeneous armchair edge in constant-height mode with bias voltage $V_s = 0.02$ V and current I = 0.7 nA. For clarity of edge structures, a model of the honeycomb lattice drawn on the image. (b) A dI/dVs curve from STS measurements taken at the edge in (a). (c) An atomically resolved UHV-STM image of zigzag and armchair edges (9×9 nm^2) observed in constant-height mode with bias voltage $V_s = 0.02$ V and current I = 0.7 nA. (d) The dI/dVs curve from STS data at a zigzag edge. Adapted from reference [10].

defined zigzag graphene nanostructures on the Ir(111) surface [60]. In such study the precise atomic structure and local density of states of individual GNFs as a function of their size is presented, however any evidence of the magnetic edge states and their influence on the energy gap is mentioned.

The strong influence of edge orientation on the electronic structure of graphene nanoribbons and nanoflakes was predicted long before graphene was isolated [65]. In absence of electron-electron interactions, these edge states localized near the Fermi level render GNRs metallic [9]. However, such one-dimensional metallic edge states with a high local density of states at the Fermi level become unstable upon electronelectron interactions. To lower the energy of the system, the flat band is splitted (open a gap) by ordering the spins along the two edges with antiferromagnetic coupling between opposite edges. Consequently, the emergence of magnetic order is closely linked to altering the electronic structure, through opening a energy gap. Recently, that gap opening has been observed in well-defined GNRs on Au [11]. Ribbons with the zigzag edge structure that are narrower than 7 nm exhibit an electronic energy gap of about 0.2-0.3 eV, which can be identified as a signature of interaction-induced spin ordering along their edges. Moreover, upon increasing the ribbon width, a semiconductor-to-metal transition is revealed, indicating the switching of the magnetic coupling between opposite ribbon edges from the antiferromagnetic to the ferromagnetic configuration. That study shows that the magnetic order on graphene edges of controlled zigzag orientation can be stable even at room temperature [11], raising hopes of graphene-based spintronic devices operating under ambient conditions.

The nature of long-range coupling between magnetic moments at the edges is dictated by whether the sites at the neighboring edges belong to the same or different sublattice of graphene. For example, atoms in a particular edge of regular hexagonal nanographene belong to the same sublattice, while atoms in the alternate edges belong to different sublattices. Thus, the intra-edge coupling is ferromagnetic, and inter-edge coupling is antiferromagnetic, which gives rise to a fully compensated ferrimagnetic solution with zero magnetic moment [72]. This behavior is in agreement with the Lieb's theorem [73–75]. Thus, it is worth exploring the possible ways to manipulate this intrinsic antiferromagnetic order toward an uncompensated magnetic order with net magnetic moment, which could be utilized in spintronics applications. Furthermore, some experimental studies shows that magnetism in zigzag nanographene is controversial with different reports of ferromagnetism [71], antiferromagnetism [11], and diamagnetism [10], and their coexistence. Therefore, the experimental situation concerning magnetism in graphene nanostructures remains debated, and is far from being fully understood.

The great progress in the synthesis of metallic and semiconductor GNFs with controlled size and shape briefly outlined above does not yet permit one to obtain isolated and clean samples, clearly limiting our capability to understand all the occurring critical phenomena, a necessary step towards engineering GNFs for a given application. Computational modelling based on density functional theory offers a useful and complementary approach to experiments. First-principles calculation on GNFs does not represent a problem, except for the computational resources, which become significant for quantum mechanical calculations concerning nanostructured in the 1-20 nm range, easily involving hundreds to thousands of atoms. In fact, the structural and electronic properties of small GNFs up to hundreds of atoms have been studied theoretically [5, 77] In particular the HOMO-LUMO energy gaps have been calculated [5]. However, for GNFs larger than 2 nm, theoretical studies are limited and most of these studies are based on tight-binding model [78]. This limitation is mainly due to the lack of computational tools that can be

used to perform large-scale first-principles calculations that involve thousand of atoms. Nevertheless, significant progress has been made in the field regarding the electronic and structural properties of GNFs. Recently, by means of density functional calculations, Hu and co-workers have studied electronic properties of armchair and zigzag GNFs with up to 2000 atoms [6], for armchair GNFs they report the well known 1/L scaling rule for energy gap. In contrast their calculations predicts that around 6-7 nm, zigzag GNFs exhibit metallic behavior, deviating from the 1/L scaling for the energy gap. However; in such study, the calculations were performed in absence of spin-polarization, and previously we have mentioned that the inclusion of spin polarization is necesary for a correct description of the magnetic order for the ground state of large zigzag GNFs.

1.4 Hydrogen storage in carbon-based materials

Design of hydrogen storage materials is one of the main challenges that must be addressed for a sustainable hydrogen-based economy [12, 13]. For that reason, the United States Department of Energy established three main targets for efficient hydrogen storage as (*i*) a gravimetric density of at least 7.5%, (*ii*) a minimum volumetric density of 0.07 kg H_2/L, and (*iii*) a reversible operation at ambient temperature and moderated pressures [79]. Presenting a light weight and a large surface area, carbon-based materials are considered good candidates to achieve a substantial hydrogen content. However, hydrogen storage in pure carbon materials is restricted by a very low adsorption energy of less than 0.1 eV per H_2, limiting the hydrogen content at operational temperatures [14,81,82]. Thermodynamic estimations indicate that the adsorption energies that would lead to an efficient cyclic adsorption/desorption process at room temperature and moderate pressures are in the range of 0.2-0.6 eV per hydrogen molecule [15, 16, 18, 83, 84], which is a narrow energy window that is intermediate between typical physisorption (less than 0.2 eV) and chemisorption (more than 0.6 eV). In contrast to carbon-based systems, materials like metal hydrides and polyaromatic hydrocarbons can store large amounts of hydrogen; however, the large hydrogen adsorption energies in these compounds avoid its reversible desorption [83].

In search of a solution to the hydrogen uptake problem, metal-decorated graphene species have been explored as possible candidates for hydrogen storage materials. Indeed, recent studies on metal-functionalized graphene show good performance for hydrogen storage by combining the low density of carbon materials with the catalytic properties of metal nanoparticles [15]. Previous experimental studies show that hydrogen storage on activated carbon and graphene samples can be dramatically enhanced by functionalization with palladium nanoparticles [15, 84]. Further, doping the porous graphitic materials with metallic atoms is viewed as a promising strategy to enhance hydrogen uptake [15, 85] because these metals have the effect of increasing the binding energies of molecular hydrogen to the pore walls. In addition, the adsorbed metallic atoms also can bind several hydrogen molecules [15], increasing the hydrogen capacity of the material. The binding of molecular hydrogen to transition metals has been explained using the Kubas model as a donation of electronic charge to the unfilled *d* orbital of noble metals such as Pd, followed by back-donation from the transition metal to the antibonding orbital of H_2 [86, 87].

However, there are some difficulties with the metal doping of graphitic materials. The first one is that aggregation of the adsorbed dopant atoms may occur, given that metal-metal bonding is usually stronger than the metal-carbon bonding [17,88]. Theoretical studies based on density functional theory reported that transition metal adatoms on

pristine graphene had binding energies from 0.2 to 1.5 eV [89], and their calculated migration barriers proved to be low, in the range of 0.2-0.8 eV, indicating that these adatoms should be mobile even at room temperature when deposited on pristine graphene [89]. That result explain the tendency of adsorbed transition metal atoms to form clusters on the graphene surface, leading to considerable reduction in its potential storage capacity. Note that the effect of the dopant metal in enhancing the amount of adsorbed hydrogen would be largest for maximum dispersion of the metal dopant, that is, when single metal atoms or very small clusters are present [17].

Contescu and co-workers [15] reported that only 18% of the adsorbed palladium on pristine graphene was in the form of single atoms forming Kubas complexes, $Pd(H_2)_n$, and 82% of total Pd forming $PdH_{0.67}$ species. The second problem in these systems is that desorption of metal-hydrogen complexes often also competes with the H_2 desorption. Both problems could however be reduced by increasing the binding energy of the metal atoms or small metal clusters to the supporting carbon substrate. This problem can be achieved by anchoring the metal atoms and small clusters to defects in the carbon networks of the graphitic pore walls [90]. First-principles calculations have found that defects in graphene (such as mono- and divacancies) increase the adsorption energy of metal atoms and small metal clusters significantly, to the point of exceeding the cohesive energy of the metal [91]. Krasheninnikov and co-workers reported that the typical binding energy values for transition metal atoms anchored to graphene monovacancies are around 7 eV [91]. This large binding energy value shows that transition metal atoms are strongly anchored to graphene defects, preventing their migration.

In recent theoretical works, Lopez and co-workers. [92, 93] reported that the binding energy of molecular hydrogen on a single Pd atom anchored on a graphene monovacancy was only 0.21 eV. This moderate hydrogen adsorption energy contrasts with the substantial adsorption energies of 0.96 eV/H_2 on Pd-doped pristine graphene and of 1.12 eV for the binding of H_2 on a free Pd atom. This result also shows the strong influence of the graphene defects on the H_2 adsorption. When the Pd atom employs a substantial part of its bonding capacity by interacting with the graphene monovacancy, as is the case of a Pd atom supported on the vacancy, the bonding with the H_2 molecule is weaker compared to Pd on pristine graphene [93]. However, it should be considered that in order to get a deeper understanding of the interaction between hydrogen and metal-decorated graphene it is necessary to include the effect of the cluster stability and its interaction with more than one hydrogen molecule.

Chapter 2

Computational Methods

First principles methods for electronic structure calculations are a powerful tool for the study of different properties of crystals, nanostructures, and molecular systems. The use of these approaches are widely extended between the scientific community, for that reason in this chapter we will give only a brief discussion about the fundamental concepts, physical approximations, numerical techniques and limitations. Which will be useful to understand the results of the following chapters.

2.1 The Born-Oppenheimer approximation

If we consider atomic nuclei and electrons like punctual masses and neglect relativistic effects, then the time-independent Hamiltonian for a molecular system is given by:

$$\hat{\mathcal{H}} = \frac{-\hbar^2}{2}\sum_{\alpha}\frac{1}{m_\alpha}\nabla_\alpha^2 \; - \frac{\hbar^2}{2m_e}\sum_i \nabla_i^2 + \sum_\alpha\sum_{\beta>\alpha}\frac{Z_\alpha Z_\beta e^2}{r_\alpha r_\beta} + \sum_\alpha\sum_i\frac{Z_\alpha e^2}{r_{i\alpha}} + \sum_i\sum_{i>j}\frac{e^2}{r_{ij}}, \quad (2.1)$$

where α and β are the atomic nuclei, i and j indicate electrons, m_e is the electron mass, e represents the electron charge, Z_α and Z_β the nuclear charge. The first and second terms in equation 2.1 denote the kinetic energies of atomic nuclei and electrons, respectively, meanwhile the last three terms represent the nuclei-nuclei, electron-nuclei, and electron-electron Coulomb interactions, respectively.

Even with the modern computational tools, the complete solution of the Schrödinger eq. (2.1) is a very hard task, for that reason with the aim to simplify the problem, often the Born-Oppenheimer approximation is used [100], which is based in the fact that the electrons move much faster than the nuclei, which it is estimated to be around of three orders of magnitud. In this way we can consider that the nuclei are nearly fixed with respect to electron motion. As a consequence, the hamiltonian (2.1) can be separated into a constant interaction and an electronic hamiltonian as is showed in eq. (2.2)

$$(\hat{\mathcal{H}}_{\text{elec}} - \hat{V}_{\text{NN}})\psi = E\psi \quad (2.2)$$

where

$$\hat{V}_{\text{NN}} = \sum_{\alpha} \sum_{\beta>\alpha} \frac{Z_\alpha Z_\beta e^2}{r_{\alpha\beta}}. \tag{2.3}$$

The variables in the eq. (2.2) are reduced only to electronic coordinates, because the internuclear distances $r_{\alpha\beta}$ are constant, in other words the wave functions depends parametrically on the the nuclear configuration:

$$\psi = \psi_{\text{ele}}(q_i, q_\alpha) = \psi_{\text{ele}}(q_i)\psi_{\text{nuc}}(q_\alpha) \tag{2.4}$$

where q_i and q_α are the electronic and nuclear coordinates, respectively.
Thus $\hat{V}_{\text{NN}}$ is constant for a given nuclear configuration, neglecting of this term in the hamiltonian does not affect the solution. Then, if we neglect $\hat{V}_{\text{NN}}$ in the eq. (2.4) we obtain:

$$\hat{\mathcal{H}}_{\text{elec}}\psi_{\text{ele}} = E\psi_{\text{ele}}. \tag{2.5}$$

Although the Born-Oppenheimer approximation is valid for a large number of systems in quantum chemistry and solid state physics. In the practice, we must employ additional approximations for electronic structure calculations.

2.2 Fundamentals on Density Functional Theory

In many-body quantum theory, the wavefunction is the fundamental variable that contains all information on the state of the system, and from which the expectation values of observables are calculated. For most interacting many-electron systems, the exact analytical solution for the wavefunction from the Schrödinger equation is not available and numerically exact solutions can be computed only for very small systems.

The main idea of density-functional theory (DFT) is that the ground-state wavefunction, which depends on the $3N$ spatial coordinates, can be replaced by a much simpler object: the N-electron density $n(r)$ that is a function of only three spatial coordinates. This mapping was proven in 1964 by Hohenberg and Kohn [101]. The first Hohenberg-Kohn theorem established that for electrons moving in an external potential, such as the potential caused by the nuclei, the ground-state density is uniquely determined. This is a one-to-one correspondence, meaning that conversely, the potential is uniquely determined by the density. The second theorem relates the ground-state density to the ground-state energy by stating that there is a universal energy functional $E[n]$. Minimizing $E[n]$ with respect to n gives the exact ground-state density. As the ground-state density is directly obtained from the ground-state wavefunction, the ground-state density can be used to describe the system instead of the wavefunction. The Hohenberg-Kohn theorems provide the theoretical justification for using the electron density instead of the wavefunction to describe the many-electron system. They do not, however, provide any concrete means to actually calculate this density. DFT became practical when Kohn and Sham [102]

formulated a mapping between the fully interacting many-body system and an effective one-body problem in a modified external potential. This Kohn-Sham potential $\upsilon_{\mathrm{KS}}(\vec{r})$, is obtained through the constrained minimization of the energy functional $E[n]$ with respect to a variation in the one-electron orbitals ψ_i. The potential can be divided into terms resulting from the original external potential $\upsilon_{\mathrm{ext}}(\vec{r})$, the Hartree potential $\upsilon_{\mathrm{H}}(\vec{r})$ describing the electrostatic interaction between electrons, and a third term, $\upsilon_{\mathrm{xc}}(\vec{r})$, containing all the electron-electron interaction terms not included in the Hartree potential such as electron correlations. All in all, this gives the form:

$$\upsilon_{\mathrm{KS}}(\vec{r}) = \upsilon_{\mathrm{ext}}(\vec{r}) + \upsilon_{\mathrm{H}}(\vec{r}) + \upsilon_{\mathrm{xc}}(\vec{r}), \tag{2.6}$$

for the Kohn-Sham potential. The ground-state density is then obtained by solving the one-electron Schrödinger equation

$$\begin{aligned} \hat{\mathcal{H}}_{\mathrm{KS}}\psi_i(\vec{r}) &= [-\frac{1}{2}\nabla^2 + \upsilon_{\mathrm{KS}}(\vec{r},\rho)]\psi_i(\vec{r}) \\ &= \epsilon_i\psi_i(\vec{r}) \end{aligned} \tag{2.7}$$

for the Kohn-Sham eigenstates and eigenenergies ψ_i and ϵ_i, respectively, and by constructing the ground-state density from the obtained orbitals,

$$n(\vec{r}) = \sum_{i=1}^{\mathrm{Occ}} |\psi_i(\vec{r})|^2. \tag{2.8}$$

Because $\upsilon_{\mathrm{KS}}(\vec{r})$ is a functional of $n(\vec{r})$, the problem has to be solved self-consistently. At first, an initial guess for the electron density is assumed, which is required for the calculation of $\upsilon_{\mathrm{KS}}(\vec{r})$, the diagonalization of the Kohn-Sham equations, and the subsequent evaluation of $n(\vec{r})$, along with E_{tot}. As long as the convergence criterion is not fulfilled, the numerical procedure is continued with the last $n(\vec{r})$ instead of the initial guess. When the criterion is satisfied, various output quantities like eigenvalues, occupancies, total energy and forces are computed, this prodedure is known as self-consistent field [102].

2.2.1 The exchange-correlation functional

Density functional theory would be exact if the exact form for the exchange-correlation potential $\upsilon_{\mathrm{xc}}(\vec{r})$ was known. Unfortunately, this is not the case and for all practical applications, this term has to be approximated. Frequently, the exchange-correlation term is composed into its exchange and correlation energy parts that are approximated separately, $E_{xc} = E_x + E_c$. The exchange-correlation potential is the functional derivative of E_{xc} with respect to the density n, given by $\delta E_{\mathrm{xc}}/\delta n = \upsilon_{\mathrm{xc}}$.

In the simplest approximation to E_{xc}, called the Local Density Approximation (LDA), E_{xc} is assumed to depend only locally on the electron density, and this dependence is assumed to be that of an homogeneous electron gas [48]. This approach can easily be

extended to treat the spin-dependent densities in magnetic systems. Allowing E_{xc} to depend also on the local gradients of the electron density leads to gradient-corrected functionals (GGA), such as PBE96 [110] widely used in this thesis. A number of improved functionals have been developed, for instance hybrid functionals mixing a portion of the exact Hartree-Fock exchange to a LDA- or GGA-type functional, and meta-GGA also depending on the kinetic energy density. An extensive review on the functionals that are available is not within the scope of this thesis, and the interested reader is referred to the literature, such as Ref. [103].

2.2.2 The band gap problem

DFT is a ground-state theory. Accordingly, the Hohenberg-Kohn theorems only state that the exact ground-state energy can be obtained by minimizing the energy functional. No physical meaning can be, however, given to the individual Kohn-Sham (KS) eigenvalues. The only exception is the energy of the highest occupied Kohn-Sham state, the energy of which is related to the first ionization potential of the system [103]. Even if the relative values of the occupied KS eigenvalues are in rather good agreement with the experiment for semiconductor and insulators, the band gaps are underestimated by about 50% up to 100% [103, 104]. The fundamental band gap for an N-electron system is defined by:

$$E_g = E^{(N+1)} + E^{(N-1)} - 2E^{(N)}, \tag{2.9}$$

i.e the difference between the electron affinity and the ionization potential. For the fictitious Kohn-Sham system we have:

$$E_g^{\mathrm{KS}} = \epsilon_{N+1}^{(N)} - \epsilon_N^{(N)}. \tag{2.10}$$

The difference between the fundamental and the Kohn-Sham gap is given by:

$$E_g - E_g^{\mathrm{KS}} = \Delta_{\mathrm{xc}} \tag{2.11}$$

We may see that the quantity Δ_{xc} is the difference between the energies of the $(N+1)$-th orbitals of the KS systems that correspond to the neutral and ionized electron system. The addition of an extra electron only induces an infinitesimal density change, so a discontinuity of order one have to be assigned to a discontinuity in the xc-potential, which is not necessarily analytic in N, in contrast to the Hartree potential:

$$\Delta_{\mathrm{xc}} = \upsilon_{\mathrm{xc}}^{(N+1)}(\vec{r}) - \upsilon_{\mathrm{xc}}^{(N)}(\vec{r}) \tag{2.12}$$

There is evidence [104] that the xc discontinuity Δ_{xc}, is the main cause of the large discrepancy between the experimental values and the one found in DFT for typical semiconductors and insulators. Thus, we can say that the band gap problem is not an intrinsic feature nor of the LDA or GGA functionals but of the Kohn-Sham scheme. In section (3.3)

we will see how energies of adding/removing electron to/from the system can be used to calculate the fundamental energy gap of GNFs within the quasiparticle formalism [118].

The energy difference between the highest occupied and lowest unoccupied Kohn-Sham state is commonly used to approximate the band gap, and it is widely known that this approach underestimates the actual gap due to the absence of the derivative discontinuity in the exchange-correlation potential. The Hartree-Fock approach, on the other hand, overestimates this discontinuity, and thus hybrid functionals that mix a portion of Hartree exchange yield larger band gaps than LDA or GGA, partly correcting the underestimation. On the other hand, the GW approximation [105], based on a perturbative expansion in the DFT-based Greens function G and a screened long-range Coulomb interaction (W), was developed to access the unoccupied side of the spectrum but it has been found to improve the predictions on the band gap magnitude. In order to access to excited-state properties such as optical spectra, also Time Dependent density Functional Theory (TDDFT) [106,107] and the solution to the Bethe-Salpeter equations [115], which includes excitonic contributions arising from the interaction between an excited electron and hole, are available.

2.3 Capabilities of the SIESTA

The SIESTA (Spanish Initiative for Electronic Simulations with Thousands of Atoms) code is a fully selfconsistent DFT method, based on a flexible linear combination of atomic orbitals (LCAO) basis set, with linear scaling [108]. It allows extremely fast simulations using minimal basis sets and very accurate calculations with complete multiple-zeta and polarized bases, depending on the required accuracy and available computational power. Apart from that of Born and Oppenheimer, the most basic approximations concerning the use of pseudopotentials, exchange and correlation are treated within Kohn-Sham DFT [102]. SIESTA code allow for both the local (spin) density approximation [109] (LDA/LSD) and the generalized gradient approximation (GGA) [110]. The code use standard norm-conserving pseudopotentials [109, 112] in their fully nonlocal form [112]. Also is posible to include scalar-relativistic effects and the nonlinear partial-core correction to treat exchange and correlation in the core region when is required [111].

2.3.1 Pseudopotentials

Although the use of pseudopotentials is not strictly necessary with atomic basis sets, it is very convenient to get rid of the core electrons and, more importantly, to allow for the expansion of a smooth (pseudo-) charge density on a uniform spatial grid. The theory and usage of first-principles norm-conserving pseudopotentials [112] is already well established. SIESTA reads them in semilocal form using the Troullier-Martins parametrization [112], transforming this semilocal form into the fully nonlocal form proposed by Kleinman and Bylander (KB) [19]. In some cases, particularly for alkaline metals, alkaline earths and some transition metals of the first few columns, we have sometimes found it necessary to include the semicore states together with the valence states [111]. In these cases, we also include two independent KB projectors, one for the semicore and one for the valence states. However, the pseudopotentials are still norm conserving rather than ultrasoft [113]. This is because, in the case of SIESTA, it is only the electron density that needs to be accurately represented in a real-space grid, rather than each wavefunction.

2.3.2 Basis set

Order-N methods rely heavily on the sparsity of the Hamiltonian and overlap matrices. This sparsity requires either the neglect of matrix elements that are small enough or the use of strictly confined basis orbitals, i.e. orbitals that are zero beyond a certain radius [114]. In SIESTA the latter approach is adopted because it keeps the energy strictly variational, which facilitate the test of the convergence with respect to the radius of confinement. Within this radius, our atomic basis orbitals are products of a numerical radial function and a spherical harmonic. For atom I , located at R_I , the basis orbitals are:

$$\phi_{Ilnm} = \phi_{Iln}(r_I)Y_{lm}(r_I), \tag{2.13}$$

where $r_I = r - R_I$. The angular momentum (labelled by l and m) may be arbitrarily large and, in general, there will be several orbitals (labelled by index n) with the same angular dependence, but different radial dependence, which is conventionally called a multiple-ζ basis [114]. The radial functions are defined by a cubic spline interpolation from the values given on a fine radial mesh. Each radial function may have a different cutoff radius and, up to that radius, its shape is completely free and can be introduced by the user in an input file. In practice, it is also convenient to have an automatic procedure to generate sufficiently good basis sets. SIESTA includes several such automatic procedures, and we shall describe one of them here for completeness, even though we stress that the generation of the basis set, like that of the pseudopotential, is to a large extent up to the user and independent of the SIESTA method itself [114].

In addition to the atomic valence orbitals, it is generally necessary to include polarization orbitals, to account for the deformation induced by bond formation, in this case polarization orbitals are frequently used. Considerer a valence pseudoatomic orbital $\phi_{lm} = \phi_l(r_I)Y_{lm}(r_I)$ such that there are no valence orbitals with angular momentum $l+1$. To polarize this, we apply a small electric field E in the z-direction. Using first-order perturbation theory we can show that the selection rules imply that the resulting perturbed orbital will only have components with $l = l \pm 1, m = m$ [114]. Thus after to integrate over the angular variables, we obtain the radial equation:

$$\left[-\frac{1}{2}r\frac{d^2}{dr^2} + \frac{(l+1)(l+1)}{2r^2} + V(r_i) - E_l\right]\varphi_{l+1}(r) = -r\phi_l(r), \tag{2.14}$$

The polarization orbitals are then added to the basis set: $\phi_{l+1,m} = N\varphi_{l+1}(r_I)Y_{l+1,m}(r_I)$ where N is a normalization constant [114].

We have found that the previously described procedures generate reasonable minimal SZ basis sets, appropriate for semiquantitative simulations, and double-ζ plus polarization (DZP) basis sets that yield high-quality results for most of the systems studied. We thus refer to DZP as the standard basis, because it usually represents a good balance between well converged results and a reasonable computational cost. In some cases (typically alkali and some transition metals), semicore states also need to be included for good-quality results [111].

2.3.3 Other features

Here we shall simply mention some of the possibilities and features of the SIESTA implementation of DFT [108].

(i) The systematic calculation of atomic forces and stress tensor allows the simultaneous relaxation of atomic coordinates and cell shape and size, using a conjugate gradients minimization or several other minimization/annealing algorithms.

(ii) It is possible to perform a variety of molecular dynamics simulations, at constant energy or temperature, and at constant volume or pressure, also including Parrinello-Rahman dynamics with variable cell shape. The geometry relaxation may be restricted, to impose certain positions or coordinates, or more complex constraints.

(iii) Mulliken charges and overlap populations for each spin channel, which is useful for magnetic systems.

(iv) The auxiliary program VIBRA processes systematically the atomic forces for sets of displaced atomic positions, and from them computes the Hessian matrix and the phonon spectrum. An interface to the PHONON program is also provided within SIESTA.

(v) A linear response program (LINRES) to calculate phonon frequencies has also been developed. The code reads the SCF solution obtained by SIESTA, and calculates the linear response to the atomic displacements, using first-order perturbation theory. It then calculates the dynamical matrix, from which the phonon frequencies are obtained.

(vi) A number of auxiliary programs allows various representations of the total density, the total and local density of states and the electrostatic or total potentials. The representations include both two-dimensional cuts and three-dimensional views, which may be coloured to simultaneously represent the density and potential.

(vii) Thanks to an interface with the TRANSIESTA program, it is posible to calculate transport properties across a nanocontact, finding selfconsistently the effective potential across a finite voltage drop, at a DFT level, using the Keldysh Green function formalism.

(viii) Optical response can be studied with SIESTA using different approaches. An approximate dielectric function can be calculated from the dipolar transition matrix elements between occupied and unoccupied single-electron eigenstates using First Order Time Dependent Pertubation Theory. For finite systems, these are easily calculated from the matrix elements of the position operator between the basis orbitals. For infinite periodic systems, we use the matrix elements of the momentum operator. It is important to notice, however, that the use of nonlocal pseudopotentials requires some correction terms.

In conclusion, the SIESTA method provides a very general and flexible scheme to perform a range of calculations from very fast to very accurate, depending on the needs and stage of the simulation, of all kinds of molecules, crystals and surfaces. It allows DFT simulations of more than a thousand atoms as in this work.

Chapter 3

Results: Electronic Structure and Quantum Confinement

Quantum confinement of massless Dirac fermions in graphene nanostructures has received special attention due to the importance of the gap opening in graphene for diverse applications [56]. In contrast to conventional semiconductors nanoestructures where the energy of electronic levels scales as $1/L^2$, the quantum confinement of massless Dirac fermions in graphene nanoestructures causes that the energy scales as $1/L$ [1, 2]. Ritter and Lyding [69] reported scanning tunneling spectroscopy (STS) of the (E_{g})-size (L) relation for GNFs. The measured values of energy gap lies in the range 0.8 up to 0.2 eV with a error associated with the energy gap determination of $\pm$ 0.1 eV. The measurements of E_{g} were modelled with a power law, which resulted in $E_{\mathrm{g}} \approx 1.57$ (eV/nm)$/L$. The experimental data are in close proximity to the predicted scaling trend E_{g} (eV) $= 1.68$(eV/nm)$/L$ [2,47] resulting from quantum confinement of noninteracting massless Dirac fermions [1–4]. The agreement between simple theory of confined Dirac fermions and experiment is surprising, which suggests that this simple model holds valid in a large range of sizes.

From the theoretical side, the energy gap size dependence of large GNFs with armchair and zigzag edges was studied first by Zhang [78] in the framework of Hückel model and more recently by Hu and co-workers using spin-restricted Kohn-Sham calculations, for armchair GNFs they reported the well known $1/L$ scaling rule for energy gap. On the other side their calculations predicts that around 6 nm, the systems begin to exhibit metallic behavior, deviating from the $1/L$ scaling, which seems in agreement with the experiment [69]. However, a very important issue that is worth mentioning, is the direct comparison between calculated and experimental energy gaps is very dificult by many reasons that which was not addresed in the theoretical studies mentioned above; namely, the energy gap opening due to edge magnetism in zigzag GNFs [11], the understimation of energy gap by DFT Kohn-Sham method [104, 118], the gap renormalization due to substrate polarization effects [122]. Furthermore, the samples reported in the work of Ritter and Lyding show irregular shapes with a mixture of zigzag and armchair edges even with the possible prescence of unpassivated edges. With these ideas in mind, it would be interesting to address questions about the origin of metallic behavior predicted by Hückel model and restricted Kohn-Sham calculations for hexagonal GNFs with zigzag edges larger than 6 nm [6, 78].

3.1 Computational details

We performed *ab initio* calculations based on the DFT [101], carried with and without spin polarization. For the exchange-correlation functional we used the Generalized Gradient Approximation (GGA) in the Perdew-Burke-Ernzerhof parametrization (PBE96) [110]. We also used norm conserving pseudopotentials as implemented in SIESTA code [112] and employed a double zeta basis function with polarized orbitals [108] and a mesh cutt-of energy of 300 Ry for the grid integration in real space. The convergence criterion for energy is chosen as 10^{-4} eV between two steps, and structural parameter were fully optimized within a force converence criterion of 0.01 eV/Å. The total energy was determinated optimizing the structural parameters by conjugated gradient. The vacuum separation between the structures in the adjacent unit cell is taken at least 15 Å in order to avoid the interactions between the structure with their images in the neighboring cells.

3.2 Size effects on HOMO-LUMO gap

Fig. 3.1 shows the evolution of single particle energy levels as function of GNF size. Small GNFs exhibit more discrete and spacing energy levels, showing the localized character of molecular system, we can see the band filling with the increasing size as well as the reduction of energy level spacing and the HOMO-LUMO gap narrowing. In Fig. 3.1 n is directly proportional to GNF size and represent the number of carbon atoms localized on each zigzag edge and ranges from 2 up to 16.

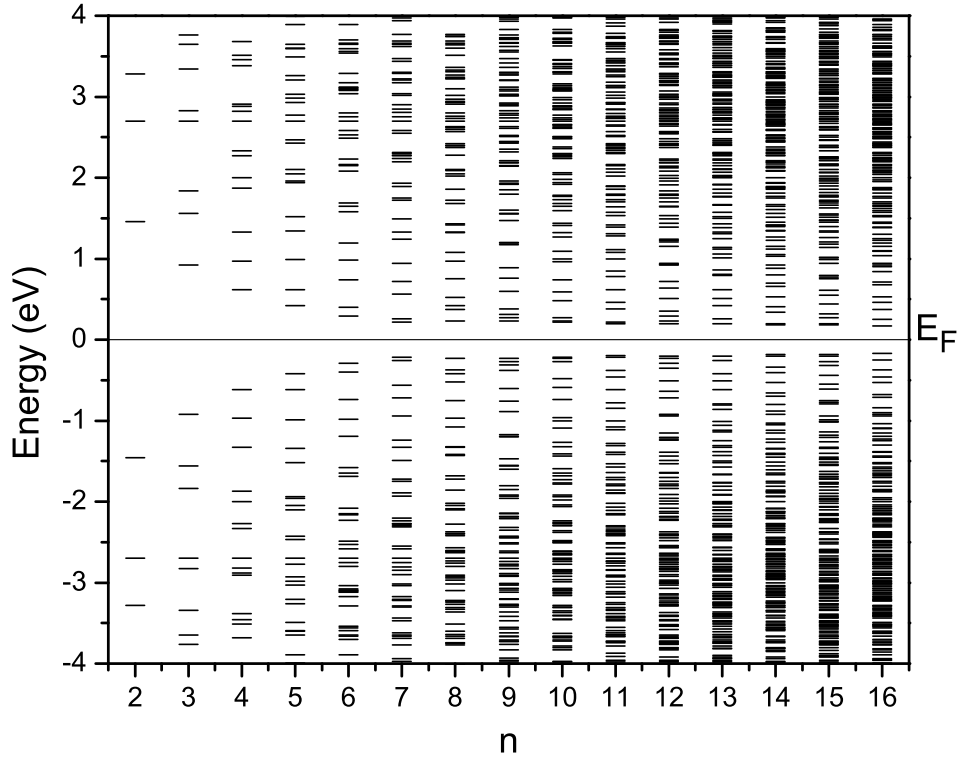

Figure 3.1: Evolution of Kohn-Sham energy levels with the increasing of GNF size ($C_{6nn}H_{6n}$, n = 2, ..., 16).

Other interesting aspects are the quantum confinement and localization of electronic states. Thus, with the aim of gaining physical insigth in this respect in Fig. 3.2(a) we show our calculations the occupied energy levels for hexagonal GNF n=7, and in Fig. 3.2(b) the projected density of states for different regions of GNF n=7. We can see that the carbon atoms localized on the edge (green region) are those that contribute mainly to degenerated HOMO and HOMO-1 states. while that HOMO-7 and HOMO-8 are localized mainly over the core region (blue region), the middle shell region (red region) exhibit a mixing of contribution from core and edge regions. In Fig 3.2(c) the experimental measurement of STM for perfect hexagonal GNFs n=7 is showed. Furthermore the Fig 3.2(d) shows the STS measurement for two points over core and middle regions. We can see the qualitative agreement between our calculated projected density of states and the experimental STS measurements with respect to the relative position of 1S and 1P peaks (red and blue lines in Fig 3.2(d)). Its is important to mention that the difference between the position of calculated peaks and the experiments is related with the fact that experimetal measurements were performed on Ir (111) surfaces meanwhile the in our calculation the system is isolated. This results clearly shows that the substrate effect is only the renormalization of energy levels to lower energies as result of the interaction.

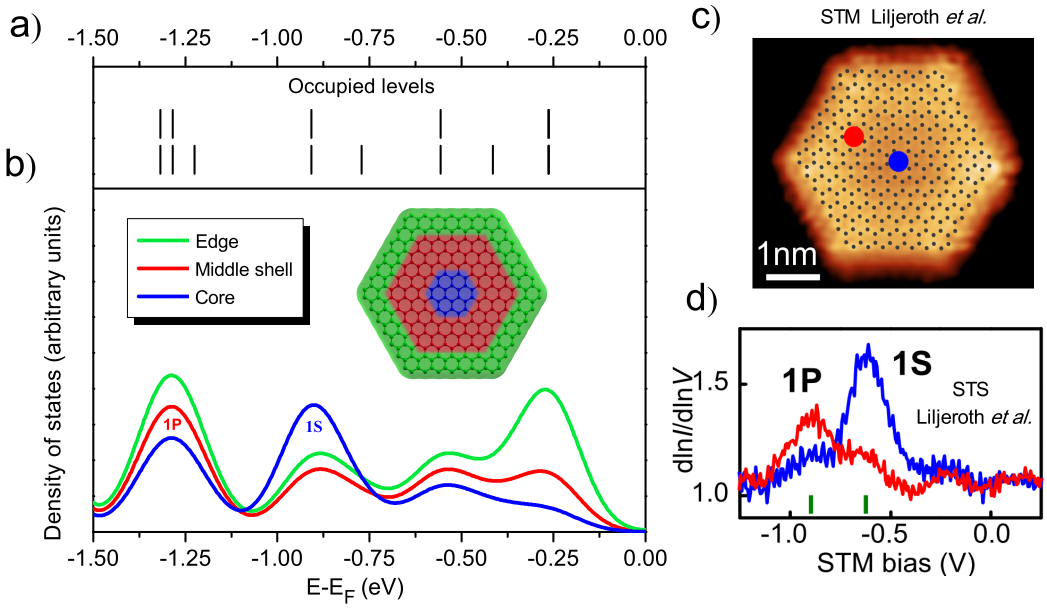

Figure 3.2: (a) Calculations for occupied levels for hexagonal GNF n=7 and (b) projected density of states for different regions of GNF n=7. (c) and (d) Experimental STM and STS measurements for hexagonal GNFs n=7 taken from ref. [60].

Now we address the size dependence of the HOMO-LUMO gap in hexagonal GNFs with zigzag edges. First, with the aim to understand the origin of metallic behavoir predicted in previous theoretical works. We have calculated the HOMO-LUMO energy difference in framework of spin-restricted Kohn-Sham method (without spin-polalization). Our calculations predicts a metallic behavoir for GNFs larger than 6 nm in the same way that previous calculations [6]. However when spin-polarization is included, we found a critical size (around 3.2 nm) where the metallic edge states become unstable upon electron-electron interactions and opens the energy gap by rearranging the spins along the

two edges with antiferromagnetic coupling between opposite edges, this semiconducting behavior remains even for GNFs larger than 6 nm, showing the importance of include spin-polarization for the correct description of the ground state of large GNFs with zigzag borders.

It is important to mention that similar results has been elucidated for n-acenes being considered as highly interesting building units for organic electronic materials, because of their diradical character that increases with the size [125]. The availability of longer acenes is, however, hampered by their increasing reactivity, with pentacene being the largest well-characterized acene [126]. In recent years substantial progress has resulted in the synthesis of n-acenes up to n=9 by matrix isolation techniques [126]. Nevertheless, these higher acenes are very reactive due to the prescence of unpaired spins. In order to overcome the kinetic stability problems, larger acenes were functionalized by adding protecting groups which inhibit the high reactivity of the acenes [127]. In this way, the calculations shows that larger hexagonal GNFs with zigzag edges exhibit radical character because the presence of unpaired electrons. However, due to the antoferromagnetic coupling between opposite edges the ground state of the system is a singlet.

For the moment we are only interested in studying the effect of magnetic edges states over the energetic of ground states and the size dependence of HOMO-LUMO gap. In the next chapter we give results about the spin distribution along the zigzag edges. The Fig. 3.3 shows clearly the effect of rising of antiferromagnetic ground states with the increasing of size. The emergence of that magnetic edge states can be attributed to a magnetic instability as a consecuence of the energy gap narrowing for the closed-shell state (NM). That is, as the energy gap approaches to the critical value, the near-degeneracy at the Fermi level coupled with electron-electron interaction makes the AFM state more stable. In other words, we can see the spin-polarization as one mechanism of the system for escaping of an instability associated with the presence of low energy electrons. Our calculations shows that this effect emerges for the system $C_{384}H_{48}$, ($n = 8$), which has a diameter of 3.2 nm.

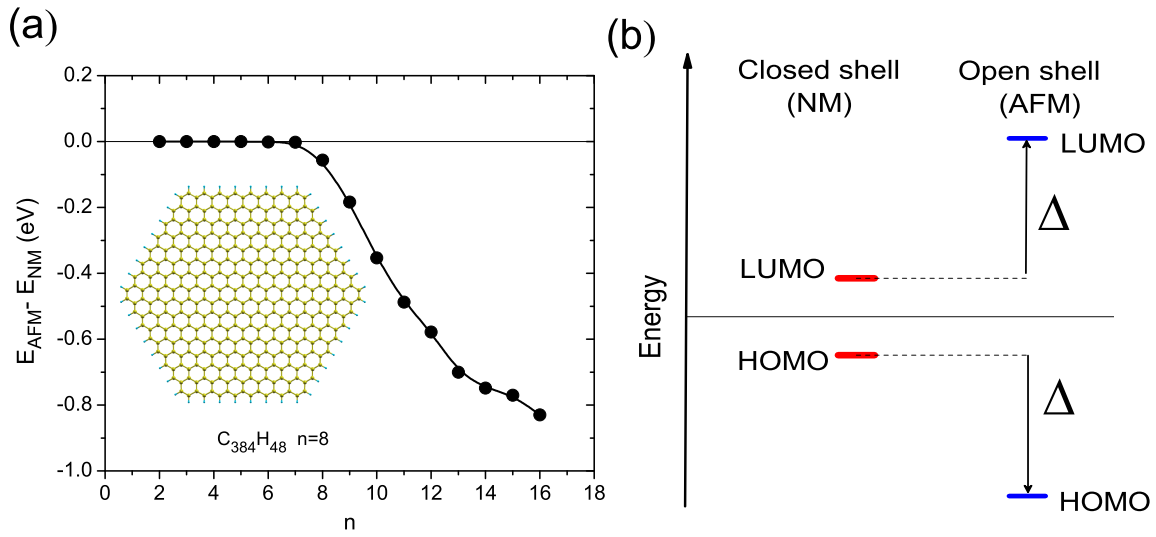

Figure 3.3: (a) Size dependence of the difference between total energy for AFM and NM states. For the smaller GNFs the ground state is non-magnetic closed shell ($n = 2 - 7$), however from n =8, the AFM ground state of zigzag GNFs becomes more stable. (b) Schematic picture about gap-opening due to magnetic instability.

As a starting point to modelling the size dependence of energy gap of the GNFs under study, we apply the confinement model of Dirac fermions. In this case, the GNFs are modelled as a circular GNFs with an effective diameter d (inset in Fig. 3.4), the boundaries impose a constraint on the motion in all directions so that the radial component of k vector is quantized: $k = m\pi/d$. Substituting this relation in the linear dispersion for a Dirac fermions we obtain the energy for the m-state, $\epsilon_m = \pi\hbar v_F m/d$. Hence the single particle gap between m and $m+1$ state is $\Delta E = \pi\hbar v_F/d$. for a value of the Fermi velocity of $v_F = 10^6$m/s, we have $\Delta E \approx 2.0(\text{eV.nm})/d$ this scaling rule is similar to one deduced by Berger [47]. In Fig. 3.4 we show the comparison between different approximations for the energy gap of GNFs under study, the single particle gap ΔE calculated with the effective model (solid black line) and the HOMO-LUMO gap calculated in the framework of spin-polarized Kohn-Sham method (red circles) and without spin-polarization (blue triangles). The Fig. 3.4 shows clearly the effect of rising of edge magnetism in the size dependence of energy gap (around 3.2 nm).

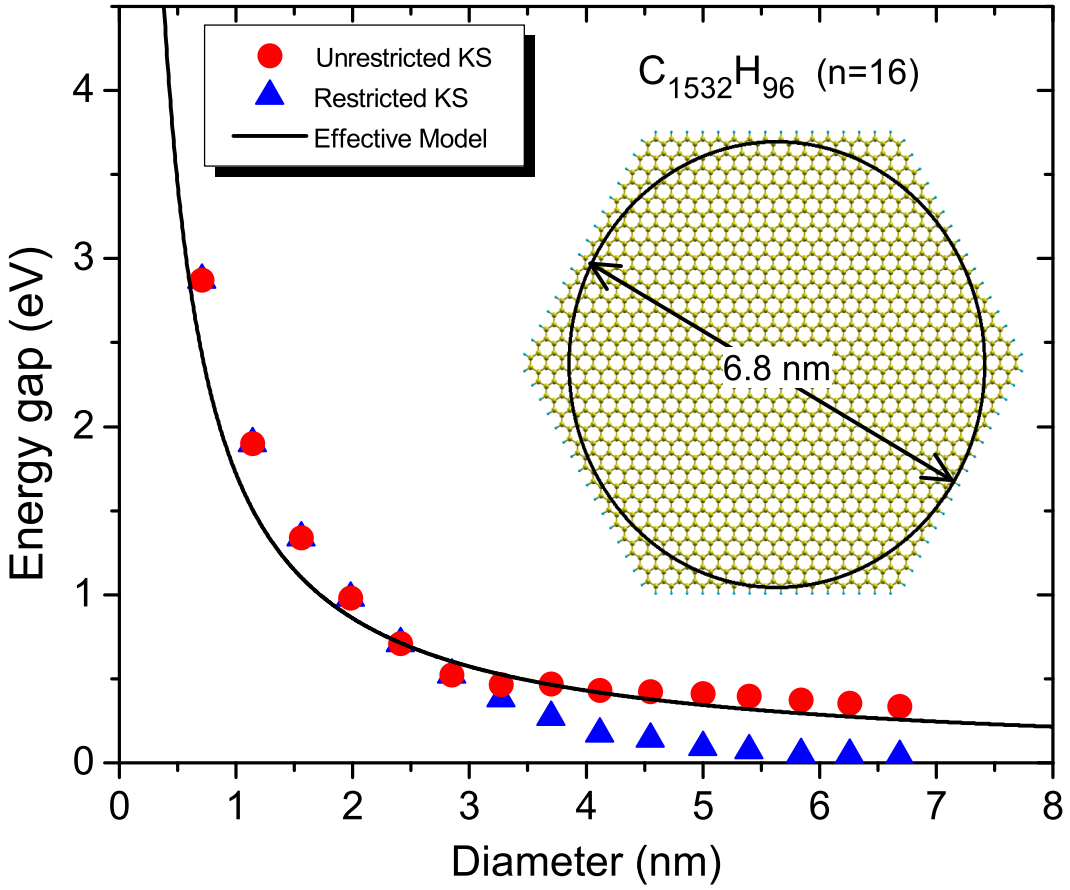

Figure 3.4: Comparison between different approximations for the calculated energy gap (HOMO-LUMO gap) of GNFs ($C_{6nn}H_{6n}$, n $= 2-16$). The effective model of confined Dirac fermions (solid black line), The Kohn-Sham gap within spin-polarized method (red circles), and the gap without spin-polarization (blue triangles).

While the calculations without spin-polarization predicts that the metallic behaviour for GNFs begin at 6 nm deviating from the trend predicted for the effective model, spin-polarized calculations predicts semiconducting behavior at 6 nm with a energy gap of

0.35 eV. This result shows clearly that the origin of metallic behavoir predicted at 6 nm in previous works is not related with the well known band gap problem of Kohn-Sham scheme, but instead with the absence of electron-electron interactions due to spin polarization.

It is worth to mention, that the effective model predicts values for single particle gap of larger GNFs that are in reasonable agreement with the calculated by most sophisticated spin-polarized Kohn-Sham method (red circles), which is wordering if we think that the effective model actually represents a electron confined inside of a circular region with infinite walls on extended graphene, the agreement can be explained if we consider that the energy difference between the highest occupied and lowest unoccupied Kohn-Sham state underestimates the actual energy gap due to the absence of the derivative discontinuity in the exchange-correlation potential [104]. For instance, for the GNFs under study, we can say that in the better of the cases effective model only predicts a reasonable estimation of the single particle Kohn-Sham gap. In the next section we will see how energies of adding/removing one electron to/from the system can be used to calculate the fundamental energy gap of GNFs within the quasiparticle formalism [118].

We note that the observation of the gap opening alone in zigzag graphene GNFs would not unambiguously indicate the prescence of edge magnetism, given that reconstructed zigzag edge configurations GNFs could contain significant fractions of armchair edges leading to semiconducting but non-magnetic GNFs. In recent work, there has been observed that GNRs of 7 nm ribbons with the zigzag-edge structure that are narrower than 7 nm exhibit an electronic bandgap of about 0.2-0.3 eV, which can be identified as a signature of interaction-induced spin ordering along their edges. Moreover, upon increasing the ribbon width, a semiconductor-to-metal transition is revealed, Theoretical models relating the origin of this semiconductor-to-metal the switching of the magnetic coupling between opposite ribbon edges from the antiferromagnetic to the ferromagnetic configuration. In other words, the signature of magnetic order in graphene nanostructures is related with the prescence of magnetic zigzag edges that can account for both gap opening and the observed semiconductor-to-metal transition. In Fig. 3.5, we present the calculated density of states for NM and AFM states of GNF $C_{1536}H_{96}$ which have a diameter of 6.8 nm.

3.3 Fundamental gap and self-energy corrections

System dimensions reduction causes the enhancement of other physical quantites that can contribute to the energy gap magnitud. Which are not taken into account in the confinement model of Dirac fermions or standard Kohn-Sham calculations. Most important, is the self-energy polarization [104, 118] which could deviate the electronic behavior of GNFs from the confinement model of Dirac fermions. From a physical point of view the energy gap can be expressed as $E_g = \epsilon_g^{ks} + \Sigma$, where ϵ_g^{ks} is the single particle Kohn-Sham gap. On the other side, Σ is the self-energy correction which could be calculated from the separate electron and hole quasiparticle energies via the GW method [105]. However, in the present study the size of the systems make the use of GW method unfeasible. Nonetheless, for finite size systems it is possible a simpler formulation of fundamental gap for the calculation of electron and hole quasiparticles [104, 123].

The fundamental gap E_g is calulated as:

$$E_g = E(m+1) + E(m-1) - 2E(m), \tag{3.1}$$

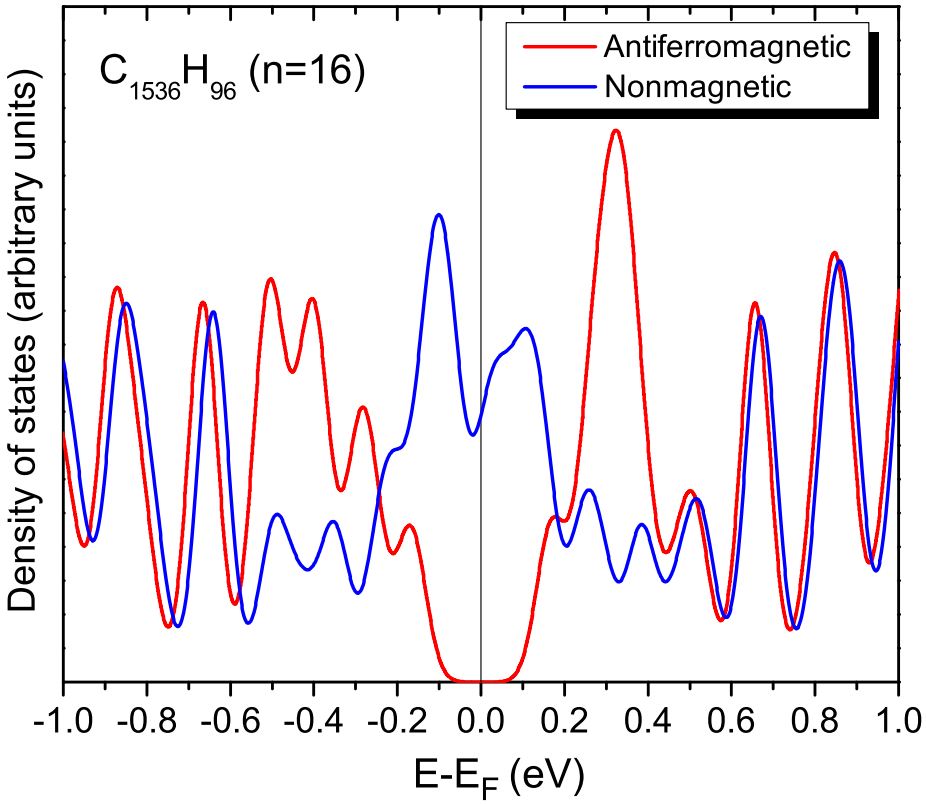

Figure 3.5: Total density of states for NM and AFM states of the largest GNFs under study (d=6.8 nm, n=16).

being $E(m)$ the total energy of the m-electron neutral system. In physical terms this aproximation for the fundamental gap (quasiparticle gap) includes the electrostatic effect of the charge density relaxation when an electron is added or substracted, and the corresponding relaxation in the exchange correlation potential, for instance it represents a systematic improvement with respect to Kohn-Sham method to approximate a energy gap of the system [104]. Thus, the fundamental gap calculation requires the self-consistent solutions of three different charge configurations for each quantum dot, $E(m)$, $E(m+1)$ and $E(m-1)$.

The calculated values for Kohn-Sham gap within spin-polarization and fundamental energy gaps as a function of the GNF size are shown in Fig. 3.6. The difference is the self-energy correction to energy gap. It is interesting to note the dramatic effect of the self-energy correction Σ in the magnitud of the fundamental gap which is finding strongly dependent of size. The main reason for the strong dependence of Σ on the GNF size is the significant enhancement of electron self-energy due to confinement effects even for the largest systems under study. The calculated values of self-energy lies in the range from 3.8 to 1.0 eV for GNFs with a effective radius from 1.0 up to 4.2 nm, respectively.

In order to characterize the size dependence of KS and fundamental gaps, we performed numerical fitting of the calculated data for $\epsilon_g^{ks}(d)$ and $\Sigma(d)$. We found that $\epsilon_g^{ks}(d) = 2.0/d^{1.1}$ in good agreement with confinement model. On the other hand $\Sigma(d) = 3.03/d^{0.98}$ which show the electrostatic nature of self-energy correction [123], E_g scaling rule can be written as:

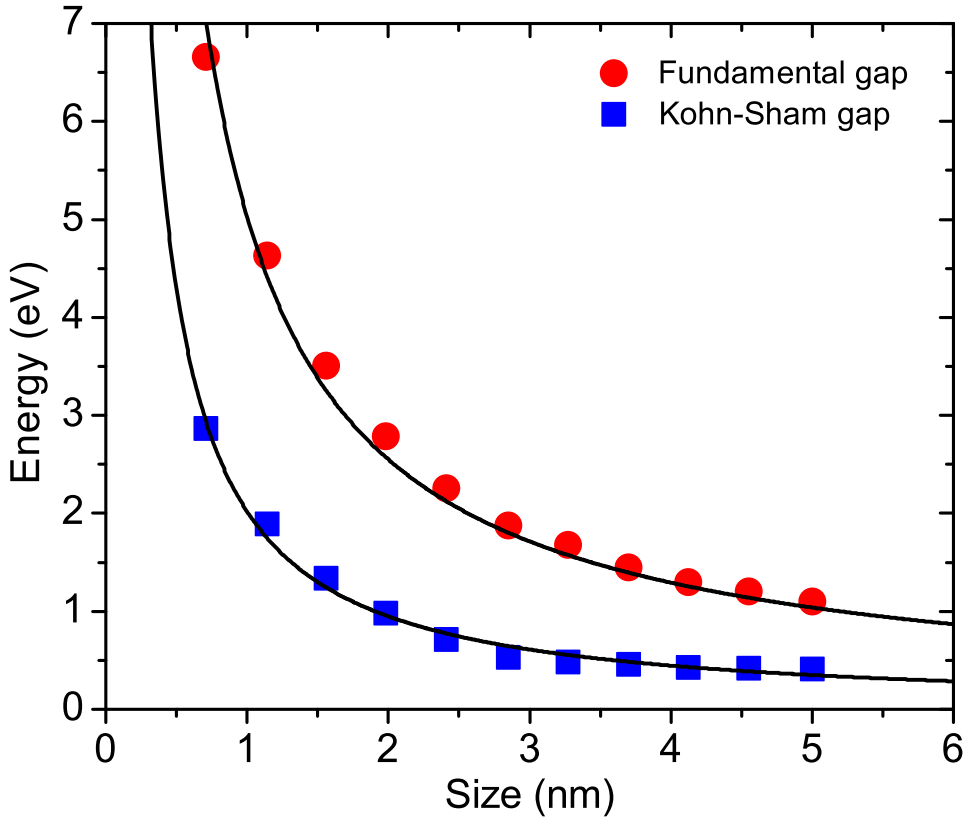

Figure 3.6: Calculated Kohn-Sham and fundamental energy gap as a function of effective radius for GNFs ($C_{6nn}H_{6n}$, n = 2 − 12) . The solid lines are power-law fitting whose parameters are mentioned in the text.

$$E_g = \frac{2.0}{d^{1.1}} + \frac{3.03}{d^{0.98}}. \tag{3.2}$$

Note that the scaling rule for both $\epsilon_g^{ks}(d)$ and $\Sigma(d)$ has the same asymptotic behavior, predicting that the energy gap vanishes when size goes to infinity as is expected for graphene. In contrast with previous calculations [6, 78], our scaling rule for fundamental gap predicts that even hexagonal GNFs with $d = 10$ nm are semiconducting with energy gaps around 0.5 eV. The scaling rule obtained in the present work for E_g, in principle can be useful to predict the fundamental gap for a hexagonal GNF of arbitrary size. Because experimental samples of GNFs usually have a combination of armchair and zigzag edges, we can expect slightly deviations from the values predicted by Eq. 2., but if the samples show some fraction of armchair edges, we can expect larger energy gaps than predicted [6, 78].

In summary the size dependence of energy gap in hexagonal GNFs with zigzag edges is was studied by density functional theory calculations. While the calculations without spin-polarization predicts that the metallic behaviour for GNFs begin at 6 nm deviating from the trend predicted for effective model, spin-polarized calculations predicts semiconducting behavior at 6 nm with an energy gap of 0.35 eV. That results show clearly that the origin of metallic behavior predicted at 6 nm in previous works is not related with the well known band gap problem of Kohn-Sham scheme, but instead with the absence of electron-electron interactions due to spin polarization. The agreement between the effective model of confined fermions and the spin-polarized calculations for HOMO-LUMO gap, can be explained if we consider that the energy difference between the highest occupied and lowest unoccupied Kohn-Sham states underestimates the actual energy gap due to the absence of the derivative discontinuity in the exchange-correlation potential. For instance the GNFs under study we can say that in the best case scenario the effective model only predicts a reasonable estimation of the single particle Kohn-Sham gap. Furthermore, to correct the band gap problem of Kohn-Sham Scheme, we have calculated the size dependence of fundamental energy gap adding/removing an electron to/from the system within the quasiparticle formalism. Thus, our calculations predicts that even hexagonal GNFs of 10 nm are semiconducting with energy gaps around 0.5 eV, in contrast with previous calculations neglecting the spin-polarization and which predict metallic behavior. We suggests that the metallic behavior observed in the experiment for GNFs larger than 6 nm can be attributed to substrate effects like gap renormalization, the shifting of Fermi level doping or chemical interaction between the top-most surface atoms and graphene carbon atoms. We expect that our results encourage future theoretical and experimental investigations with the aim of explaining the role of substrate effects on the modulation of electronic structure and magnetic edges states of GNFs or GNRs.

3.4 Optical properties

Optical properties description involves calculations of excited states. However, the most common approximations for density functional theory fail describing many-body effects like excitonic interaction, because its limited to ground state properties [101]. The solutions of Bethe-Salpeter equation [115] or multiple configuration of interactions methods [116] can take into account electronic correlations, necessary in the excited states

description, however their use in large systems is unfeasible. Time Dependent Density Functional Theory (TDDFT) [106], is an alternative to treat the problem of excited states in an approximated way, and that exhibit a good balance between accuracy and required computational resources, and which enables their application to systems with a few hundred atoms.

3.4.1 The single-particle, fundamental and excitonic gap

Before to discussing the main results about optical properties, it is convenient clarify some fundamental concepts related with the energy gap definition.

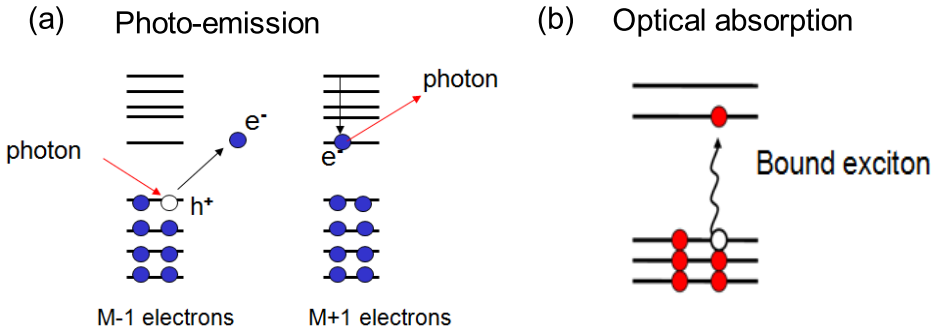

Figure 3.7: Schematic picture showing the different definitions for energy gap. (a) Shows the physical meaning of quasiparticle gap related with photoemission and inverse photoemission experiment. (b) Optical absorption is related with the formation of an interecting electron-hole pair.

In a previous section we have addresed the size dependence of HOMO-LUMO gap in the Kohn-Sham approximation (ϵ_g^{ks}) and the fundamental energy gap (E_g), and we have mentioned that the relation between these quantities is $E_g = \epsilon_g^{ks} + \Sigma$. Actually the Kohn-Sham gap refers to a HOMO-LUMO energy difference for an single-particle in a effective potential [118, 123], for hence some times is refered as a single-particle gap. The fundamental gap can be viewed as the energy difference of separate formation of hole or electron, which in principle, can be measured by photoemission and inverse photoemission experiments, On the other hand, the excitonic gap is related with the formation of an interacting electron-hole pair (exciton) which is a many-body effect totally absent in conventional DFT calculations. In fact, the relation between excitonic and fundamental energy gap is; $E_g^{exc} = E_g - E_b$, where E_b is the exciton binding energy, Typical inorganic semiconductors exhibit E_b values of some few meV (Wannier-like excitons),for hence the optical gap is practically the same than fundamental gap. In contrast, organic materials have larger E_b values of the order of 1 eV [22]. Particulary in the case of GNFs we expect large values of exciton binding energy, for example, experimental measurements for ionization potential and electron affinity of coronene ($C_{24}H_{12}$, n = 2), show that its fundamental gap is 6.87 eV, however optical determination shows a strong excitonic peak at 4.09 eV [124], showing a large excitonic binding energy of 2.78 eV.

In this thesis we have applied the TDDFT in the linear response approximation as is implemented in Quantum-Espresso code [113, 119, 120] to calculate the optical absorption spectrum of smaller GNFs ($n = 2-5$). In Fig. 3.8 we show the calculated values for Kohn-Sham, fundamental and excitonic gaps for benzene and some hexagonal GNFs ($n = 2-5$).

For all the systems under study, the excitonic gap values lie between the value for the fundamental and the Kohn-Sham gap. In other words, fundamental gap is the upper limit of excitonic gap in absence of electron-hole interaction, meanwhile Kohn-Shap gap is the lower limit neglecting self-energy polarization and electron-hole interaction. The effect of the exciton binding energy is the renormalization of fundamental energy gap. Also in Fig. 3.8, we can see that the difference between Kohn-Sham and excitonic gap decreases as the size increases. The origin of this behavior can be explain if we write the excitonic gap in terms of Kohn-Sham gap, self-enegy and exciton binding energy,

$$E_g^{exc} = E_g - E_b = \epsilon_g^{ks} + \Sigma - E_b, \tag{3.3}$$

we can see that Σ and E_b have opposite sign. Thus a large value in the exciton binding energy could cancel the contribution of Σ, making that $E_g^{exc} \approx \epsilon_g^{ks}$, it expected that this cancelation effect will be significant for larger systems as has been demostred previously in silicon quantum dots [118].

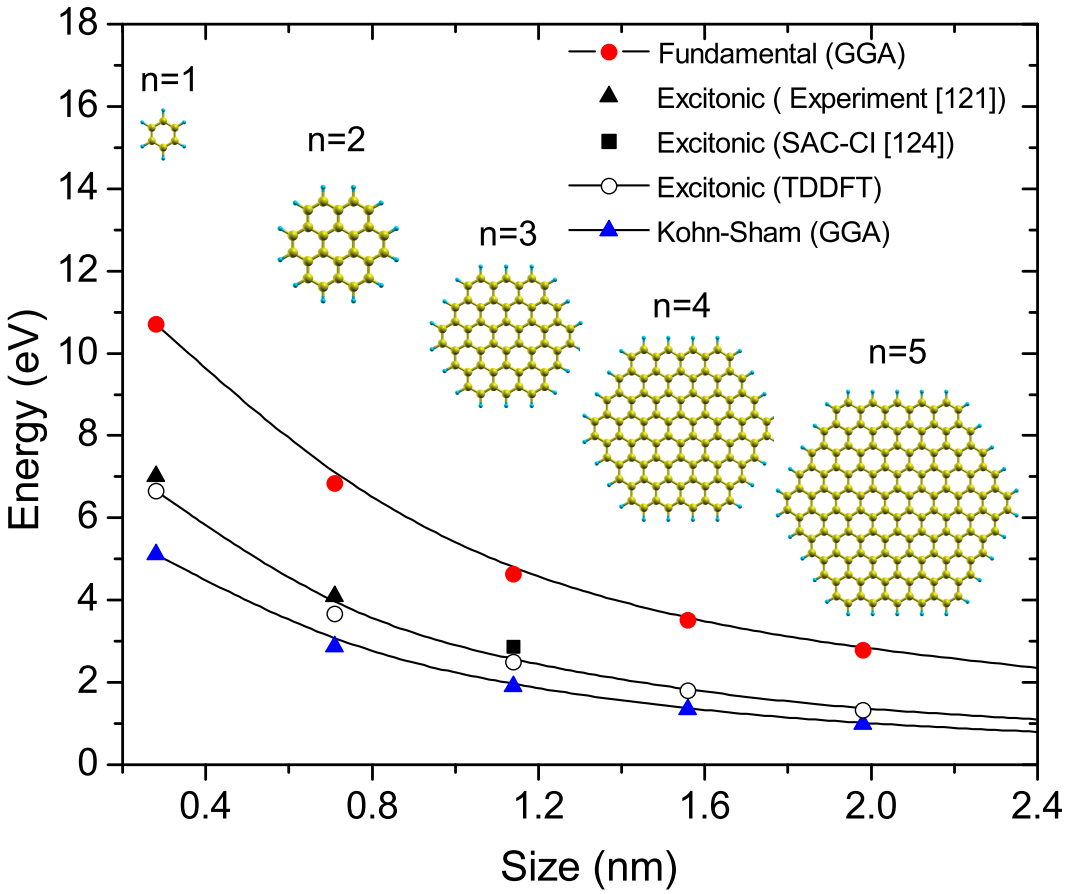

Figure 3.8: Calculated Kohn-Sham, fundamental and excitonic gaps a function of size for benzene and GNFs ($C_{6nn}H_{6n}$, $n = 2 - 5$). For benzene and coronene ($n = 2$) the experimental values for excitonic gap (black triangles) were taken from references [121] and [124], respectively. For $C_{54}H_{18}$ ($n = 3$) the excitonic gap was reported by Fukuda and co-workers in ref. [124], using Symmetry-Adapted Cluster-Configuration Interaction Method SAC-CI (black square).

Other interesting aspect presented in Fig. 3.8 is the comparison between experimen-

tal and calculated values for GNFs excitonic gap, with the aim to evaluate the reliablity of our TDDFT calculations we have incluided in the plot the experimental values for the excitonic gap of benzene and coronene (black triangles in Fig. 3.5) which are taken from references [121] and [124], respectively. Furthermore, we also included the calculated excitonic gap for $C_{54}H_{18}$ $n = 3$ (black square), which has been obtained by Fukuda and co-workers [124] using Symmetry-Adapted Cluster-Configuration Interaction Method SAC-CI. Our calculated values for excitonic gap by TDDFT method sistematically understimate the experimental values for benzene and coronene and by an amount of 0.3 eV. In the case of $C_{54}H_{18}$ ($n = 3$ *Cir*-coronene) the difference between TDDFT and SAC-CI method is around 0.4 eV. These differences are significant and can be corrected if we introducing long range separated corrections in the exchange-correlation kernel for TDDFT calculations [128], since that we have used GGA (PBE96) as starting point for the TDDFT calculations, that corrections are totally absent [107, 128]. However, despite of their limitations, we have showed that the present TDDFT calculations captures a good portion of the excitonic effects of GNFs.

3.4.2 Optical absorption

Optical absorption of GNFs is a very interesting issue to addres due to interesting features and potential application of GNFs in optoelectronics and plasmonics. However, as we have mentioned before, a rigorous study about optical properties involves the use of computational model that takes into account the electron-electron interaction for the description of excited states (TDDFT, CI, or BSE techniques), The large sizes of the systems under study in this work makes the application of such approaches unfeasible, for that reason we adopt a simplified strategy to give some physical insigths about the size effects on optical properties, for that end we have used random phase approximation (RPA). In Fig. 3.6(a) we showed the optical spectra for smaller hexagonal GNFs (n=2-5) obtained using the RPA, in Fig. 3.6(b) the TDDFT calculations are included for reference. For each system we have indicated the main absorption peaks with blue lines, we can see that the RPA spectra exhibit some slightly differences respect to calculated by TDDFT, however the relative positions of the peaks are very similar, in fact we noted that the effect including the electron-electron interactions (TDDFT) are not only a rigid shift of the spectra but that it has a significant effect on the renormalization of the excitation energies and the oscillator strengths. However, despite the differences between the two approximations, we can see that certain peaks occur in both approaches.

For example, the first excitation peak indicated in Fig. 3.9(a) corresponds to the lowest one-photon excitation between degenerated HOMO, HOMO-1 and LUMO, LUMO+1, meanwhile the second excitonic peak is the two-photon allowed excitations which involves electronic excitations between HOMO, HOMO-1 and LUMO+2 and LUMO+3 [78, 124]. On the other side, the more intense peak in TDDFT shows an energy reduction from 5.77 eV for coronene up to 4.73 eV in the case of n=5, while RPA results predicts a shift between 5.37 to 4.50 eV. Also in Fig 3.6(b) we can see that the TDDFT calculations predicts that the most intense peak exhibit a shoulder (blue arrows) that appears slightly blue-shifted by 0.4-0.5 eV, meanwhile that shoulders are totally absent in the RPA calculations, the origin of this behavior is explained by the electron-electron effects which are not included in RPA. Despite of the limitations of RPA, we conclude that RPA represent a reasonable approximation for study and give some physical insigths about the size effects on the optical properties of GNFs. For that reasons, larger hexagonal GNFs (n=6-10)

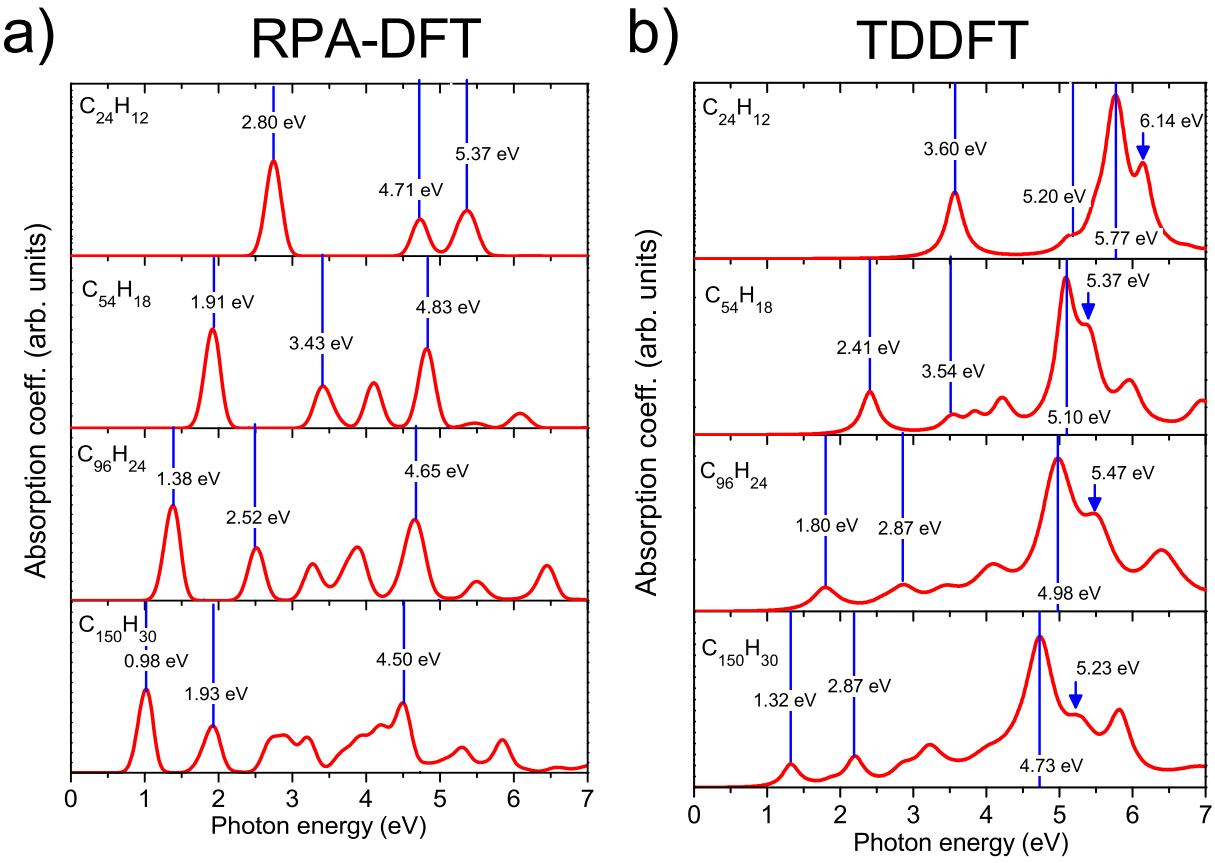

Figure 3.9: Absorption spectra of hexagonal GNFs (n=2-5). (a) Calculated using the random phase approximation (RPA) on single particle Kohn-Sham eigenvalues. (b) Calculated using the TDDFT approach. The main peaks are indicated in blue lines.

were calculated only at RPA level, the results for n=6 and n=7 are showed in the panels (a) and (b) of Fig 3.10, respectively. We can see that with the increasing the size a red shifting of the peaks occurs, however the most important features of the spectra remains preserved.

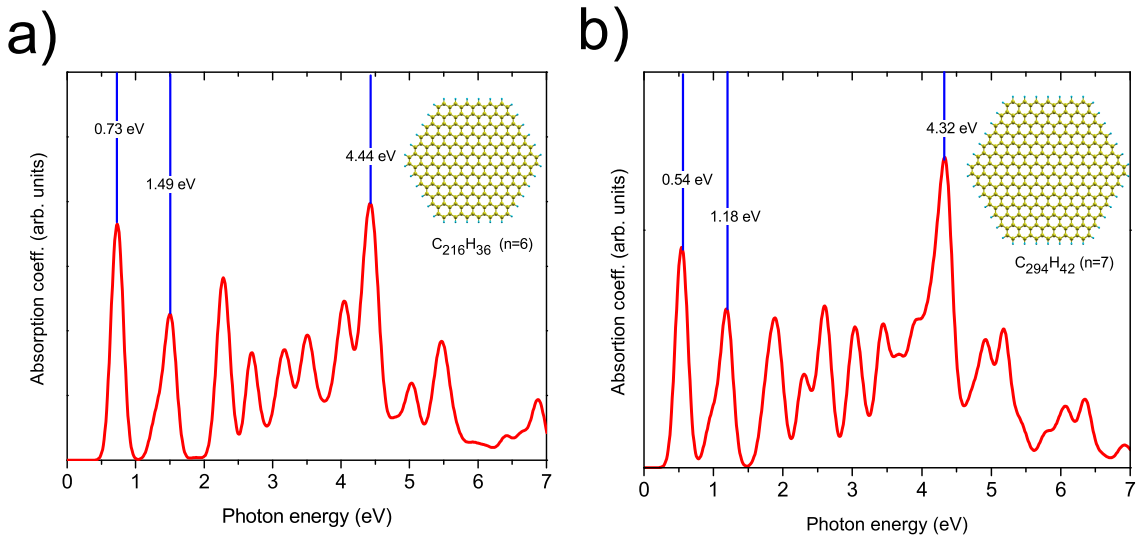

Figure 3.10: Absorption spectra calculated using the random phase approximation for (a) $C_{216}H_{36}$ ($n = 6$) and (b) $C_{294}H_{42}$ ($n = 7$).

Other very important issue is the effect of antiferromagnetic ordering on the optical properties of GNFs, previously we have showed that this effect occurs for $n \geq 8$. In Fig 3.11(a) we have plotted the optical absorption for medium size GNF n=10, the black line corresponds to the absorption coefficient calculated with out spin polarization (closed-shell system), while red line corresponds to the spin-polarized case (AFM system), we can see that the edge magnetism affects only the low-lying portion of optical espectra (near of absortion edge). In Fig. 3.11(b) we have plotted the ratio between the absorption coefficient for the AFM (A_{AFM}) case and the absorption coefficient for the NM case (A_{NM}), the effect of magnetic edge states is the renomarlization of absorption peaks as well as the changes in their intensities from the absorption edge up to around 3 eV, For energies larger than 3 eV. The A_{AFM}/A_{NM} ratio is equal to one indicating that the magnetic edges states do not have significant effects on more energetic excitations. These results shows the importance of including the spin effects in the calculations of the optical properties of graphene nanoestructures, which can be useful for future studies with more sophisticated methods for the correct treatment of excited states.

In Fig. 3.11(a) we can note that the positon of most intense peak at 4.23 eV is not affected by the rising of edge magnetism, this is indicative that edge states do not contribute to this excitation, we can question about the origin of this intense peak. In order to understand the origin of this excitation we must remember that experimetally this intense peak occurs at 4.5 eV for graphene monolayer [129] and many authors argued that this intense peak is related with the presence of collective excitations called π-π plasmons [129], Thus, we have calculated the optical espectrum for graphene monolayer and we have obtained a value of 4.1 eV for the most intense peak. In Fig. 3.12 we have plotted the difference between the energy of π-π plasmons in GNFs (E_{π}^{GNFs}) and our

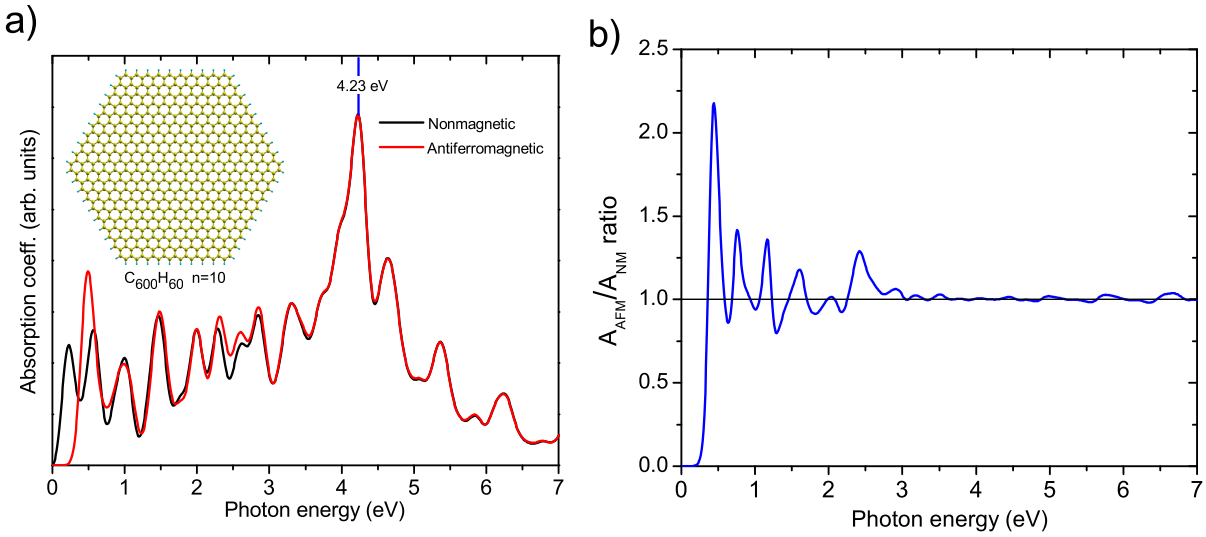

Figure 3.11: RPA absorption spectra for hexagonal GNFs $C_{600}H_{60}$ ($n = 10$). (a) Comparison between absorption spectra of the nonmagnetic closed-shell system (black line) and antiferromagnetic ground state (red line). (b) Ratio A_{AFM}/A_{NM} between the absorption coefficient for the AFM and NM states.

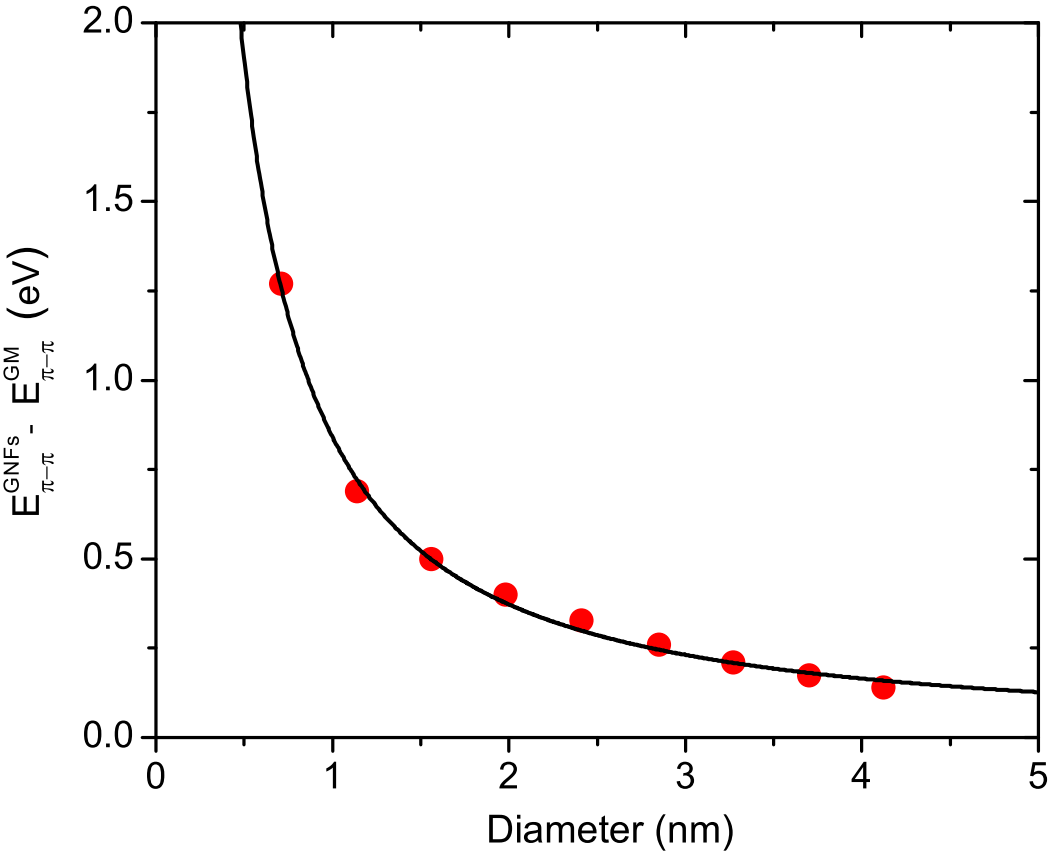

Figure 3.12: π-π plasmon energy difference as a function of effective radius for GNFs ($C_{6nn}H_{6n}$, n $= 2 - 10$) . The solid lines are power-law fitting whose parameters are mentioned in the text.

calculated value for π-π plasmon in graphene monolayer (E_{π}^{GM}=4.1 eV) as a function of size. Furthermore, we have fitted the calculated values to a power-law finding a scaling rule for the plasmon energy.

$$E_{\pi}^{\mathrm{GNFs}} - E_{\pi}^{\mathrm{GM}} = \frac{0.84}{d^{1.17}}. \tag{3.4}$$

The $1/d$ dependence that follows the plasmon energy, resembles the model of quantum confinement of Dirac fermions in graphene.

Chapter 4

Results: Edge Magnetism in GNFs

Graphene based magnetism recently attracts great interest due to the possibility of designing novel nanostructures with potential applications in spintronics. In this chapter a detailed study of the magnetic properties of the edge states in zigzag GNFs of different size and shape is presented. The theoretical studies addressing the issue of magnetism in carbon-based material have focused mainly on point deffects [70, 71], reduction of dimentionality [9, 72] or topological frustration in zigzag-edge GNFs [73, 74]. These works have shown that magnetism can arise in many ways, for example, the antiferromagnetic (AFM) order across the edges of zigzag GNRs [9], and the large net spin in zigzag-edge triangular GNFs [73, 74].

Compared to armchair-edge GNFs which usually exhibit considerable energy gap and nonmagnetic closed-shell ground state, the electronic structure and magnetic properties of zigzag-edge GNFs are found highly sensitive to their shapes. Triangular flakes present ferromagnetic order due the existence of degenerated edge states at Fermi level induced by the imbalance between the two sublattices as Lieb theorem predicts [76], while that the ground state of hexagonal and diamond-shaped GNFs have AFM ordering between opposite edges. That AFM coupling is induced by the spin polarization of the low-energy states that approaches the Fermi level as the system size increases. This kind of magnetism is characterized by a zero total spin moment and that antiferromagnetic order appears only if the on-site interaction energy is above of positive threshold.

It is well known the one-dimentional (1D) character of AFM order on the zigzag edge of GNRs [9, 72]. However, the eirlier studies of zigzag GNRS were based on periodic boundary conditions: namely, infinitely long ribbons were examined [9]. Unlike of GNRs, the zero-dimentionality of GNFs introduces the confinement along the finite edges and depending on the size and shape the magnetic properties can be tailored. As starting point and with the aim of gain physical insigth about the magnetism of edge states in GNFs we have selected the family of GNFs known as circumacenes and which structure is showed in Fig. 4.1(a),, which are a longitudinal extension of coronene molecule studied in previous chapters. Furthermore in order to evaluate the effect of GNF width, we select a second set of GNFs where we have numbered edges according to the number of carbon atoms at zigzag edges, such that a (n,m) GNF has n carbon atoms in its larger zigzag edge and m carbon atoms on its shorter zigzag edge as is shown in Fig. 4.1(b)

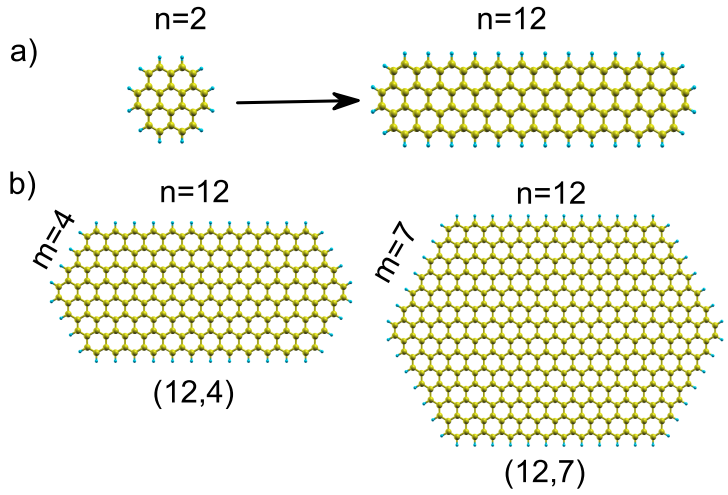

Figure 4.1: (a) Atomic structure of GNFs (circumacenes) with n=1-12 and (b) Atomic structure of GNFs (12,4) and (12,7).

4.1 Computational Details

We have performed *ab initio* calculations based on the DFT for GNFs (n,m) [101], which were carried out with and without spin polarization. For the exchange-correlation functional we have used the Generalized Gradient Approximation (GGA) in the Perdew-Burke-Ernzerhof parametrization (PBE96) [110]. We also used norm conserving pseudopotentials as implemented in SIESTA code [112] and employed a double zeta basis function with polarized orbitals [114] and a mesh cut-off energy of 300 Ry for the grid integration in real space. The convergence criterion for energy is chosen as 10^{-4} eV between two steps, and structural parameter were fully optimized within a force converence criterion of 0.01 eV/Å. The total energy was determinated optimizing the structural parameters by conjugated gradient. The vacuum separation between the structures in the adjacent unit cell was taken at least 15 Å, in order to avoid the interactions between the structure with their images in the neighboring cells.

4.2 Antiferromagnetic ground state

In Fig. 4.2 we show the total energy differences between AFM and NM states for circumacenes and we can see that, for n=2 up to 6 the energy difference is practically zero, which indicates a nonmagnetic closed-shell ground state. Also we can see that n=7 is the critical size where the AFM order emerges. For the studied systems, the AFM and NM states are very close in energy with a difference lower than 0.50 meV. Thus, for circumacenes with $n > 7$ the AFM becomes energetically more favorable than the nonmagnetic one.

The inset in Fig. 4.2 shows that the spin polarization for the circumacene with n=7 is spread mainly on the opposite zigzag edges and the maximum value of magnetization is localized in the middle of the largest edges. The Fig. 4.3 shows the values of the local magnetic moment m_i at the carbon atoms in zigzag edge. We found that the middle edge carbon atom has a maximum value of local magnetic moment of 0.28 μ_B.

It is particulary interesting to study the evolution of the AFM order along the edges as a function of GNF length. The Fig. 4.4 shows the local magnetization for circumacene

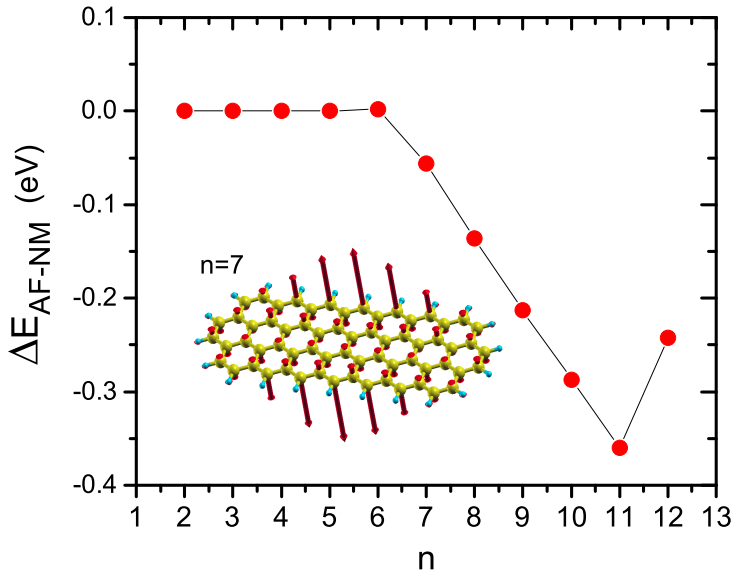

Figure 4.2: Total energy difference between the AFM and NM states for circumacenes. The AFM order emerges for circumacene with n=7. The inset shows that the spin polarization (red arrows) is spread mainly on the edges.

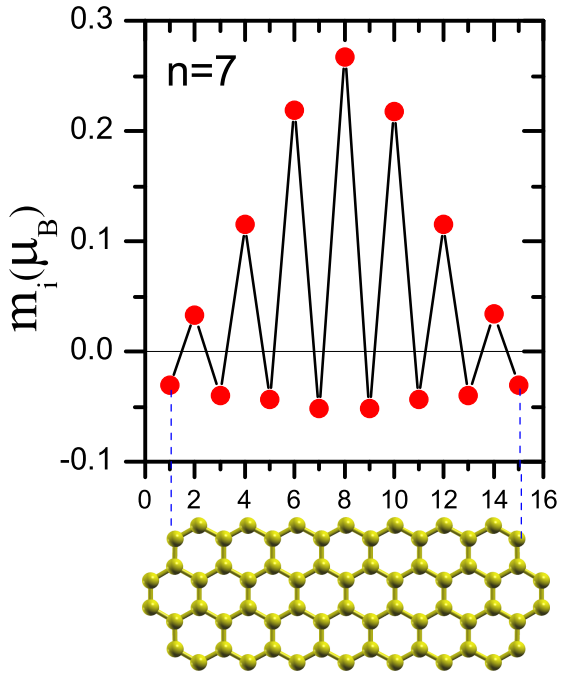

Figure 4.3: Local magnetic moment m_i at the zigzag edge in circumacene with n=7. The plotted magnetization correspond to one edge is plotted. Hydrogen atoms at the zigzag edges are omited for a better visualization.

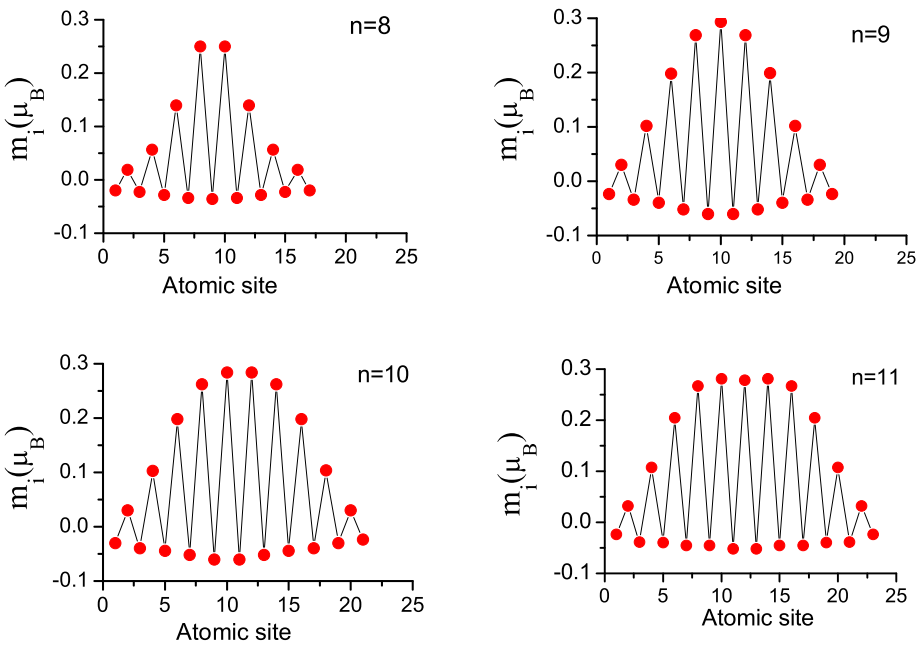

Figure 4.4: Evolution of local magnetization in circumacenes as a function of size (n=8-11).

with n=8 up to 11. The maximum value for m_i remains practically constant (around 0.28 μ_B) for all the studied circumacene. As the length of zigzag edges increases the magnetization at the carbon atoms in the central part of the edge becomes nearly uniform. This resembles the spin distribution of infinitely long GNRs [9], where the ground state is characterized by ferromagnetic arrangement of spins along the edges with antiferromagnetic coupling of the spins at the opposite edges.

4.3 Collinear domain wall formation

A very interesting result is the formation of a spin-collinear domain wall (SCDW) for the circumacene with n=12, Fig. 4.5 illustrates the distribution of the spin density at the carbon atoms of the circumacene with n=12, we can see the domain wall located in the center of the edge fragment. The spin populations of the outermost edge atoms is showed in Fig. 4.6 where the domain-wall is characterized by a spin wave excitation with a node localized in the middle of the nanostructure and a maximum value for m_i of 0.30 μ_B.

In Fig. 4.7 we show a quantitative analysis of the polyradical character of GNFs under study by means of the magnetization on each sublatticce, since the sublattice magnetization is proportional to the number of unpaired electrons in the system. We found that the sublattice magnetization exhibits a nearly linear behavior with the length from n=7 to 11 however for n=12 a discontinuity occurs, which is clearly associated with the formation of the collinear domain wall.

The origin of the AFM state was discussed in a previous chapter for the case of hexagonal GNFs. We have mentioned that the onset of magnetism is associated with an electronic instability due to the presence of low-energy states, for that reason the system opens an energy gap with the aim of avoiding the instablity. This mechanism is ilustrated in Fig. 4.8(a) where the single particle spectrum for NM and AFM state is schematized.

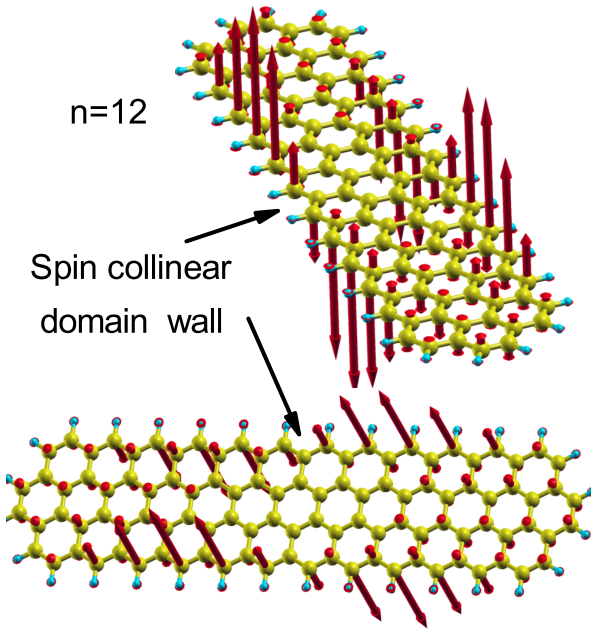

Figure 4.5: Spin collinear domain wall formation at the circumacene with n=12. The magnetic moments of the atoms are showed by red arrows and the magnitude is proportional to the arrow length

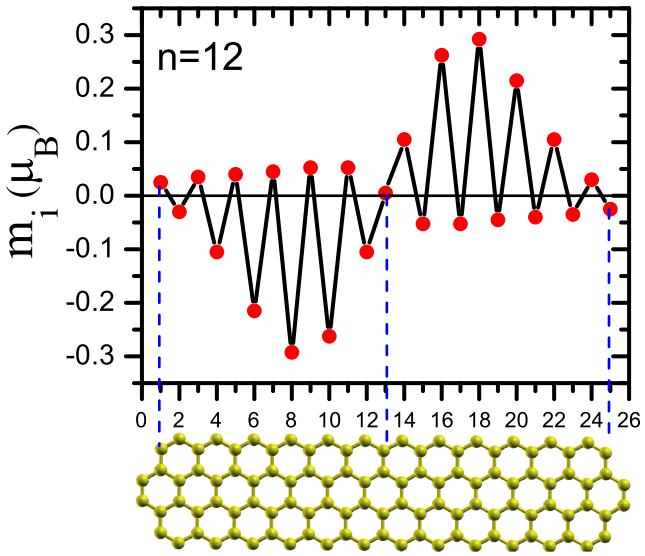

Figure 4.6: One-dimentional representation of the local magnetic moment for the circumacene with n=12.

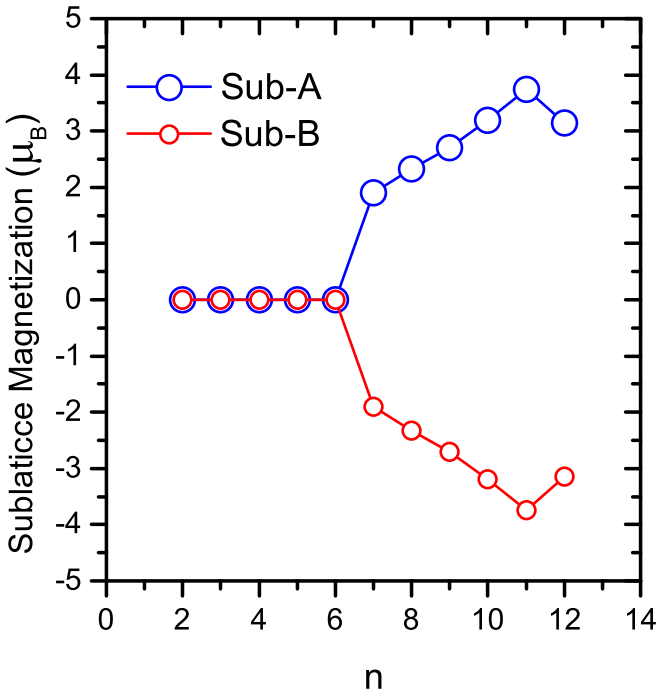

Figure 4.7: Sublattice magnetic moment as a function of n for circumacenes with n=2-12.

The magnitud of energy gap opening (2Δ) is showed in Fig. 4.8(b), where we can see that this quantity is depending of size and shows a similar behavior to the sublatticce magnetization (see in Fig. 4.7).

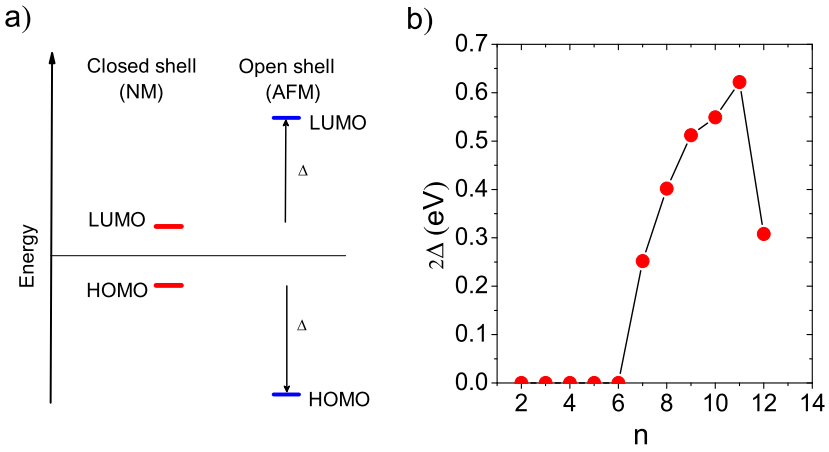

Figure 4.8: (a) Schematic energy shift 2Δ of HOMO and LUMO levels for circumacenes and (b) Energy level Shift 2Δ as a function of n.

Having explored the effect of the length on the energetics and magnetism of circumacenes, we now turn to discuss how the AFM state depends on the width. For this purpose we focus on a second set of GNFs, which are presented in Fig. 4.1(b). These GNFs has been denoted according to the number of carbon atoms at the zigzag edges, such that a (n, m) GNFs has n carbon atoms on its larger zigzag edge and m atoms on its shorter zigzag edge. This kind of GNFs have a similar topology of the circumacenes studied

above. In fact circumacenes are a special case of the (n, m) structures with m=2. For this part of the study we take n = 12 and m=4,7. In Fig. 4.9(a) we showed the SCDW for (12,4) GNF, which is practically the same for the (12,2) structure, however for the (12,7) system the situation changes dramatically with the disappearance of the SCDW as can be observed in Fig. 4.9(b). In Figs 4.9(c) and (d), we present the comparison of the local spin magnetic moment at the perimeter for (12,4) and (12,7) structures. In the case of the (12,7) system the spin moment shows two maximum values close to 0.30 μ_B spread along the largest edge, and four magnetic moments with values of 0.1 μ_B spreading on the shorter edges. Thus the spin polarization of (12,7) GNF resembles the result reported previosuly for hexagonal GNFs, where the antiferromagnetic arregement of spins at the hexagon segments are separated by the 120°-turn of the zigzag borders.

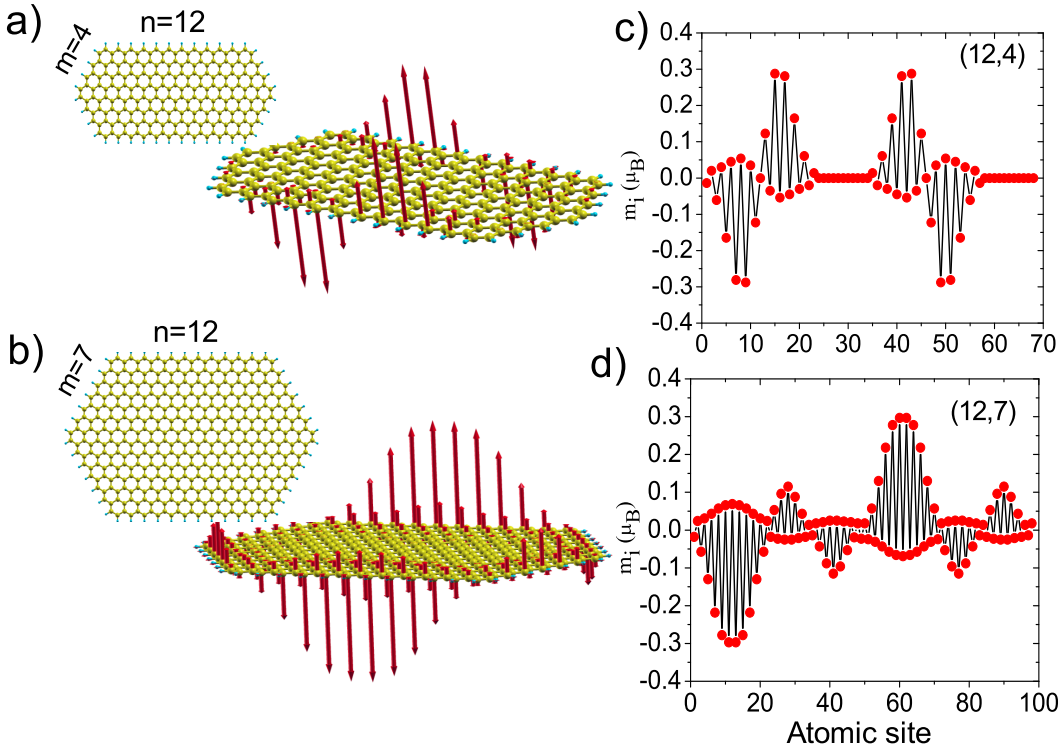

Figure 4.9: Atomic structures and spin magnetization for the GNFs (a) (12,4) and (b) (12,7). One dimentional representation of spin magnetic moment along the perimeter for the GNFs. (c) (12,4) and (d) (12,7).

In Fig. 4.10 we present the atomic structure and magnetic moment along the perimeter of the hexagonal graphene nanoflake with zigzag edge $C_{864}H_{72}$. This GNF can be viewed as a limit case of (n, m) GNFs with n=m=12. In this case we can see that the magnetic spin moments are equally distribuited at the six facets of the structure exhibiting antiferromagnetic coupling. Based on all these results we can conclude that the formation of collinear domain wall in GNFs with zigzag edges is strongly dependent on the separation distance between opposite edges in the structure. Thus the formation of collinear domain walls is favoured in GNFs with small aspect ratio (width/length), in contrast most symmetrical and high aspect ratio structures prefers the antiferromagnetic couplig between opposite edges as is the case of hexagonal GNFs.

In brief, we have found that the antiferromagnetic state is energetically more favor-

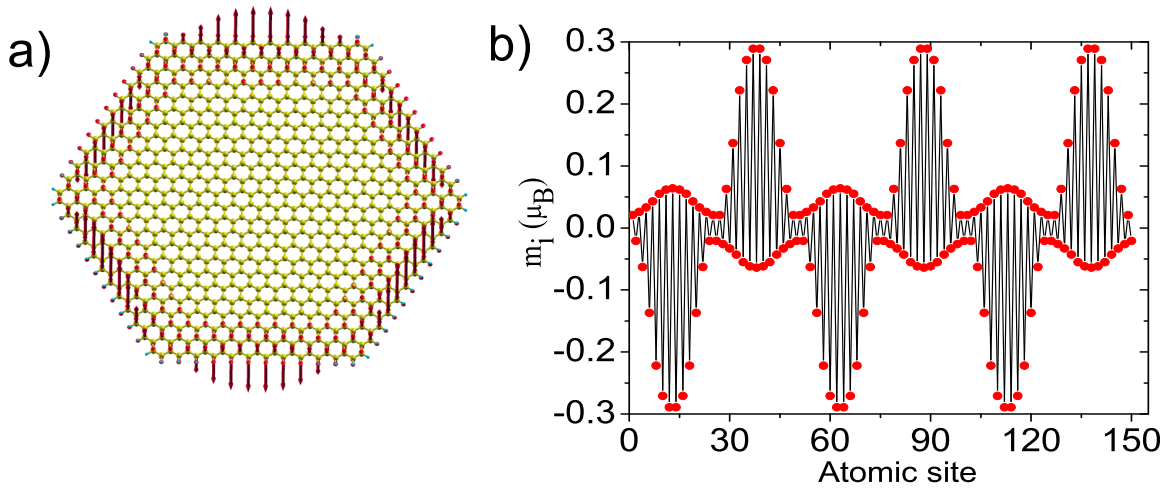

Figure 4.10: (a) Atomic structures and spin magnetization for hexagonal GNF $C_{864}H_{72}$ (n=12) and (b) One dimentional plot of edge magnetization for GNF (n=12).

able than the nonmagnetic one for larger GNFs with small energy gap, and also that total magnetic moment is M=0, as is predicted by Lieb theorem [73, 74, 76]. However is interesting the question about the posibility of a ferromagnetic state and the relative stability respect to the antiferromagnetic and nonmagnetic solutions. With the aim to answer this question Fig. 4.11(a) shows the energetic differences between AFM and NM state (red circles) and the difference between FM and NM state (blue triangles) for circumacenes (n,2) with n=7-13. We can see that for n=7-11 the antiferromagnetic states is more favorable, however from n=12 we founded that the ferromagnetic states becomes the ground state. The Fig. 4.11(b) shows the calculated magnetic spin distribution for (12,2) GNF, maximum magnetic moment is 0.28 μ_B and the total magnetic moment M=4 μ_B, which indicates a polyradical system with four unpaired electrons. This result is very surprising, considering that until now ferromagnetic ground states with M$\neq$0 has been predicted only for graphene nanoflakes with topological frustration, where the total magnetic moment is given for the nullity of the graph associated to the molecular structure [73, 74]. However the structures studied in this thesis are symmetrical and their nullity is zero, so there not topological frustration involved in the ferromagnetic ground state, the only explanation for the results discussed above is the magnetic correlations resulting from of the electron-electron interactions. A detailed analysis of energetic and spin distribution shows that the ground state of larger circumacene (n=13) is the ferromagnetic one with a total magnetic moment M=4 μ_B, the energetic difference between FM and AFM state is only of 15 meV for 12-circumacene. This energetic difference can be tuned up to 47 meV increasing the width of nanoestructure as in the case of (12,4) GNF, which may enables the utilization of these nanoestructures as spin logic devices at room temperature.

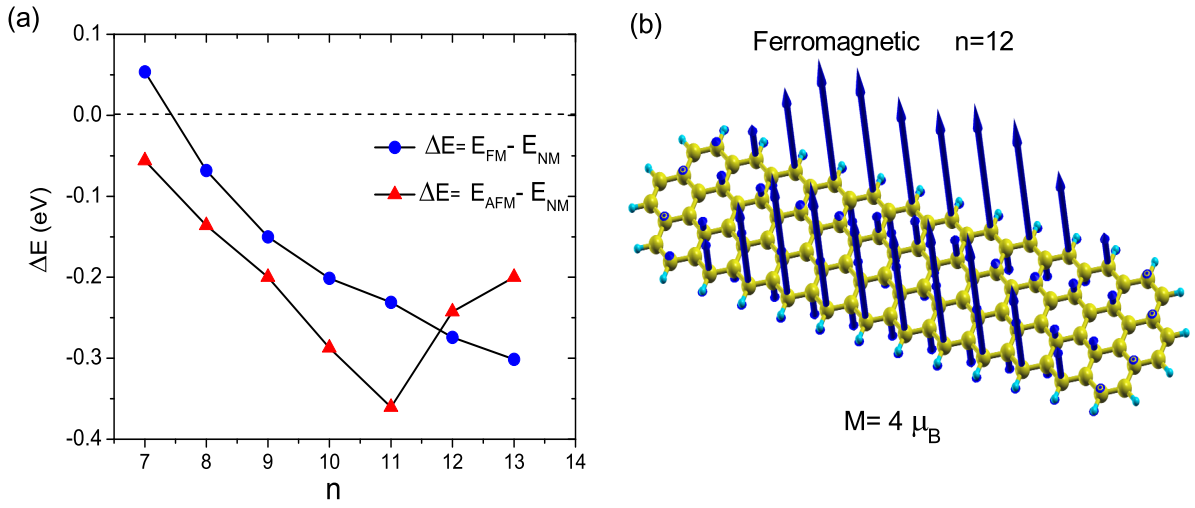

Figure 4.11: (a) Total energy difference between the AFM and NM states (red triangles) an energetic difference FM and NM states, for n-circumacenes. (b) Spin magnetization for the FM state of 12-circumacene.

Chapter 5

Results: Metal-functionalized Graphene for Hydrogen Storage

Hydrogen is one of the most promising energy carriers, particularly since its only combustion waste product is water [12, 13, 79]. Its practical exploitation, however, is hindered by several technical problems. Among these one of the most challenging is storage [12, 79]. In this respect, graphene recently attracted attention as a storage material owing to its chemical stability, low weight, and favorable physical-chemical properties for hydrogen adsorption [15, 18]. The main requirements for the success of these storing materials to utilize hydrogen as alternative energy are a gravimetric density of 7 wt % and that hydrogen should interact with the material between weak physisorption and strong chemisorption interaction. Thus, the desirable binding energy This is within an energy window of 0.2-0.6 eV/ H_2. One way to obtain this kind of interaction is by the so-called, Kubas interaction [15, 94]. Obviously, metal functionalized graphitic surfaces, flat or incurved, are natural and interesting candidates for the H_2 activation and H_2 adsorption/desorption processes. Especially since the synthesis of isolated single graphene [1], a peculiar interest in the potential applications of functionalized graphenelike materials is growing [83]. However, one of the major drawbacks in the use of metal-functionalized graphene materials for hydrogen storage is the thermodynamic tendency of transition metals (TMs) to clusterize on the surface carbon nanostructures because of the high cohesive energy of the TMs. The second problem in that kind of systems is that the desorption of metal-hydrogen complexes often also competes with the H_2 desorption. Both problems could however be reduced by increasing the binding energy of the metal atoms or small metal clusters to the supporting carbon substrate. This can be achieved by anchoring the metal atoms and small clusters to defects in the carbon networks of the graphene structure [91].

5.1 Computational details

We carried out first-principles calculations on the basis of density functional theory (DFT). [101, 102] within the generalized gradient approximation (GGA) using the exchange-correlation functional proposed by Perdew, Burke, and Ernzerhof [110] To speed up the calculations, we used norm-conserving pseudopotentials [112] as implemented in the SIESTA code [108] The Gamma point is used for the Brillouin zone sampling, and we employed a double-ζ basis function set with polarized orbitals [108], and a mesh cutoff energy of 300 Ry for the grid integration in real space. semicore states in the pseudopotential and basis set were included for titanium atoms [98]. The convergence criterion

for energy is chosen to be 10^{-4}. The structural parameters were fully optimized within a force convergence criterion of 0.01 eV/Å. Frequency calculations were carried out, in order to ensuring that the optimized structures were minima. These calculations were restricted to the small- and medium-size systems because the calculation of frequencies for the systems with more than 200 atoms demanded large computational resources. For hydrogen adsorption energies, additional calculations were undertaken by the DFT-D method, which is included [95]. A negligible contribution of less than 0.06 eV was found, and the dispersion effects were not included in most of our reported results.

5.2 Graphene monovacancy

The supporting defective graphene layer with the monovacancy was simulated as a periodically repeated unit cell consisting of 199 carbon atoms in the xy plane (Figure 5.1a).

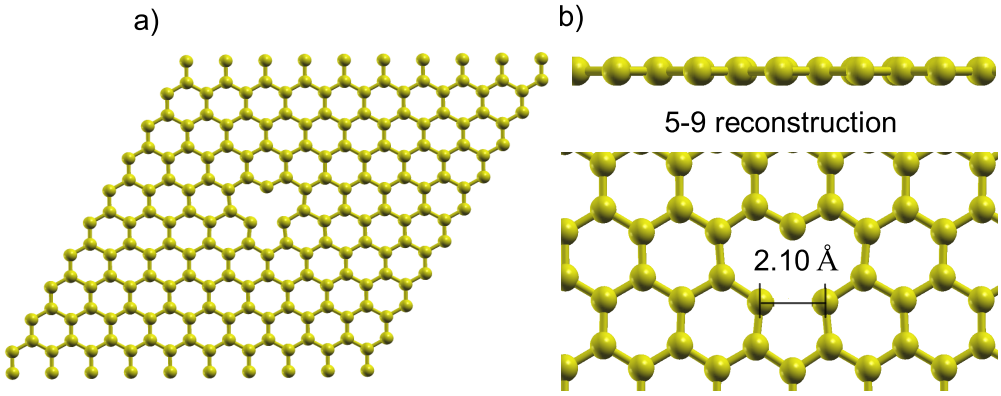

Figure 5.1: Atomic structure for a) top and b) side views of optimized graphene monovacancy. Yellow circles represent carbon atoms.

The panels (a) and (b) in Fig. 5.1 shows the atomic structure of the optimized graphene monovacancy. We did not observe a significant change in the structure beyond the defect site after one carbon atom was removed from the graphene sheet; however, in the vicinity of the vacancy there occurs a structural distortion that breaks the symmetry as a result of local bonding rearrangement. This reconstruction is known to generate a 5-9 isomer of the graphene surface [96], which presents an elongated bridge that causes the formation of two rings, with 5 and 9 atoms, respectively. Further, no significant out of the plane atomic displacements were observed in the relaxed structure. Our calculated vacancy formation energy of 7.6 eV is in good agreement with the experimental value [80] of 7.0 ± 0.5 eV and with previous calculations which give values of 7.7-7.8 eV [97] We obtain a magnetic moment of 1.26 μ_B/cell localized in the vacancy region. Earlier study have shown that the spin moment varies from 1.1 to 1.3 μ_B/cell, depending in the size of the supercell and converging toward 1.0 μ_B/cell as the supercell's size increases [97]. These results highlight the importance of using large supercells to correctly describe the ground state of the graphene monovacancies. For the large supercell size used in our calculations, our value of 1.26 μ_B/cell is in reasonable agreement with the magnetic moment reported by Palacios and Yndurain [97] for similar supercell sizes.

5.3 Pd_n clusters on graphene monovacancy

Next, we studied the bonding of Pd species to the graphence monovacancy. Fig. 5.2(a) presents the optimized structure of a single Pd atom on the defective graphene. We found that Pd forms covalent bonds with the undercoordinated C atoms at the vacancy by breaking a weak C-C bond (bond length = 2.08 Å) of one pentagon in the reconstructed vacancy. Because the Pd atomic radius is larger than that of the carbon atom, the Pd atom is displaced outward from the graphene surface, with an elevation of 1.85 Å. The three C atoms around the vacancy also move out of the graphene plane by about 0.6 Å. The interatomic distance between the Pd atom and three surrounding C atoms at the vacancy is 1.98 Å. The binding energy of a Pd atom or a Pd_n cluster to the graphene monovacancy was calculated using,

$$\Delta E(\mathrm{Pd}_n/\mathrm{GM}) = E(\mathrm{Pd}_n/\mathrm{GM}) - E(\mathrm{GM}) - E(\mathrm{Pd}_n) \tag{5.1}$$

where $n = 1$ for the case of a Pd atom, GM represents the supporting graphene monovacancy, and E indicates total energies. The calculated binding energy for a Pd atom on the graphene monovacancy is 7.5 eV, in good agreement with previous calculations of other transition metal atoms on graphene vacancies [91]. This large value of binding energy suggests that the monovacancy prevents the migration of palladium atoms on the graphene surface.

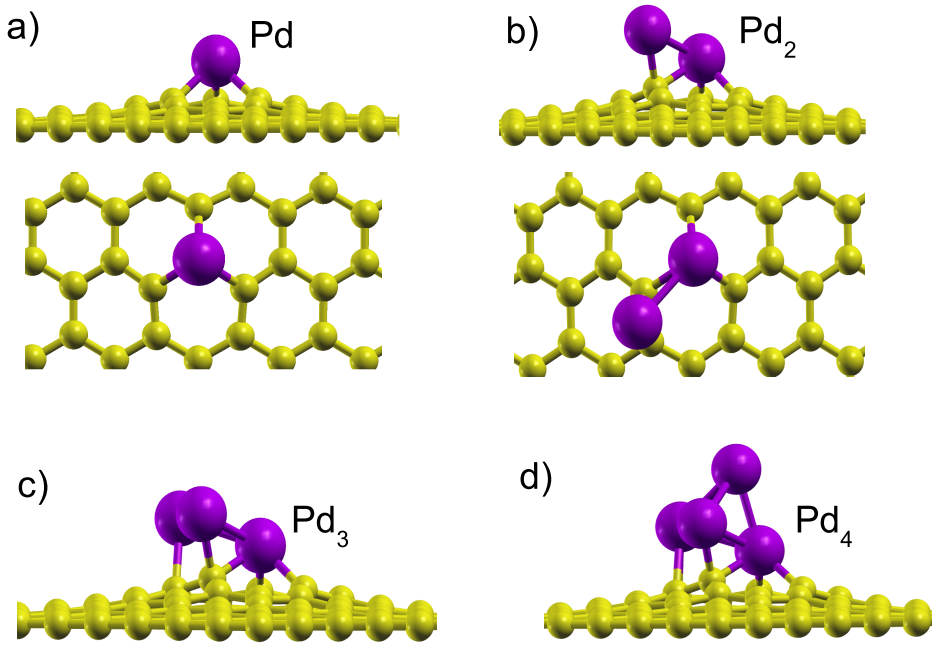

Figure 5.2: Side and top views of the relaxed structures of Pd_n (n = 1-4) clusters adsorbed on the graphene monovacancy. Yellow and purple circles represent carbon and palladium atoms, respectively.

Also shown in Figure 5.2(b)-(d) are the relaxed structures for the Pd_n (n = 2-4) clusters anchored to the monovacancy. As in the case of a single palladium atom, the

Pd clusters move out of the graphene plane in the region around the vacancy, and it is observed that the extension of the distortion is more pronounced for larger clusters. The vacancy-supported Pd_2 results by the binding of a second Pd atom on top of one of the C atoms around the vacancy and binding the first Pd atom. The calculated binding energy of Pd_2 to the vacancy is 8.6 eV. Pd_3 forms a triangle with a plane nearly parallel to the graphene layer with a binding energy of 8.30 eV. The lowest energy configuration, of the Pd_4 cluster attached to the vacancy, is a tetrahedral structure, similar to that of a free gas-phase Pd_4 cluster. The tetrahedron lies on a triangular face with one Pd atom at the center of the vacancy. The binding energy of Pd_4 to the vacancy is 7.92 eV. It is well-known that free Pd_n clusters have a magnetic moment of 2.0 μ_B [92]; however, upon chemisorption of the Pd_n clusters on the graphene vacancies, the magnetic moment is quenched because of their strong interaction with the graphene monovacancy [91].

Determining of the strength of interaction between Pd_n clusters and graphene support clusters is very important for two main reasons: First, the strength of this interaction is directly related with the mobility of the Pd_n species on the graphene surface. Given the large binding energy found, we conclude that Pd_n remains attached to the vacancy and will not diffuse on the surface, avoiding the possibility of encountering another Pd_n species and forming larger aggregates that diminish the hydrogen storage capacity thus explaining the role that defects play in the dramatic enhancement of hydrogen storage in metal-decorated graphene samples.

Second, it is well-known that the interaction strength between Pd nanoparticles and graphene support influences the adsorption and dissociation of hydrogen molecules. For example, Bhagavathi and co-workers [84] observed a dramatic increase in the hydrogen adsorption for Pd nanoparticles supported on graphene samples containing functional groups with oxygen atoms that act as bridges and increase the interaction with the Pd nanoparticles [84]. In this sense, we can ask about that ability of graphene monovacancies to mimic the effect of these functional groups. The relative stability of Pd_n cluster was quantified by means of the cluster cohesive energies, that is, the energy required to fragment a species into its atomic units. We calculate the cohesive energies for both gas-phase and supported clusters by:

$$E_C = [E(Pd_n) - nE(Pd)]/n \tag{5.2}$$

and

$$E_{C/GM} = [E(Pd_n/GM) - E(GM) - nE(Pd)]/n. \tag{5.3}$$

Here, E_C is the cohesive energy per atom of the gas-phase clusters [98], and $E_{C/GM}$ contains information about the cohesive energy of the clusters in the presence of the graphene support [99]. The results are summarized in Table 5.1. The calculated values for $E_{C/GM}$ were found to be significantly larger than those of E_C , indicating that the strong chemical interaction between Pd_n cluster and the graphene monovacancy stabilizes the supported clusters with respect to the gas-phase species; this stabilization is also in good agreement with the observed quenching of the spin magnetic moment as a consequence of the strong hybridization between Pd species and the monovacancy. Even for the clusters

Table 5.1: Calculated values of E_{C} and $E_{\mathrm{C/GM}}$ in eV for the Pd_n. clusters

n	E_{C}	$E_{\mathrm{C/GM}}$
2	-0.64	-5.11
3	-1.26	-4.54
4	-1.67	-4.02
Bulk Pd	-3.66	—

under study we can see that $E_{\mathrm{C/GM}}$ is larger than the cohesive energy of bulk Pd (see Table 5.1).

5.4 Hydrogen adsorption on the graphene-Pd species

Following our study, we investigated the effect of anchoring the Pd clusters on its capacity to adsorb H_2 molecules. The Fig. 5.3 shows the relaxed structures and adsorption energies for a single H_2 as a function of the Pd cluster size. The adsorption energy for a single H_2 on a Pd atom deposited on a pristine graphene is also given. The energy ranges for chemical and physical H_2 adsorption are marked.

The adsorption energy E_{ad} of x hydrogen molecules on the Pd_n-graphene system is given by:

$$E_{\mathrm{ad}}(x\mathrm{H_2}) = [E(x\mathrm{H_2/Pd}_n\mathrm{/GM}) - E(\mathrm{Pd}_n\mathrm{/GM}) - E(x\mathrm{H_2})]/x \tag{5.4}$$

where GM represent the graphene monovacancy, x is the number of adsorbed H_2 molecules, and $E(x\mathrm{H_2/Pd}_n\mathrm{/GM})$ is the total energy of the system formed by x hydrogen molecules adsorbed on Pd_n/GM. Our calculations show that the adsorption energy of a single H_2 on a Pd atom anchored to a graphene vacancy is 0.15 eV/H_2

This result is promising for achieving reversible adsorption/desorption of hydrogen in this system, given that as discussed before the ideal range for the absorption energy is in the range of 0.2-0.6 eV per hydrogen molecule. Note that this moderate adsorption energy of 0.15 eV contrasts with our calculated large adsorption energy of 1.25 eV on Pd-doped pristine graphene. As seen in Figure 5.3b, the adsorption energy of a single H_2 increases when increasing the Pd cluster size, up to a value of around 1.2 eV for Pd_4. This high absorption energy for Pd_4 is already in the range of chemisorption above of the optimal energetic window for hydrogen storage. The calculated bond length for the adsorbed H_2 ranges from 0.76 Å in the case of adsorption on single Pd up to 0.96 Å when supported on Pd_4; these bond lengths are typical of the Kubas-type complex indicating that the interaction between clusters and graphene monovacancy favors activation of hydrogen molecules in contrast with the adsorption of H_2 on Pd_n/pristine graphene where a complete dissociation of H_2 occurs causing the formation of hydrides.

Despite the fact that the large binding energies found so far can be daunting for practical purposes, we considered that there are two additional questions that must be addressed in the theoretical modeling of nanomaterials for hydrogen storage. The first one is related to the fact that metal clusters can attach hydrogen molecules in different sites and thus present different adsorption energies. Therefore, the energy cost to remove

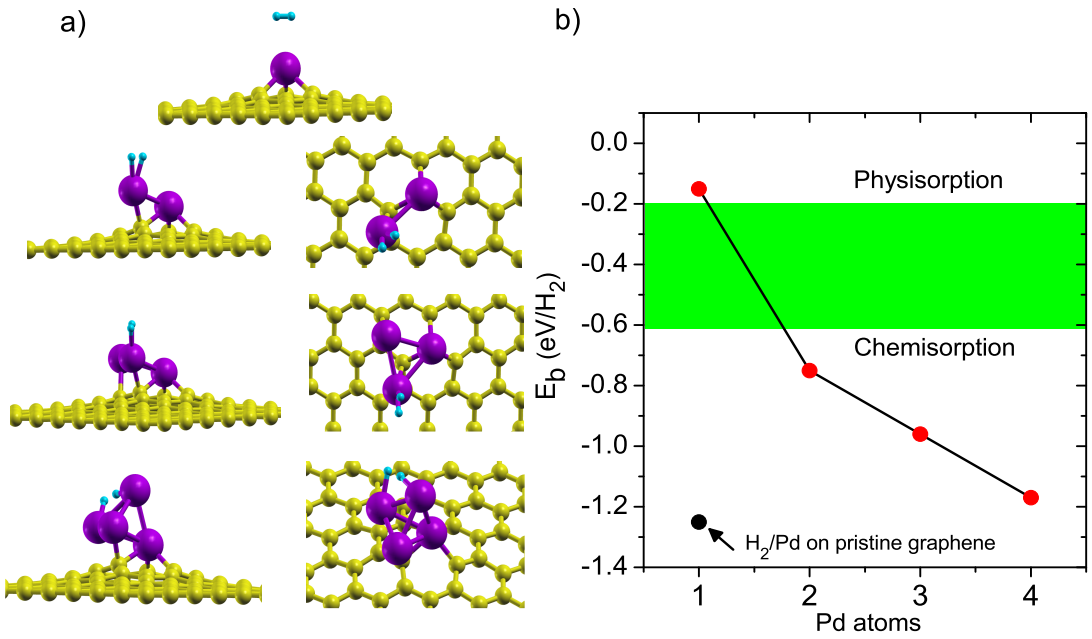

Figure 5.3: a) Relaxed structures and b) variation of the adsorption energies for a single H_2 on the graphene supported Pd_n (n = 1-4) clusters as a function of cluster size. Yellow, purple and light brown circles represent carbon, palladium and hydrogen atoms, respectively. The optimum energy range for reversible H_2 absorption/desorption is marked in a green rectangle.

hydrogen from the cluster may be different depending in the position where it attaches to the metal cluster. The second factor to take into account is the possibility of the absorption of multiple H_2 in a given Pd cluster. Two important questions rise in this case: (i) What is the maximum number of H_2 that can bind to a given Pd cluster? and (ii) How is the absorption energy affected by the attaching of multiple hydrogen molecules? We expect that the number of adsorbed H_2 increases with increasing the size of the cluster and at the same time that the binding strength decreases with the grade of H_2 saturation of the active site. Furthermore, if the binding energy decreases with the number of H_2 molecules, then the question arises whether we can have a system that presents both a large H intake and a binding energy that lies in the ideal range for an efficient cyclic adsorption/desorption process at room temperature and moderate pressures.

5.5 Adsorption sites on the supported clusters

In Fig. 5.4, we present the site dependence of the hydrogen average adsorption energy for the larger cluster under study (Pd_4). For this cluster we found four possible adsorption sites, which were labeled as edge 1-3 and apical, illustrated in Fig. 5.4. The edge 1 and 2 sites were found to be the lowest energetic configurations with the same adsorption energy of 1.17 eV/H_2, the edge 3 site resulted in the highest energy configuration with a computed energy difference of 0.5 eV with respect to edge 1 and 2 isomers, and the apical site is only 0.2 eV above the lowest energy configuration. Similar searches were repeated for smaller clusters. Thus, all the configurations presented in Figure 3 correspond to the lowest energy structures for each case after a full geometry optimization.

The Figure 5.4 shows that the H_2 binds to supported Pd_4 cluster preferently as kubas-

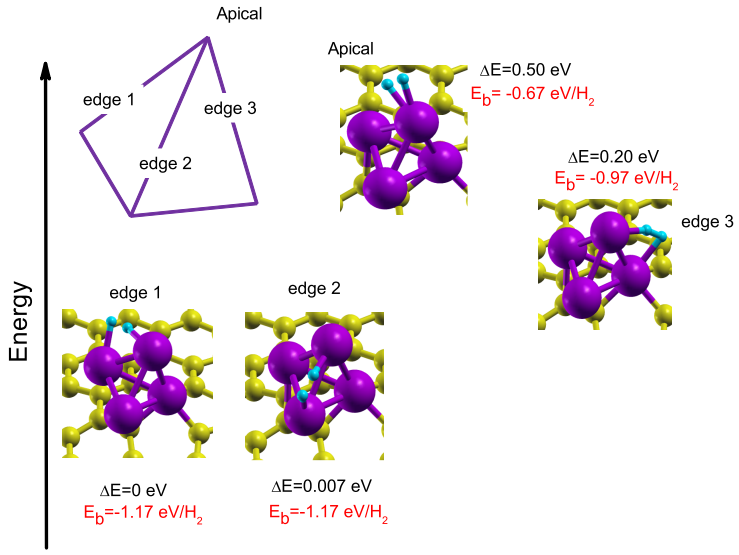

Figure 5.4: Relaxed structures for the adsorption of H_2 on the graphene-supported Pd_4-cluster at the edge 1-3 and apical sites of the cluster; the relative energies (ΔE) and H_2 adsorption energy (E_b) for each isomer in eV are also given.

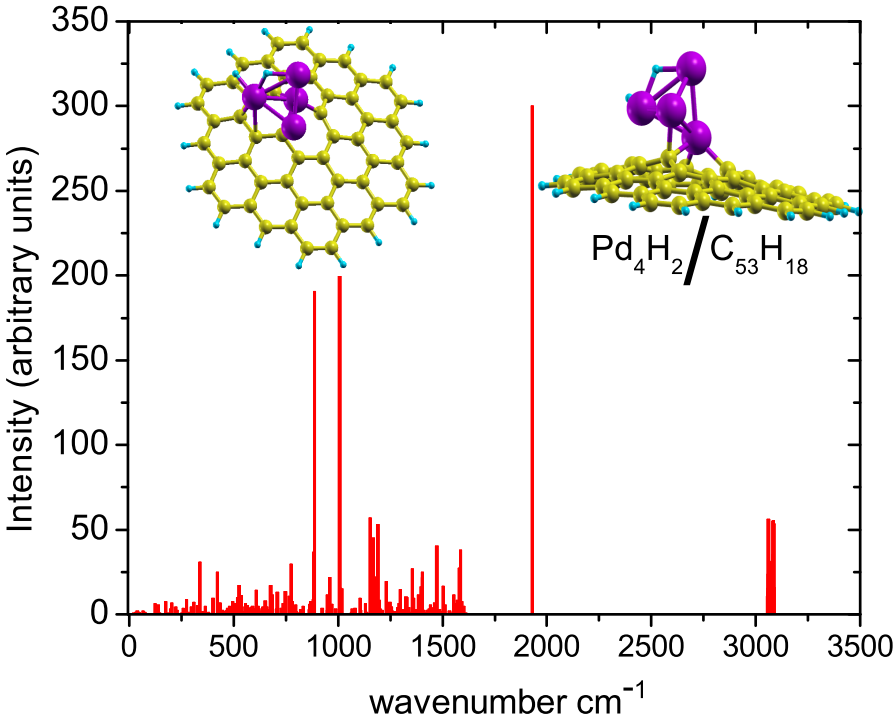

Figure 5.5: Calculated vibrational frequencies and intensities for $Pd_4(H_2)/C_{53}\ H_{18}$ cluster model. The lowest calculated frequency is 20.30 cm^{-1}. The positive values for the 3N-6 vibrational modes indicates that the structure is an energy minimum.

type complex independently of the adsorption site. In strict sense, calculations of vibrational frequencies are needed in order to show that the lowest-enery structure in Figure 5.4 is a true energy minimum. however the calculation of vibrational frequencies for an system of more than 200 atoms is computationally expensive, For that reason we performed geometry optimization and frequency calculations for a smaller $Pd_4(H_2)$ on C_{53} H_{18} graphene nanoflake with a vacancy. From Figure 5.5 we can see that the formation of the kubas-type complex is favored on graphene nanoflake as in the case of $Pd_4(H_2)$ on 10×10 graphene supercell with a vacancy. Furthermore, in Figure 5.5 we present the calculated vibrational frequencies and intensities for $Pd_4(H_2)/C_{53}$ H_{18} cluster model. The lowest calculated frequency is 20.30 cm^{-1}. The positive values for 3N-6 vibrational modes indicates that the structure is a energy minimum.

5.6 Hydrogen saturation of gas-phase and supported clusters

Understanding the key factors that determine the adsorption of a single H_2 on Pd_n clusters allows us to gain insight for such interactions. However, for a more realistic modeling, the role of the catalyst (Pd particles in our case), the hydrogen saturation, and the variation in the H_2 binding energy should be addressed. Saturation of the catalyst plays a central role in the study of adsorption of molecular species. With this aim, we analyzed the variation in the H_2 absorption sequential energies, ΔE_x, defined as:

$$\Delta E_x = E(xH_2/\mathrm{Pd}_n/\mathrm{GM}) - E((x-1)H_2/\mathrm{Pd}_n/\mathrm{GM}) - E(\mathrm{H}_2) \tag{5.5}$$

We note that ΔE_x differs from the definition given for E_{ad}, which represents an average adsorption energy, because it is generally compared with the thermodynamic estimations of adsorption energies [92, 93]. However, ΔE_x can be a good descriptor for the grade of saturation on the basis of the definition of eq. 5.4; a value for $\Delta E_x > 0$ indicates that the adsorption of H_2 is energetically unfavorable.

To investigate the effect of the vacancy on the successive H_2 absorption on the Pd clusters, we first studied the successive addition of H_2 molecules to free gas-phase Pd_n (n= 1-4) species. Thus, to this end, a H_2 molecule was approached to the metal particle from several initial configurations, and a full geometry optimization was carried out. The hydride structure was found to be more stable by 0.09 eV than the Kubas on the isolated Pd, and the vibrational frequencies presented in Table B1 in appendix B shows both structures are minima. The process was successively repeated on the most stable geometries found by approaching additional H_2 molecules to Pd atom followed by geometry optimizations. Fig. A1 in appendix A show the relaxed structures for gas-phase $Pd(H_2)_x$ with x = 1-4 clusters. Furthermore, vibrational frequencies for are presented in Table B1 in appendix B, showing that the calculated structures fro $Pd(H_2)_x$ are energy minima. In Table 5.2 we can see the calculated values of ΔE_x for $Pd(H_2)_x$ clusters in gas phase and for supported Pd atom on graphene monovancy being evident tha dramatic effect of the graphene monovacancy on the hydrogen uptake of single Pd atom.

The Table 5.3 shows the calculated values for of ΔE_x for $Pd_2(H_2)_x$ clusters in gas phase and supported on graphene monovacancy Fig. A2 in appendix A show the relaxed structures for gas-phase $Pd(H_2)_x$ with x = 1-4 and supported $Pd(H_2)_x$ with x = 2-3

Table 5.2: Calculated values of the H_2 sequential energy ΔE_x (eV) for the gas phase and graphene anchored $Pd(H_2)_x$ clusters as a function of the number of H_2. Relaxed estructures are showed in Fig. A1 in appendix A. Calculated vibrational frequencies are presented in Table B1 in appendix B.

n	Gas-phase	Supported
1	-1.1	-0.15
2	-0.92	—
3	-0.67	—
4	-0.40	—

cluster. Furthermore, vibrational frequencies for $Pd(H_2)_x$ with x = 1-3 in gas phase are presented in Table B2 in appendix B, showing the stability of the mentioned Pd-H species.

Table 5.3: Calculated values of the in the H_2 sequential energy ΔE_x (eV) for the gas phase and graphene anchored $Pd_2(H_2)_x$ clusters as a function of the number of H_2 molecules. Relaxed estructures are showed in Fig. A2 in appendix A. Calculated vibrational frequencies for selected clusters in gas phase are presented in Table B2 in appendix B.

n	Gas-phase	Supported
1	-2.2	-0.75
2	-1.15	-0.63
3	-0.95	-0.20
4	-0.30	—

The Table 5.4 shows the results for of ΔE_x for $Pd_3(H_2)_x$ clusters in gas phase and supported on graphene monovacancy Fig. A3 in appendix A show the relaxed structures for gas-phase $Pd(H_3)_x$ with x = 2-3 and supported $Pd(H_2)_x$ with x = 2-3 cluster. Furthermore, vibrational frequencies for $Pd(H_2)_x$ with x = 1-3 in gas phase are presented in Table B3 in appendix B, showing the stability of the mentioned Pd-H species. The hydrogen sequential energies (ΔE_x) were then calculated using eq 5.5 and are reported in Tables 5.2-5.4. As expected, the number of adsorbed H_2 increased with the particles size, whereas ΔE_x for hydrogen molecules decreases with the number of H_2 attached to the Pd species.

Motivated by these results, we focused our study on the Pd_4 cluster. The gas-phase cluster was found to dissociate an initial H_2 molecule without an energy barrier. Additional molecules were further attached without dissociation until achieving saturation of the first shell around Pd after 8 H_2 molecules as presented in Figure 5.6. Furthermore, calculated vibrational frequencies for selected clusters Pd_4H_2, $Pd_4(H_2)_2$, $Pd_4(H_2)_3$ and $Pd_4(H_2)_7$ in gas phase are presented in Table B4 in appendix B. We then analyzed the successive addition of H_2 molecules to the Pd_4 graphene-anchored cluster. Figure 5.7 presents the relaxed structures from two to seven adsorbed H_2 molecules on Pd_4. It is found that when the H_2 molecules interact with the deposited Pd_4 cluster, most of them bind in molecular form, although the interaction strength between Pd_4 and H_2 depends on the number of adsorbed molecules. The hydrogenation process continued until achieving saturation. We found that in the case of the Pd_4 cluster anchored on the graphene

Table 5.4: Calculated values of the H_2 sequential energy ΔE_x (eV) for the gas phase and graphene anchored $Pd_3(H_2)_x$ clusters as a function of the number of H_2 molecules. Relaxed estructures are showed in Fig. A3 in appendix A. Calculated vibrational frequencies for selected clusters in gas phase are presented in Table B3 in appendix B.

n	Gas-phase	Supported
1	-1.6	-0.96
2	-1.32	-0.68
3	-0.63	-0.17
4	-0.61	—
5	-0.54	—
6	-0.32	—

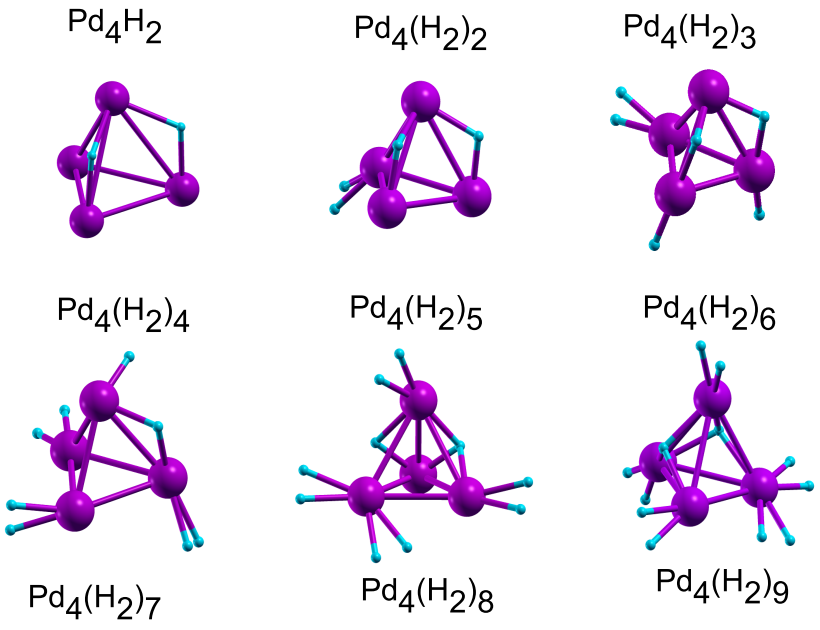

Figure 5.6: Relaxed structures for the H_2 adsorption at the Pd_4 cluster in the gas-phase, $Pd_4(H_2)_x$ with x = 1-9. Calculated vibrational frequencies for selected clusters Pd_4H_2, $Pd_4(H_2)_2$, $Pd_4(H_2)_3$, and $Pd_4(H_2)_7$ in gas phase are presented in Table B4 in appendix B.

monovacancy, saturation occurs after adsorbing only four H_2 molecules because the fifth and further H_2 molecules do not directly bind to the Pd cluster and remained practically unaltered with respect to isolated H_2. These unattached H_2 molecules form a second shell around the Pd_4 that lies more than 2.5 Å away from the metallic atoms of the saturated cluster.

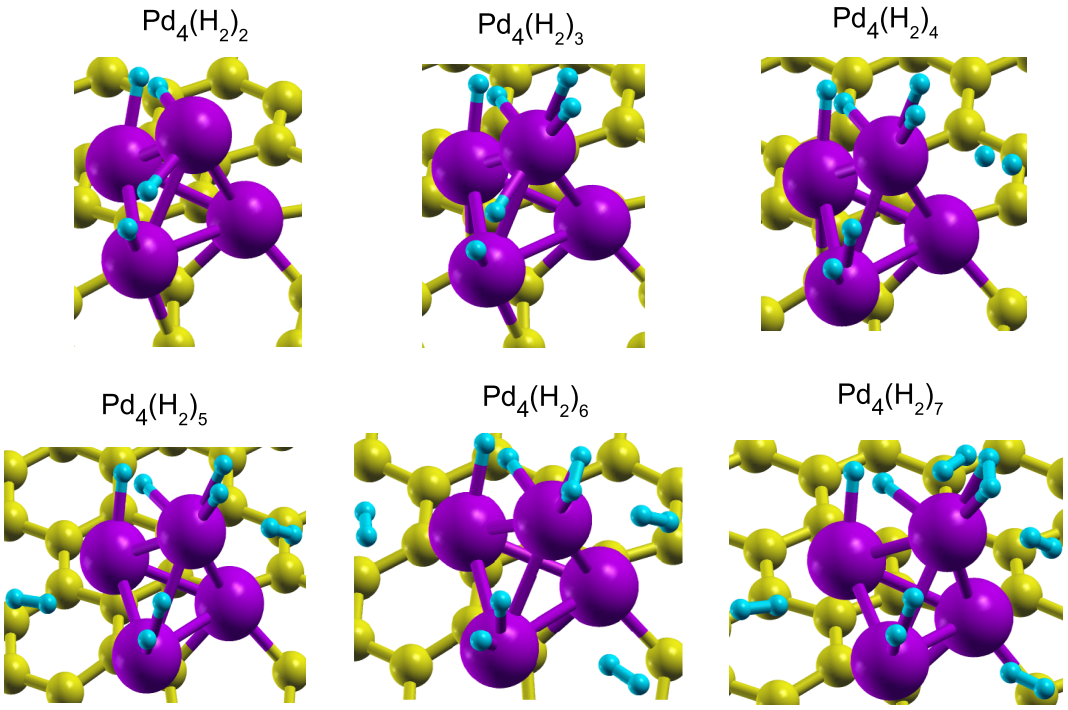

Figure 5.7: Relaxed structures for the H_2 adsorption on the supported Pd_4 cluster, $Pd_4(H_2)_x$ with x = 1-7.

Despite the fact that adsorption of multiple H_2 does not distort the tetrahedral geometry of the Pd_4 cluster in a noticeable way, a strong influence on it was again found on the hydrogen-metal interaction, caused by the hybridization between the carbon surface and the Pd atoms. Figure 5.8a presents the changes in the adsorption energies for both the gas-phase and the graphene-anchored Pd_4. It is found that for both cases the first H_2 dissociates on the Pd_4 cluster forming a hydride with a larger binding energy of 1.4 and 1.2 eV for the gas-phase and deposited cluster, respectively. This large energy shows a strong chemisorptive interaction. The second molecule is adsorbed with an energy of 0.9 and 0.6 eV for the free and deposited cluster, respectively. Notably, although a value of ΔE_x for the free Pd_4 in the range of 0.7 to 0.30 eV is found from the third until the ninth hydrogen molecule, in the case of the vacancy-deposited cluster, the fourth H_2 already shows a moderate energy of only 0.37 eV. Furthermore, from the fifth H_2 onward, H_2 molecules show lower adsorption energies nearer to the range of physisorption, for example, the seventh adsorbed molecule shows a value of ΔE_x = -0.085 eV, in this case dispersion van der Waals corrections were taken in to account with a contribution of around 0.06 eV respect to calculation without dispersion effects.

Despite the low value for ΔE_x, the adsorption of hydrogen molecules is still $\Delta E_x < 0$. These results attest to the important role of the graphene vacancy on modulating the adsorption energies. Figure 5.8b presents the optimized $Pd_4(H_2)_7$ cluster.

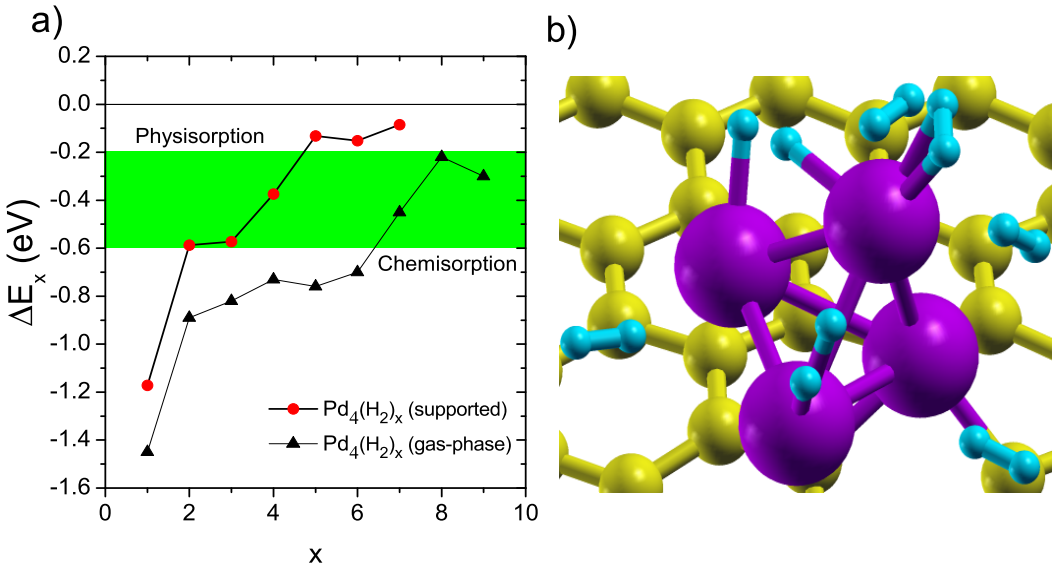

Figure 5.8: a) Evolution of the sequential energy for the gas-phase and graphene-anchored $Pd_4(H_2)_x$ clusters as a function of the number of H_2 molecules. A value for $\Delta E_b > 0$ indicates that adsorption is energetically unfavorable. b) Relaxed atomic structure for supported $Pd_4(H_2)_7$

5.7 Average adsorption energies

In the previous section, we have shown that the supported Pd_4 cluster can covalently bind a total of four H_2 molecules, or one H_2 per Pd atom, and that the remaining hydrogen molecules are weakly physisorbed with energies around 0.1 eV. Now we are interested in evaluating and analyzing the average binding energy with respect to multiple hydrogen adsorption. The average H_2 binding energy is defined in eq 5.4 and is a good descriptor of the interaction strength of the clusters with the adsorbed molecules; for this reason, it is directly compared with thermodynamics estimations for an ideal adsorption energy range [93]. However, we should caution the reader about this concept, namely, that this quantity cannot be used for situations where two adsorption regimes are present, as in our case. For example, the calculated average binding energy of a supported $Pd_4(H_7)$ cluster is 0.40 eV/H_2, which seems reasonable for the first four molecules, but it is hard to believe that this is a realistic estimate for the adsorption energy of weakly adsorbed H_2, especially considering that these H_2 molecules form a second shell around the supported Pd_4 that lies more than 2.5 Å away. In other words, when chemisorbed and physisorbed species coexist in the system, eq 5.4 causes the overestimation of the adsorption energy for the weakly adsorbed species. Furthermore, it is desirable to analyze the opposite case. As mentioned earlier, the binding energy of a single H_2 adsorbed on a supported Pd_4 cluster is 1.20 eV/H_2; if a second H_2 is adsorbed, then we can question how the adsorption of the second molecule influences the binding energy of the first one. The large value for $\Delta E_x = 0.6$ eV for the second is related to the reduction of the system stability upon the adsorption of the second molecule, so we can assume that the binding energy of the first molecule is not more 1.2 eV. Thus, in this case the average adsorption energy is a good descriptor of the interaction strength between adsorbed molecules and the catalyst. Similar arguments can be provided for the adsorption of the third and fourth molecules because the calculated values for ΔE_x are relatively large; however, for weak interacting

molecules we cannot expect a strong influence on the adsorption energy of the previous one. In consequence, the average binding energy is not a meaningful stability descriptor. For these reasons, in Table 5.5 we summarized the calculated values of E_b for Pd_2, Pd_3, and Pd_4, excluding the calculated values for physisorbed species ($\Delta E_x < 0.2$ eV).

Table 5.5: Calculated values of E_b (in eV/H_2) for supported Pd_2, Pd_3, and Pd_4 clusters.

n	Pd_2	Pd_3	Pd_4
1	-0.75	-0.96	-1.20
2	-0.70	-0.68	-0.65
3	—	—	-0.57
4	—	—	-0.50

The calculated values for Pd_2 and Pd_3 show that these species interact strongly with two H_2; however, the adsorption energy is still far away from the optimal range for hydrogen storage. In contrast, supported Pd_4 is able to attach up to four H_2 molecules with an adsorption energy of 0.50 eV/H_2, which is in the optimal energy range for an efficient cyclic adsorption/ desorption process at room temperature and moderate pressures. The adsorption energy of hydrogen on Pd-doped graphene samples has been measured in the range of 7-12.5 kJ/mol (0.26-0.54 eV) [84] for samples with a H_2 gravimetric content of 0.20-0.70 wt % at moderate pressures.

5.8 Hydrogen adsorption on supported Ni_4 and Ti_4 clusters

A question of vital importance and which is rarely mentioned is the effect of the nature of the transition metal on the hydrogen gravimetric content. In previous sections we have showed that a Pd_4 cluster supported on a graphene monovacancy is able to adsorb up to four H_2 with moderate binding energies such that the ratio between the number of adsorbed hydrogen molecules and Pd atoms on the clusters surface is 1 [130]. This result has been further corroborated by Granja and co-workers for the case of Pd_6 supported on a graphene monovacancy [131]. Although these results are encouraging, our estimations, based on first-principles calculations, determined a maximum gravimetric content for the Pd_4/graphene system of only 0.65 wt % which is in reasonable agreement with experiments [15, 84] but it is still far from the ideal gravimetric content of 7.5 wt %.

Experimental and theoretical studies have suggested that the main limitation of Pd_n-graphene systems for hydrogen storage is not the H_2 adsorption energy per se, but the metals atomic weight and the number of hydrogen molecules that it can adsorb up to saturation. In this sense, it is reasonable to think about using lighter transition metal clusters as an alternative to solve the problem. Nickel is a promising candidate; it weighs about half as much as Pd and is well-known for its catalytic properties. Unfortunately, previous experiments on graphene decorated with monodispersed Ni nanoparticles showed a hydrogen content of only 0.5 wt % at moderate pressures [132], a value that is similar to the one measured in Pd-decorated graphene. This result supports the idea that large metal nanoparticles are not good candidates for maximum hydrogen uptake, and that the effect of the metal dopant enhancing the hydrogen adsorption would be largest for maximum

dispersion, that is, when single metal atoms or very small clusters are present [15, 17].

Another potential candidate is Ti. Recently, an interesting result has been reported by Mashoff and co-workers where the formation of titanium-islands on graphene as a function of defect density was investigated [133]. When depositing titanium on pristine graphene, titanium forms islands with an average diameter of about 10 nm and an average height of a few atomic layers. In contrast, if defects are introduced in the graphene by ion bombardment, the mobility of the deposited titanium atoms is reduced, and the average diameter of the islands decreases to only 5 nm. Furthermore, these islands present a single layer monatomic height that increases the titanium surface available per unit of graphene area and have a gravimetric density between 0.75 and 2.5 wt % depending on the surface coverage. These results show how the lattice engineering in graphene surfaces is a promising route to enhance their catalytic properties by maximizing the dispersion of metal dopants, and hence the surface coverage. Based on these reports we consider that studying the adsorption of hydrogen on small graphene supported $3d$ transition metal clusters is of great relevance toward the design of novel graphene based materials with tailored properties.

Motivated by the recent experiments of the H_2 adsorption on Ti and Ni graphene supported nanoparticles [132, 133], in this section we provide a detailed description of the interaction of H_2 with atomic and Ti_4- and Ni_4-doped defective graphene.

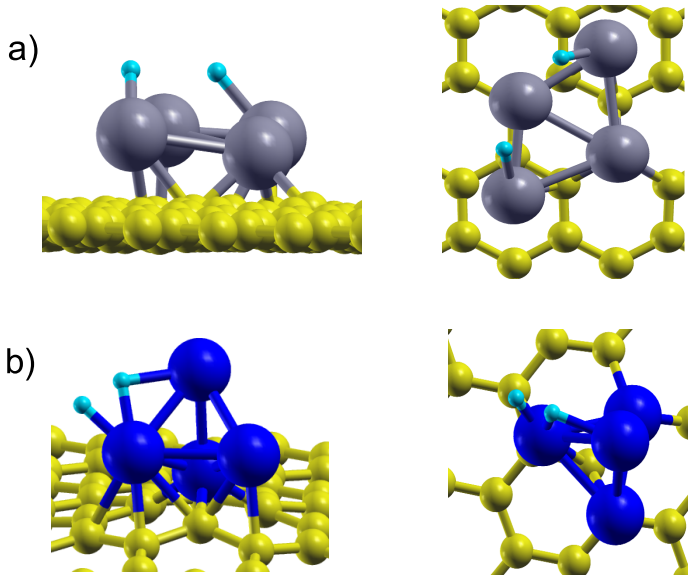

Figure 5.9: Relaxed structures for the H_2 adsorption on the supported a) Ti_4 and b) Ni_4 clusters.

The Figure 5.9 shows the relaxed structures and adsorption energies for a single H_2. The adsorption energy (ΔE_{ad}) of x hydrogen molecules on the M_4-graphene system is given by:

$$\Delta E_x = E(x\mathrm{H_2/Pd}_n/\mathrm{GM}) - E((x-1)\mathrm{H_2/Pd}_n/\mathrm{GM}) - E(\mathrm{H_2}) \tag{5.6}$$

Here M could be Ti or Ni, GM represents the graphene monovacancy, x is the number

of adsorbed H_2 molecules, and $E(xH_2/M_4/GM$ is the total energy of the system formed by The x hydrogen molecules adsorbed on M_4/GM. The H_2 adsorption on supported clusters is far stronger with calculated energies ranging from 1.0 and 1.6 eV for Ni_4 and Ti_4, respectively. It is interesting to note that the difference in binding energies between Ti_4 and Ni_4 is reflected in the way in which the H_2 adsorbs on the cluster; for Ti_4 the complete dissociation of H_2 is favored, while Ni_4 prefers the formation of Kubas-type complexes, and this result is similar to the one previously found for supported Pd_4 cluster in which case we found a H_2 adsorption energy of 1.2 eV [130]. This high absorption energy for Ti_4 and Ni_4 is already in the range of chemisorption above of the optimal energetic window for hydrogen storage of 0.2 to 0.6 eV per H_2 molecule. The calculated bond length for the adsorbed H_2 ranges from 0.85 Å in the case of adsorption on Ni_4, a bond length that is typical of Kubas-type complexes [87], to 2.5 Å for the case of H_2 adsorbed and dissociated on Ti_4, thus indicating that interaction between Ti_4 cluster and the graphene monovacancy favors hydride formation. The formation of hydrides in titanium clusters is very interesting as this is known to be the first step for the hydrogen spillover mechanism that only occurs with the complete dissociation of H_2 molecules on catalysts surface [131].

To investigate the rational for the difference on the H_2 absorption of Ti_4/GM, i.e., complete dissociation, versus Ni_4/ GM, where Kubas-type complexes are present, we calculated the partial density of states for $H_2/Ti_4/GM$ and $H_2/Ni_4/GM$. As shown in Figure 5.10 the Ti 3*d* states are located below and above the Fermi level and exhibits a strong interaction with the hydrogen 1*s* levels which leads to the hydrogen dissociation upon absorption. On the other hand, the Ni 3*d* levels are located below the Fermi level and the hydrogen 1*s* levels only interact with the Ni 4*s* levels, thus explaining the formation of the Kubas-type complexes.

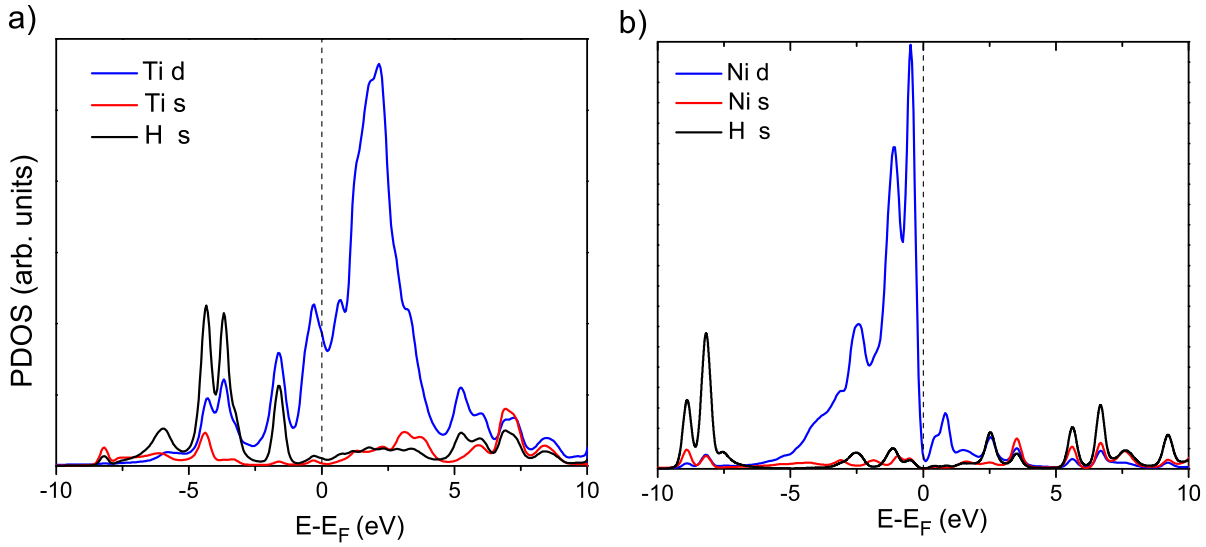

Figure 5.10: Partial density of states for a) $H_2/Ti_4/GM$ and b) $H_2/Ni_4/GM$.

Understanding the key factors that determine the adsorption of a single H_2 on metal clusters allows gaining insight of such interactions. However, for a more realistic modeling the role of the active sites (Ti_4 and Ni_4 clusters in our case), the hydrogen saturation, and the variation in the H_2 binding energy should be addressed. Saturation of the catalyst

plays a central role in the study of adsorption of molecular species. With this aim we analyzed the variation in the sequential H_2 absorption energies ΔE_x as defined in eq 5.6. As we have noted in section 5.6, a value for $\Delta E_x > 0$ indicates that the adsorption of H_2 is energetically unfavorable.

We then analyzed the successive addition of H_2 molecules to the Ti_4 anchored cluster. Figure 5.11 presents the relaxed structures for three, six, and eight adsorbed H_2 molecules on Ti_4 . It is found that when the first three H_2 molecules interact with the deposited Ti_4 cluster most of them bind in dissociative form (see Figure 5.11a), although the interaction strength between Ti_4 and the first three H_2 molecules slightly depends on the number of adsorbed molecules, resulting that ΔE_x with $x = 1$ to 3, ranges from 1.6 to 1.2 eV. The adsorption of another three molecules is favored by the formation of Kubas complexes as seen in Figure 5.11b, with ΔE_x energies between 0.50 and 0.25 eV and H-H bond lengths of 0.8 Å. It is found that Ti_4 achieves saturation with 6 adsorbed molecules, as after adding two more H_2 molecules a weakly physisorption is observed with ΔE_x energies of less that 0.2 eV, and in which the additional H_2 molecules lay more than 2.5 Å away from the Ti_4 cluster (Figure 5.11c).

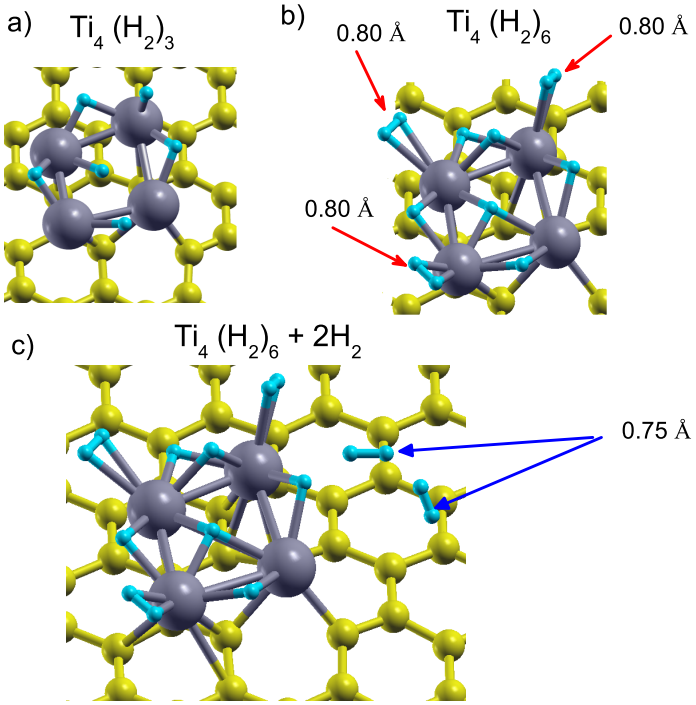

Figure 5.11: Relaxed structures for the hydrogen saturation of supported Ti_4/GM. a) Geometry after the adsorption of three H_2 molecules, b) after the adsorption of six H_2 molecules, and c) after the adsorption of eight H_2 molecules.

In contrast to the case of the supported Ti_4 cluster, in the case of Ni_4 anchored on the graphene monovacancy saturation occurs after adsorbing only three H_2 molecules and with the forming of Kubas type complexes. The fourth H_2 molecule does not directly bind to the Ni_4 cluster and remains practically unaltered with respect to isolated H_2 (Figure 5.12). This unattached H_2 situates more than 3.0 Å away from the supported cluster atoms. In general, the adsorption of multiple H_2 does distort neither the planar nor the tetrahedral geometries of the Ti_4 and Ni_4 in a noticeable way. However, a strong influence

was again found on the hydrogen-metal interaction caused by the hybridization between the carbon surface and the metal atoms.

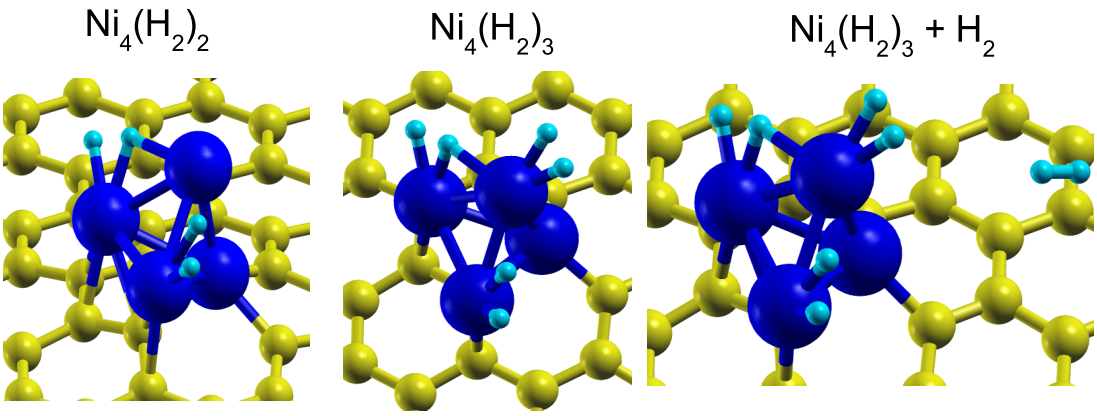

Figure 5.12: Relaxed structures for the saturation of graphene supported Ni_4/GM.

Figure 5.13a presents the calculated ΔE_x as a function of the number of adsorbed H_2 for the supported Ti_4 and Ni_4 clusters. We have also included the results discussed above for the supported Pd_4 cluster. Since Pd and Ni belong to the same group of the periodic table, it is interesting to compare the H_2 saturation of Pd_4 and Ni_4 clusters to evaluate the effect of the atomic radius on the hydrogen adsorption. We can see in Figure 5.13a that the values of ΔE_x for Ni_4 are slightly smaller than those calculated for Pd_4. This result can explain why Pd_4 reaches saturation with four H_2 molecules while Ni_4 only can attach up to three molecules before saturation. On the other hand, the values of ΔE_x for H_2 on Ti_4 vary from 1.6 eV for a single H_2 up to 0.1 eV for the eighth adsorbed molecule. From the calculated values for ΔE_x and the atomic structure seen in Figure 11b, we can conclude that Ti_4 is able to attach up to 6 molecules before the saturation. Figure 5.13b shows the average H_2 adsorption energy at the saturation point. Our results predicts that Ti_4, and Pd_4 exhibit similar average adsorption energies 0.53 and 0.56 eV/H_2, respectively, while Ni_4 have slightly smaller value of 0.42 eV/H_2. Importantly, all atomic clusters under study, i.e., Ti_4 , Pd_4 , and Ni_4 , are able to attach H_2 molecules with an average adsorption energy between 0.2 and 0.6 eV/H_2, which is in the optimal energy range for an efficient cyclic adsorption/desorption process at room temperature and moderate pressures.

5.9 Hydrogen gravimetric content

We have showed that the interaction between the graphene monovacancy and the transition-metal clusters under study lead to H_2 adsorption energies within the ideal range for practical hydrogen storage; however, it is also important to analyze the hydrogen gravimetric content (wt %). For the estimation of wt % we have used the method recently proposed by Mashoff and co-workers [133], that method is convenient as it involves parameters that can be determined from the optimized geometries. These include the maximum number of loaded hydrogen molecules per metal atom in the cluster, the surface particle density, which can be evaluated from the clusters interatomic distances, the fraction of metal atoms in the clusters surface, and the exposed metal-surface to total graphene to surface ratio. All these quantities can be evaluated directly from our first-principle calculations.

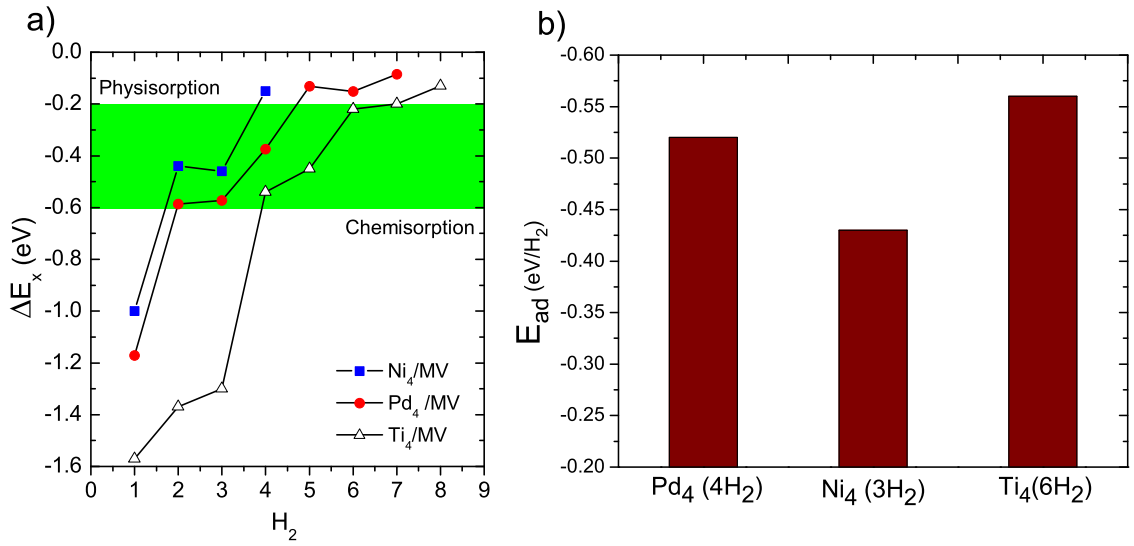

Figure 5.13: a) Calculated values for the sequential H_2 adsorption energy for graphene anchored $Ti_4(H_2)_x$/GM, $Ni_4(H_2)_x$/GM and $Pd_4(H_2)_x$/GM clusters as a function of the number of H_2 molecules. Values of $\Delta E_x > 0$ indicate that adsorption is energetically unfavorable. b) Average adsorption energy of H_2 molecules at the saturation for $Ti_4(H_2)_6$/GM, $Ni_4(H_2)_3$/GM and $Pd_4(H_2)_4$/GM.

The detailed description of the estimation of the wt % for the Ti_4-, Ni_4-, and Pd_4-doped defective graphene is given in the Appendix C. Figure 5.14 summarizes the calculated hydrogen gravimetric content for the systems under study, and includes a comparison with experimental reports of graphene-decorated samples. Palladium decorated graphene is by far the most studied system for hydrogen storage, in in previous experimental works the measured gravimetric content at moderated pressures and room temperatures was estimated to be 0.30% by Contescu and co-workers [15] and 0.75 wt % as reported by Vinayan and co-workers [84]. It is important to mention that in Contescus experiments the graphene samples were decorated with well dispersed palladium atoms, in fact, they reported that 18% of the adsorbed palladium was in the form of single atoms, and the rest in the form of $PdH_{0.6}$ species, which could be explained by the adsorption of H_2 on small Pd clusters. On the other hand, in Vinayan's experiments [84] the formation of Pd nanoparticles, which may indeed favor the H_2 absorption, was reported. In this case the hydrogen gravimetric content was twice as large as in the experiments with well-dispersed atoms. Our calculated value of 0.64% for Pd_4-doped graphene cluster is in good agreement with the experimental report [15, 84]. Furthermore, our results suggest that the gravimetric content is mainly determinate by the ratio between the surface clusters atoms and the maximum number of adsorbed H_2 molecules, which is 1:1 for the case of $Pd_4(H_2)_4$ on defective graphene. Actually, this ratio is predicted to be independent of the metal clusters size, a conclusion supported by the recent work of Granja and co-workers [131]. In the case of the Ni_4-doped graphene our predicted value of 0.30 wt% is slightly smaller than the one reported by Gaboardi of 0.40 wt% for Ni nanoparticles on graphene [132]. It is interesting to note that, despite the fact that Ni is a lighter element than Pd, both the experimental and theoretical values predicts similar values of wt%. Our calculations show that the reason of this low hydrogen gravimetric content is the lower ratio between the maximum number of adsorbed H_2 to the number of metal atoms, which is only 0.75:1

in the case of $Ni_4(H_2)_3$ defective-graphene, that is, smaller than the one found for the case of Pd. On the other hand, Ti_4-doped graphene shows a most interesting behavior. Ti_4 reaches saturation after adsorbing six hydrogen molecules leading to a H_2:Ti ratio of 1.5:1 [134].

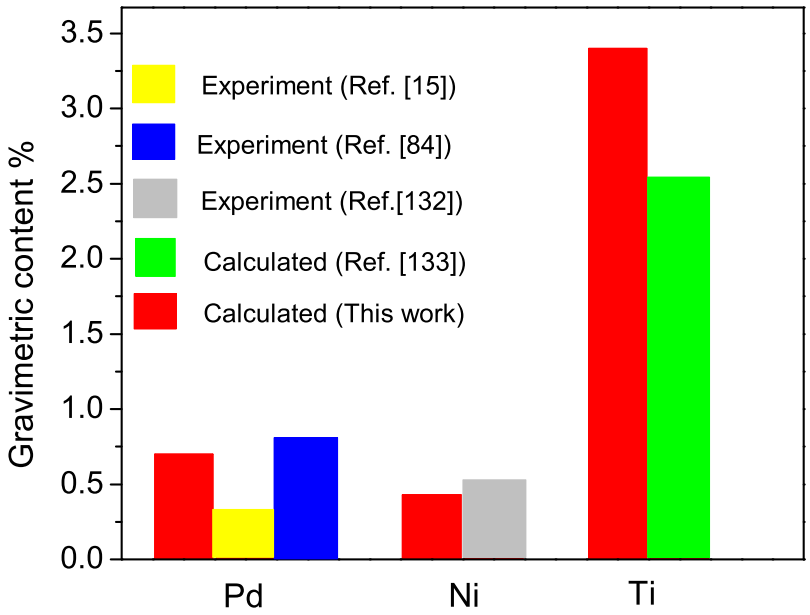

Figure 5.14: Comparison of calculated and experimental values for the hydrogen gravimetric content of Ti-, Ni-, and Pd-doped graphene.

Notably, we calculated a gravimetric content of 3.4 wt % for the graphene supported Ti_4, which is larger than the 2.4 wt % value estimated by Mashoff and co-workers for Ti nanoislands assuming a 1:1 H_2:Ti ratio and an almost complete Ti coverage of the graphene sheet with small metal islands [133]. The considerably higher gravimetric content found for Ti_4-doped graphene (3.4 wt %) compared to the ones for Ni_4-doped graphene (0.30 wt %) and Pd_4-doped graphene (0.64 wt %) can be explained by the fact that Ti is lighter than Ni and Pd, and it absorbs a larger amount H_2 per atom, and because the planar geometry which makes that all clusters atoms participate in the adsorption and increases the graphene sheet coverage.

Summary and Conclusions

In summary, the goal of this work is the study by means of density functional calculations the size dependence of the electronic, optical, and magnetic properties of GNFs with zigzag borders. Furthermore, motivated by the challenge to develop hydrogen storage materials for practical applications, we provide a detailed description of the interaction of H_2 with atomic and small Pd, Ni, and Ti clusters adsorbed on a defective graphene surface.

Thus, in the first part the geometrical and electronic properties of GNFs with zigzgag edges were studied in detail with the aim to identify the key factors determinating the energy gap and the spin density deistribution of the GNFs. Different graphene nanoestructures ranging from 1.0 to 7.0 nm were constructed and analyzed in detail. In particular the evolution of the Kohn-Sham energy gap, the sel-energy correction, the edge magnetism and the optical absorption as a fuction of size. In the second part large-scale periodic DFT calculations are performed to examine systematically the energetics and the hydrogen adsorption of Pd, Ni, and Ti clusters on graphene monovacancies.

This thesis has presented a number of new findings, as follows:

(i) Smaller hexagonal GNFs with zigzag borders have a nonmagnetic closed-shell ground state, however with the increasing of size (around 3 nm) the open-shell antiferromagnetic ground state emerges.

(ii) We have found that the origin of metallic behavoir predicted for zigzag GNFs at 6 nm in previous works is not related with the well known band gap problem of Kohn-Sham scheme, but with the absence electron-electron interactions due to spin polarization.

(iii) The size dependence of fundamental energy gap obtained within the quasiparticle formalism, predicts that even hexagonal GNFs of 10 nm are semiconducting with energy gaps around 0.5 eV, in contrast with previous calculations.

(iv) Based on the present results, we proposed that the metallic behavoir observed in the experiment for GNFs larger than 6 nm can be attributed to substrate effects like gap renormalization, the shifting of Fermi level self-doping or chemical interaction between the top-most surface atoms and graphene carbon atoms.

(v) Magnetic edge states do not exhibit influence on the π-plasmon energy in GNFs.

(vi) We found result is the formation of a spin-collinear domain wall (SCDW) for the 12-circumacene (n=12).

(vii) A detailed analysis of the results for larger circumacenes (n=12,13) shows that the ground state of larger circumacenes is the ferromagnetic one with a total magnetic

moment M=4 μ_B, But the energetic difference between FM and AFM state is only of 15 meV. This energetic difference can be tuned up to 47 meV increasing the width of nanoestructure, which may enables the utilization of these nanoestructures as spin logic devices at room temperature.

(viii) The results about hydrogen adsorption, shows that the Pd clusters supported on graphene monovacancies are able to attach up H_2 molecules covalently, forming dihydrogen complexes, most importantly with moderate binding energies, within the ideal energy range for efficient cyclic adsorption/desorption at room temperature and moderate pressures (0.2-0.6 eV/H_2).

(ix) Because to the large atomic mass of Pd, the gravimetric content of H_2 is limited to approximately 0.7%, atomic clusters of lighter elements such as Ni or Ti were proposed to resolve this issue. The maximum theoretical gravimetric content of H_2 for $Ni_4(H_2)_3$/defective graphene has been estimated to be 0.30 wt %, while that for Ti_4 on defective graphene was 3.4 wt %, which is significantly larger than the one predicted for Ni_4 and Pd_4 clusters. The better performance of Ti_4 clusters is related to the fact that Ti is a ligther transition metal and absorbs a larger amount of H_2 per metal atom.

(x) The present results indicates that controlled introduction of defects in graphene together within the anchoring of small transition-metal clusters is a feasible way to enhanced the hydrogen gravimetric content in graphene systems.

Prospects and future work

The study of graphene nanoestructures is a relatively new area of research that continually evolves. A sinergy between theory and experiments is necesary to narrow he gap between fundamental science and applicattions. Computational modelling and density functional theory are a valuable tools to understand and give physical insigth about general trends. However, we are aware that there is still much work to do in this field. In this way, the analysis in this thesis can be extended to the study of the electronic structure of:

(i) Graphene nanoflakes with defective terminations.

(ii) Graphene nanoflakes with oxygen-containing functional groups like carbonyl, hydroxyl and epoxides, which are commonly synthesized.

(iii) Graphene nanoflakes supported on metallic surfaces.

By other side, in the case of hydrogen adsorption on graphene nanoestructures we can extend the study to:

(i) Interactions between hydrogen and supported atomic clusters of ligther metal atoms.

(ii) Thermal effects on the hydrogen adsorption/desorption process.

(iii) Hydrogen spillover mechanism.

(iv) Finally, hope that our study motivates future theoretical and experimental studies because it provides a descriptor (or template) toward the computational discovery and design of families of novel hydrogen storage materials.

Appendix A

Relaxed Structures for Gas Phase and Supported Pd_η Clusters

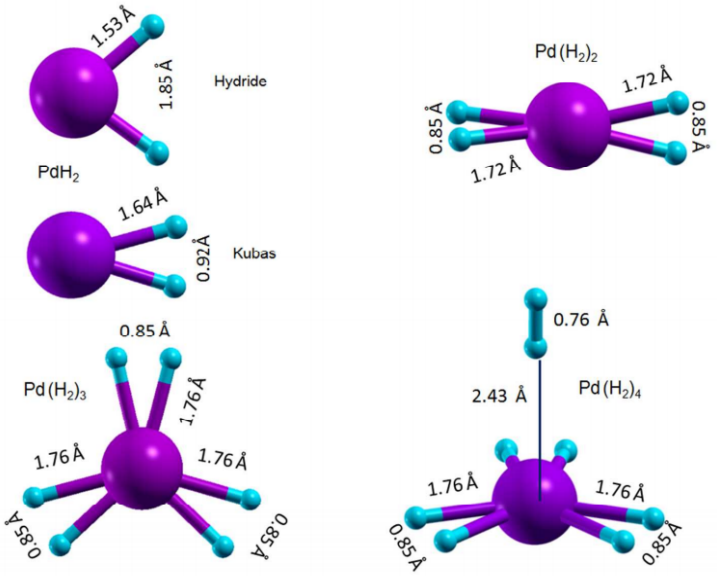

Figure A.1: Relaxed structures for the H_2 adsorption at the Pd atom in the gas phase, $Pd(H_2)_x$ with x=1-4 cluster.

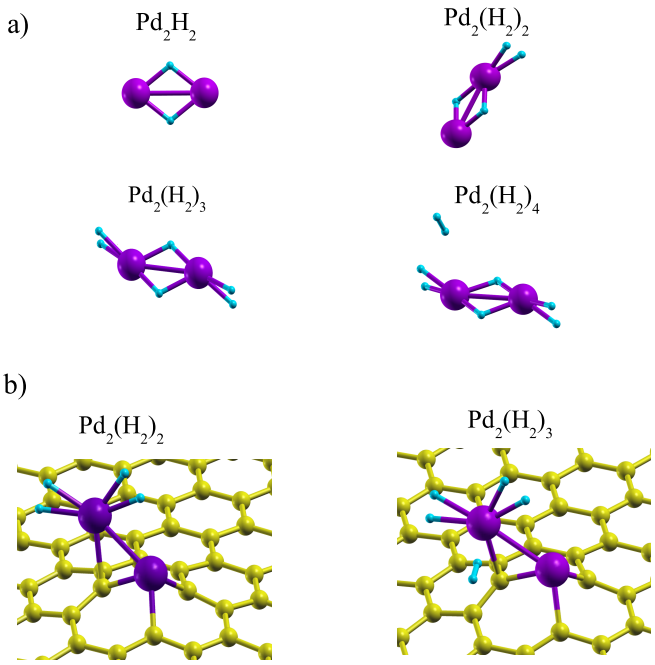

Figure A.2: a) Relaxed structures for the H_2 adsorption at Pd_2 cluster in the gas phase, Pd_2 $(H_2)_x$ with x=1-4 cluster, and for b) graphene anchored Pd_2 $(H_2)_x$ with x=2-3 cluster.

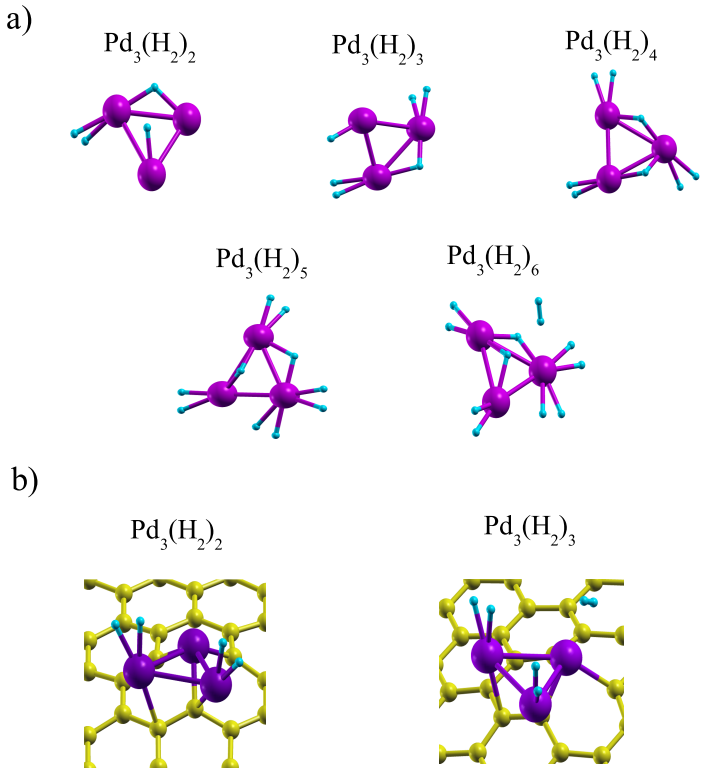

Figure A.3: a) Relaxed structures for the H_2 adsorption at the Pd_3 cluster in the gas phase, Pd_3 $(H_2)_x$ with x=1-6 cluster, and for b) graphene anchored Pd_3 $(H_2)_x$ with x=2-3 cluster.

Appendix B

Calculated Vibrational Frequencies for Selected Clusters.

Table B.1: Frequencies of the 3N-6 normal modes in cm^{-1} for the $Pd(H_2)_x$ clusters in gas phase.

$Pd(H_2)$	$Pd(H_2)_2$	$Pd(H_2)_3$	$Pd(H_2)_4$
Kubas	251.466	345.123	112.12
767.60	252.09	346.409	116.99
1658.86	680.97	386.49	175.69
2214.86	849.41	399.50	337.08
	1122.54	400.67	338.64
Hydride	1446.44	475.02	376.17
669.19	1446.68	843.70	376.67
2116.09	2846.47	844.44	396.81
2187.65	2874.24	1008.90	397.82
		1302.11	398.64
		1408.62	465.28
		1409.79	831.59
		2870.99	832.73
		2872.06	994.82
		2911.23	1274.64
			1379.78
			1380.55
			2892.21
			2892.61
			2930.41
			3976.14

Table B.2: Frequencies of the 3N-6 normal modes in cm^{-1} for the $Pd_2(H_2)_x$ (x=1-3) clusters in gas phase.

$Pd_2(H_2)$	$Pd_2(H_2)_2$	$Pd_2(H_2)_3$
72.48	187.72	114.73
206.33	199.91	154.91
1221.73	223.60	168.81
1332.06	236.49	189.69
1401.37	453.37	205.92
1523.77	884.07	206.46
	1129.91	434.42
	1314.68	523.64
	1325.74	812.85
	1397.72	880.58
	1552.64	1252.12
	3054.00	1281.60
		1288.36
		1387.88
		1491.45
		3183.64
		3186.29

Table B.3: Frequencies of the 3N-6 normal modes in cm^{-1} for the $Pd_3(H_2)_x$ (x=1-3) clusters in gas phase.

$Pd_3(H_2)$	$Pd_3(H_2)_2$	$Pd_3(H_2)_3$
101.58	40.48	59.94
140.83	131.71	101.70
192.76	135.92	122.44
255.85	151.27	134.73
462.95	225.99	166.17
1229.18	242.12	181.92
1296.87	445.67	188.04
1373.69	632.29	254.94
1410.06	677.52	284.28
	865.59	364.98
	909.36	580.17
	1187.84	798.99
	1277.86	824.88
	1451.84	1153.98
	2982.53	1204.68
		1253.71
		1320.86
		1582.43
		1651.18
		3058.28
		3187.37

Table B.4: Frequencies of the 3N-6 normal modes in cm^{-1} for the $Pd_4(H_2)$, $Pd_4(H_2)_2$, $Pd_4(H_2)_3$ and $Pd_4(H_2)_7$ clusters in gas phase.

$Pd_4(H_2)$	$Pd_4(H_2)_2$	$Pd_4(H_2)_3$	$Pd_4(H_2)_7$	
100.45	60.70	58.00	61.26	640.06
102.59	98.88	99.62	65.99	724.52
138.45	107.24	109.92	99.59	772.81
142.73	126.56	143.05	110.07	783.42
160.66	148.63	148.45	111.29	796.69
211.19	158.57	162.00	136.23	807.43
228.44	161.12	191.43	144.37	845.92
415.90	207.91	207.23	155.03	941.79
1192.46	246.69	225.38	163.83	970.68
1221.04	289.69	241.77	182.25	1064.59
1425.97	470.03	306.07	191.43	1087.96
1520.09	860.09	337.67	203.21	1146.20
	1118.61	372.37	217.03	1176.53
	1177.25	379.44	228.07	1186.52
	1372.35	537.04	240.94	1215.18
	1454.06	840.23	262.62	1230.50
	1552.19	861.58	273.63	1237.05
	2745.20	881.31	279.07	1287.11
		1363.51	292.94	2584.09
		1559.45	310.76	2907.87
		1619.37	334.48	3117.60
		1951.85	437.26	3165.70
		1977.09	442.59	3213.54
		2844.39	474.85	

Appendix C

Gravimetric Density Calculation Details

The general formula for gravimetric density of hydrogen is given in ref. [133].

$$GD = \frac{n_{H_2} m_{H_2} r_{TM-G}}{m_{TM}(r_{TM-G}/r) + m_C(\sigma_G/\sigma_{TM}) + n_{H_2} m_{H_2} r_{TM-G}} \times 100, \tag{C.1}$$

where the parameters are defined in the following manner:

m_{H_2}: Molecular mass of hydrogen.

m_C: Atomic mass of carbon.

m_{TM}: Atomic mass of transition metal atoms (Ti, Ni or Pd).

n_{H_2}: The average number of adsorbed hydrogen molecules per transition metal atoms in the cluster (0.75 for Ni_4, 1 for Pd_4 and 1.5 for Ti_4).

r: The fraction of TM atoms in contact with graphene surface (0.75 for Ni_4 and Pd_4 and 1 for Ti_4).

r_{TM-G}: The fraction of cluster-surface in contact with graphene-surface (0.25 for Ni_4 and Pd_4 and 1 for Ti_4).

σ_G: The surface atom density of graphene (around 38 atoms/nm^2).

σ_{TM}: The surface atom density of transition metal clusters, can be evaluated from the size and interatomic distances of supported clusters (around 3 clusters/nm^2).

Bibliography

[1] K.S. Novoselov, A.K. Geim, S.V. Morozov, D. Jiang, Y. Zhang, S.V. Dubonos, I.V. Grigorieva, and A.A. Firsov, *Electric Field Effect in Atomically Thin Carbon Films.* Science **306**, 666-669 (2004).

[2] A.K. Geim and K.S. Novoselov, *The Rise of Graphene.* Nature Mater. **6**, 183-191 (2007).

[3] A.K. Geim, *Graphene: Status and Prospects.* Science **324**, 1530-1534 (2009).

[4] A.H.C. Neto, F. Guinea, N.M.R. Peres, K.S. Novoselov, and A.K. Geim, *The Electronic Properties of Graphene.* Rev. Mod. Phys. **81**, 109-161 (2009).

[5] A.M. Silva, M.S. Pires, V.N. Freire, E.L. Albuquerque, D.L. Azevedo, and E.W.S. Caetano, *Graphene Nanoflakes: Thermal Stability, Infrared Signatures, and Potential Applications in the Field of Spintronics and Optical Nanodevices.* J. Phys. Chem. C **114**, 17472-17485 (2010).

[6] W. Hu, L. Lin, C. Yang, and J. Yang, *Electronic Structure and Aromaticity of Large-Scale Hexagonal Graphene Nanoflakes.* Chem. Phys. **141**, 214704-214714 (2014).

[7] Y. Son, M. Cohen, and S. Louie, *Energy gaps in Graphene Nanoribbons.* Phys. Rev. Lett. **97**, 216803-216806 (2006).

[8] V. Barone, O. Hod, and G. Scuseria, *Electronic Structure and Stability of Semiconducting Graphene Nanoribbons.* Nano Lett. **6**, 2748-2754 (2006).

[9] Y. Son, M. Cohen, and S. Louie, *Half-Metallic Graphene Nanoribbons.* Nature **444**, 347-349 (2006).

[10] T. Enoki, *Role of Edges in the Electronic and Magnetic Structures of Nanographene.* Phys. Scr. **T146**, 014008-01400822 (2012).

[11] G.Z. Magda, X. Jin, I. Hagymási, P. Vancso, Z. Osváth, P. Nemes-Incze, C. Hwang, L.P. Biró, and L. Tapasztó, *Room-Temperature Magnetic Order on Zigzag Edges of Narrow Graphene Nanoribbons.* Nature **514**, 608-611 (2014).

[12] J.M. Ogden, *Hydrogen: The Fuel of the Future*? Phys. Today **55**, 69-75 (2002).

[13] P. Jena, *Materials for Hydrogen Storage: Past, Present, and Future.* J. Phys. Chem. Lett. **2**, 206-211 (2011).

[14] P. Chen, X. Wu, J. Lin, and K. Tan, *High H_2 Uptake by Alkali-Doped Carbon Nanotubes Under Ambient Pressure and Moderate Temperatures.* Science **285**, 91-93 (1999).

[15] C.I. Contescu, K. van Benthem, S. Li, C.S. Bonifacio, S.J. Pennycook, P. Jena, and N.C. Gallego, *Single Pd Atoms in Activated Carbon Fibers and their Contribution to Hydrogen Storage.* Carbon **49**, 4050-4058 (2011).

[16] J. Li, T. Furuta, H. Goto, T. Ohashi, Y. Fujiwara, and S. Yip, *Theoretical Evaluation of Hydrogen Storage Capacity in Pure Carbon Nanostructures.* J. Chem. Phys. **119**, 2376-2385 (2003).

[17] Q. Sun, Q. Wang, P. Jena, and Y. Kawazoe, *Clustering of Ti on a C60 Surface and its Effect on Hydrogen Storage.* J. Am. Chem. Soc. **127**, 14582-14583 (2005).

[18] S.K. Bhatia and A.L. Myers, *Optimum Conditions for Adsorptive Storage.* Langmuir **22**, 1688-1670 (2006).

[19] H. Kroto, J. Heath, S. O'Brien, R. Curl, and R. Smalley, *C60: Buckminster-Fullerene.* Nature **318**, 162-163 (1985).

[20] S. Iijima, *Helical Microtubules of Graphitic Carbon*, Nature **354**, 56-58 (1991).

[21] K. Nakada, M. Fujita, G. Dresselhaus, and M. S. Dresselhaus, *Edge state in graphene ribbons: Nanometer size effect and edge shape dependence.* Phys. Rev. B **54**, 17954-17962 (1996).

[22] R. Saito, G. Dresselhaus, and M.S. Dresselhaus, *Physical Properties of Carbon Nanotubes.* Imperial College Press, (1998).

[23] S.D. Sharma, S. Adam, E.H. Hwang, and E. Rossi, *Electronic Transport in Two-Dimensional Graphene.* Rev. Mod. Phys. **83**, 407-469 (2011).

[24] C. Lee, X.D. Wei, J.W. Kysar, and J. Hone, *Measurement of The Elastic Properties and Intrinsic Strength of Monolayer Graphene.* Science **321**, 385-388 (2008).

[25] A.A. Balandin, *Thermal Properties of Graphene and Nanostructured Carbon Materials.* Nature Mater. **10**, 569-581 (2011).

[26] K.S. Novoselov, V.I. Falko, L. Colombo, P.R. Gellert, M.G. Schwab, and K. Kim, *A Roadmap for Graphene.* Nature **490**, 192-200 (2012).

[27] Y.M. Lin, C. Dimitrakopoulos, K.A. Jenkins, D.B. Farmer, H.Y. Chiu, A. Grill, and P. Avouris, *100-GHz Transistors from Wafer-Scale Epitaxial Graphene.* Science **327**, 662-667 (2010).

[28] M. Liu, X. B. Yin, E. Ulin-Avila, B.S. Geng, T. Zentgraf, L. Lu, F. Wang, and X. Zhang, *A Graphene-Based Broadband Optical Modulator.* Nature **474**, 64-67 (2011).

[29] K.S. Kim, Y. Zhao, H. Jang, S.Y. Lee, J.M. Kim, K.S. Kim, J.Y. Ahn, P. Kim, J.Y. Choi, and B.H. Hong, *Large-Scale Pattern Growth of Graphene Films for Stretchable Transparent Electrodes.* Nature **457**, 706-710 (2009).

[30] M.F. El-Kady, V. Strong, S. Dubin, and R.B. Kaner, *Laser Scribing of High-Performance and Flexible Graphene-Based Electrochemical Capacitors.* Science **335**, 1326-1330 (2012).

[31] M. Terrones, A.R. Botello-Mendez, J. Campos-Delgado, F. López-Urias, Y.I. Vega-Cantu, F.J. Rodriguez-Macias, A.L. Elias, E. Muñoz-Sanoval, A.G. Cano-Marquez, J.C. Charlier, and H. Terrones, *Graphene and Graphite Nanoribbons: Morphology, Properties, Synthesis, Defects and Applications.* Nano Today **5**, 351-372 (2010).

[32] R.E. Peierls, *Remarks on Transition Temperatures.* Helv. Phys. Acta **7**, 81-83 (1934).

[33] R.E. Peierls, *Some Properties of Solids.* Ann. Inst. Henri Poincare **5**, 177-222 (1935).

[34] L.D. Landau, *Zur Theorie der Phasenumwandlungen II.* Phys. Z. Sowjetunion, **11**, 26-35 (1937).

[35] N.D. Mermin and H. Wagner, *Absence of Ferromagnetism or Antiferromagnetism in One- or Two-Dimensional Isotropic Heisenberg Models.* Phys. Rev. Lett. **17**, 1133-1136 (1966).

[36] N.D. Mermin, *Crystalline Order in Two Dimensions.* Phys. Rev. **176**, 250-252 (1968).

[37] A. Fasolino, J.H. Los, and M.I. Katsnelson, *Intrinsic Ripples in Graphene.* Nature Mater. **6**, 858-861 (2007).

[38] P.R. Wallace, *The Band Theory of Graphite.* Phys. Rev. **71**, 622-634 (1947).

[39] G.W. Semenoff, *Condensed Matter Simulation of a Three-dimensional Anomaly.* Phys. Rev. Lett. **53**, 2449-2452 (1984).

[40] K.S. Novoselov, A.K. Geim, S.V. Morozov, D. Jiang, M.I. Katsnelson, I.V. Grigorieva, S.V. Dubonos, and A.A. Firsov, *Two-dimentional Massless Dirac Fermions in Graphene.* Nature **438**, 197-200 (2005).

[41] Y. Zhang, Y.W. Tan, H.L. Stormer, and P. Kim, *Experimental Observation of the Quantum Hall Effect and Berry's Phase in Graphene.* Nature **438**, 201-204 (2005).

[42] A.J. van Bommel, J.E. Crombeen, and A. van Tooren, *LEED and Auger Electron Observations of the SiC(0001) Surface.* Surface Science **48**, 463-472 (1974).

[43] Y. Gamo, A. Nagashima, M. Wakabayashi, M. Terai, and C. Oshima, *Atomic Structure of Monolayer Graphite Formed on Ni(111).* Surface Science **374**, 61-64 (1997).

[44] F. Himpsel, K. Christmann, P. Heimann, D. Eastman, and P.J. Feibelman, *Adsorbate Band Dispersions for C on Ru(0001).* Surface Science **115**, 159-164 (1982).

[45] R. Rosei, M. De Crescenzi, F. Sette, C. Quaresima, A. Savoia, and P. Perfetti, *Structure of Graphitic Carbon on Ni(111): A Surface Extended-Energy-Loss Fine-structure Study.* Phys. Rev. B **28**, 1161-1164 (1983).

[46] N. Kholin, E. Rut'kov, and A. Tontegode, *The Nature of the Adsorption Bond Between Graphite Islands and Iridium Surface.* Surface Science **139**, 155-172 (1984).

[47] C. Berger, Z. Song, T. Li, X. Li, A.Y. Ogbazghi, R. Feng, Z. Dai, A.N. Marchenkov, E.H. Conrad, P.N. First, and W.A. de Heer, *Ultrathin Epitaxial Graphite: 2D Electron Gas Properties and a Route toward Graphene-based Nanoelectronics.* J. Phys. Chem. B **108**, 19912-19916 (2004).

[48] M.I. Katsnelson, K.S. Novoselov, and A.K. Geim, *Chiral Tunnelling and the Klein Paradox in Graphene.* Nature Phys. **2**, 620-625 (2006).

[49] K.I. Bolotin, F. Ghahari, M.D. Shulman, H.L. Stormer, and P. Kim, *Observation of the Fractional Quantum Hall Effect in Graphene.* Nature Phys. **462**, 196-199 (2009).

[50] T.M. Rusin and W. Zawadzki, *Zitterbewegung of Electrons in Graphene in a Magnetic Fields.* Phys. Rev. B **78**, 125419-125426 (2008).

[51] P. Miró, M. Audiffred, and T. Heine, *An Atlas of Two-Dimensional Materials.* Chem. Soc. Rev. **43**, 6537-6554 (2014).

[52] H.S.P. Wong and D. Akinwande, *Carbon Nanotubes and Graphene Devices Physics.* Cambridge University Press, First Edition (2011).

[53] J. Wu, W. Pisula, and K. Müllen, *Graphene as Potential Material for Electronics.* Chem. Rev. **107**, 718-747 (2007).

[54] L. Zhi and K. Müllen, *A Bottom-Up Approach from Molecular Nanographenes to Unconventional Carbon Materials.* J. Mat. Chem. **18**, 1472-1484 (2008).

[55] M. Terrones, *Nanotubes Unzipped.* Nature **458**, 845-846 (2009).

[56] M. Han, B. Ozyilmaz, Y. Zhang, and P. Kim, *Energy Band Gap Engineering of Graphene Nanoribbons.* Phys. Rev. Lett. **98**, 206805-206809 (2007).

[57] S. Stankovich, D.A. Dikin, G.H. Dommett, K.M. Kohlhaas, E.J. Zimney, E.A. Stach, R.D. Piner, S.T. Nguyen, and R.S. Ruoff, *Graphene-based Composite Materials* Nature **442**, 282-286 (2006).

[58] L. Chen, Y. Hernandez, X. Feng, and K. Müllen, *From Nanographene and Graphene Nanoribbons to Graphene Sheets: Chemical Synthesis.* Angew. Chem. Int. Ed. **51**, 7640-7654 (2013).

[59] C. Simpson, J. Brand, A. Berresheim, L. Przybilla, H. Räder, and K. Müllen, *Synthesis of a Giant 222 Carbon Graphite Sheet.* Chem. Eur. J. **8**, 1424-1429 (2002).

[60] S. Hämäläinen, Z. Sun, M. Boneschanscher, A. Uppstu, M. Ijäs, A. Harju, D. Vanmaekelbergh, and P. Liljeroth, *Quantum-Confined Electronic States in Atomically Well-Defined Graphene Nanostructures.* Phys. Rev. Lett. **107**, 236803-236806 (2011).

[61] J. Bardeen, *Surface States and Rectification at a Metal-Semiconductor Contact.* Phys. Rev. **71**, 717-727 (1947).

[62] Z. Chen, Y. Lin, M. Rooks, and P. Avouris, *Graphene-Nanoribbon Electronics.* Physica E **40**, 228-232 (2007).

[63] X. Li, X. Wang, L. Zhang, S. Lee, and H. Dai, *Chemically Derived, Ultrasmooth Graphene Nanoribbon Semiconductors.* Science **319**, 1229-1232 (2008).

[64] S. Adam, S. Cho, M. Fuhrer, and S. Das Sarma, *Density Inhomogeneity Driven Percolation Metal-Insulator Transition and Dimensional Crossover in Graphene Nanoribbons.* Phys. Rev. Lett. **101**, 046404-046410 (2008).

[65] M. Fujita, K. Wakabayashi, K. Nakada, and K. Kusakabe, *Peculiar Localized State at Zigzag Graphite Edge.* J. Phys. Soc. Jpn. **65**, 1920-1923 (1996).

[66] F. Sols, F. Guinea, and A. Castro-Neto, *Coulomb Blockade in Graphene Nanoribbons.* Phys. Rev. Lett. **99**, 166803-166806 (2007).

[67] D. Querlioz, *Suppression of the Orientation Effects on Bandgap in Graphene Nanoribbons in the Presence of Edge Disorder.* Appl. Phys. Lett. **92**, 42108-42111 (2008).

[68] D. Gunlycke, D. Areshkin, and C.T. White, *Semiconducting Graphene Nanostrips with Edge Disorder.* Appl. Phys. Lett. **90**, 142104-142107 (2007).

[69] K.A. Ritter and J.W. Lyding, *The Influence of Edge Structure on the Electronic Properties of Graphene Quantum Dots and Nanoribbons.* Nature Mat. **8**, 235-242 (2009).

[70] R. Nair, M. Sepioni, I. Tsai, O. Lehtinen, J. Keinonen, A.V. Krasheninnikov, T. Thomson, A.K. Geim, and I.V. Grigorieva, *Spin-Half Paramagnetism in Graphene Induced by Point Defects.* Nature Phys. **8**, 199-202 (2012).

[71] P. Esquinazi, D. Spemann, R. Höhne, A. Setzer, K.H. Han, and T. Butz, *Induced Magnetic Ordering by Proton Irradiation in Graphite.* Phys. Rev. Lett. **91**, 227201-227204 (2003).

[72] L. Chen, L. Guo, Z. Li, H. Zhang, J. Lin, J. Huang, S. Jin, and X. Chen, *Towards Intrinsic Magnetism of Graphene Sheets with Irregular Zigzag Edges.* Sci. Rep. **3**, 2599-2605 (2013).

[73] W.L. Wang, S. Meng, and E. Kaxiras, *Graphene Nanoflakes with Large Spin.* Nano Lett. **8**, 241-245 (2008).

[74] O.V. Yazyev, W.L. Lang, S. Meng, and E. Kaxiras, *Comment on Graphene Nanoflakes with Large Spin: Broken-Symmetry States.* Nano Lett. **8**, 766 (2008).

[75] W.L. Wang, O.V. Yazyev, S. Meng, and E. Kaxiras, *Topological Frustration in Graphene Nanoflakes: Magnetic Order and Spin Logic Devices.* Phys. Rev. Lett. **102**, 157201-157203 (2009).

[76] E. Lieb, *Two Theorems on the Hubbard Model.* Phys. Rev. Lett. **62**, 1201-1204 (1989).

[77] A.S. Barnard and I.K. Snook, *Thermal stability of graphene edge structure and graphene nanoflakes.* J. Chem. Phys. **128**, 094707-094714 (2008).

[78] Z.Z. Zhang, K. Chang, and F.M. Peeters, *Tuning of Energy Levels and Optical Properties of Graphene Quantum Dots.* Phys. Rev. B **77**, 235411-235419 (2008).

[79] Targets for Onboard Hydrogen Storage Systems for Light-Duty Vehicles, revision 4.0; Technical report produced by the US Department of Energy, Office of Energy Efficiency and Renewable Energy, and the FreedomCAR and Fuel Partnership: Washington, DC, September 2009. http://energy.gov/sites/prod/files/2014/03/f11/targets onboard hydro storage explanation.pdf.

[80] P.A. Thrower and R.M. Mayer, *Point Defects and Self-Diffusion in Graphite.* Phys. Status Solidi A **47**, 11-37 (1978).

[81] A. Dillon, K.M. Jones, T.A. Bekkedahl, C. Kiang, D.S. Bethune, and M.J. Heben, M.J., *Hydrogen Storage in Single-Walled Carbon Nanotubes at Room Temperature.* Nature **386**, 377-379 (1997).

[82] C. Liu, Y.Y. Fan, M. Liu, H.T. Cong, H.M. Cheng, and M.S. Dresselhaus, *Nanotubes at Room Temperature Hydrogen Storage in Single-Walled Carbon.* Science **286**, 1127-1129 (1999).

[83] V. Tozzini, and V. Pellegrini, *Prospects for Hydrogen Storage in Graphene.* Phys. Chem. Chem. Phys. **15**, 80-89 (2013).

[84] V. Bhagavathi, P. Rupali, N.K. Sethupathi, and S. Ramaprabhu, *Investigation of Spillover Mechanism in Palladium Decorated Hydrogen Exfoliated Functionalized Graphene.* J. Phys. Chem. C **115**, 15679-15685 (2011).

[85] H. Lee, J. Ihm, M.L. Cohen, and S.G. Louie, *Calcium-Decorated Graphene-Based Nanostructures for Hydrogen Storage.* Nano Lett. **10**, 793-798 (2010).

[86] G.J. Kubas, *Molecular Hydrogen Complexes: Coordination of Sigma Bond to Transition Metals.* Acc. Chem. Res. **21**, 120-128 (1988).

[87] P. Power, *Main-Group Elements as Transition Metals.* Nature **463**, 171-177 (2010).

[88] P. Krasnov, F. Ding, A.B. Singh, and B.I. Yakobson, *Clustering of Sc on SWNT and reduction of hydrogen uptake: ab-initio all-electron calculations.* J. Phys. Chem. C **111**, 17977-17980 (2007).

[89] K.T. Chan, J.B. Neaton, and M.L. Cohen, *First-Principles Study of Metal Adatom Adsorption on Graphene.* Phys. Rev. B **77**, 235430-235442 (2008).

[90] G. Kim, S.H. Jhi, S. Lim, and N. Park, *Effect of Vacancy Defects in Graphene on Metal Anchoring and Hydrogen Adsorption.* Appl. Phys. Lett. **94**, 173102-172105 (2009).

[91] A.V. Krasheninnikov, P.O. Lehtinen, A.S. Foster, P. Pyykko, and R.M. Nieminen, *Embedding Transition-Metal Atoms in Graphene: Structure, Bonding, and Magnetism.* Phys. Rev. Lett. **102**, 126807-126810 (2009).

[92] M.J. López, I. Cabria, S. Fraile, and J.A. Alonso, *Adsorption and Dissociation of Molecular Hydrogen on Palladium Clusters Supported on Graphene.* J. Phys. Chem. C **116**, 21179-21198 (2012).

[93] M.J. López, I. Cabria, and J.A. Alonso, *Palladium Clusters Anchored on Graphene Vacancies and Their Effect On the Reversible Adsorption of Hydrogen.* J. Phys. Chem. C **118**, 5081-5090 (2014).

[94] H. Valencia, A. Gil, and G. Frapper, *Trends in the Hydrogen Activation and Storage by Adsorbed 3d Transition Metal Atoms onto Graphene and Nanotube Surfaces: A DFT Study and Molecular Orbital Analysis.* J. Phys. Chem. C **119**, 5506-5522 (2015).

[95] S. Grimme, J. Antony, S. Ehrlich, and H. Krieg, *A Consistent and Accurate Ab-initio Parametrization of Density Functional Dispersion Correction (DFT-D) for the 94 elements H-Pu.* J. Chem. Phys. **132**, 154104-154111 (2010).

[96] Y.H. Zhang, L.J. Yue, L.F. Han, J.L. Chen, S.M. Fang, D.Z. Jia, and F. Li, *Tuning the Magnetic Behavior and Transport Properties of Graphene by Introducing Dopant and Defect: A First Principle Study.* Comput. Theor. Chem. **972**, 63-67 (2011).

[97] J.J. Palacios and F. Yndurain, *A Critical Analysis of Vacancy-Induced Magnetism in Mono and Bilayer Graphene.* Phys. Rev. **40**, 3616-3624 (2012).

[98] J. Medina, R. de Coss, A. Tapia, and G. Canto, *Structural, Energetic and Magnetic Properties of Small Ti_n (n = 1-13) Clusters: a Density Functional Study.* Eur. Phys. J. B **76**, 427-433 (2010).

[99] J. Harman, J. Wu, S. Wei, H.C. Kang, and E. Soon, *Graphene-Adsorbed Fe, Co, and Ni Trimers and Tetramers: Structure, Stability, and Magnetic Moment.* Phys. Rev. B **83**, 205408205415 (2011).

[100] M. Born, and J.R. Oppenheimer, *Zur Quantentheorie der Molekeln.* Annalen der Physik **389**, 457-484 (1927).

[101] P. Hohenberg and W. Kohn, *Inhomogeneous Electron Gas.* Phys. Rev. **136**, 864-871 (1964).

[102] W. Kohn and L. Sham, *Self-Consistent Equations Including Exchange and Correlation Effects.* Phys. Rev. **140**, 1133-1138 (1965).

[103] K. Burke. *Perspective on Density Functional Theory.* Chem. Phys. **136**, 150901-150910 (2012).

[104] R.W. Godby and L.D. White, *Density-Relaxation Part of the Self-energy.* Phys. Rev. Lett. **80** 3161-3164 (1998).

[105] L. Hedin, *One-Particle Green's Function with Application to the Electron-Gas Problem.* Phys. Rev. **139**, 796-802 (1965).

[106] E.K.U. Gross, J.F. Dobson, and M. Petersilka, in *Density Functional Theory.* Edited by R.F. Nalewajski (Springer-Verlag, Berlin, 1996), p. 81.

[107] M.E. Casida, in *Recent Advances in Density-Functional Methods.* Edited by D. P. Chong (World Scientific, Singapore, 1995), Pt. I, p. 155.

[108] J.M Soler, E. Artacho, J.D. Gale, A. García, J. Junquera, P. Ordejón, and D. Sánchez-Portal, J. Phys.: Condens. Matter. **14**, 2745-2779 (2002).

[109] D.M. Ceperley and B.J. Alder, *Ground State of the Electron Gas by a Stochastic Method.* Phys. Rev. Lett. **45**, 566-569 (1980).

[110] J.P. Perdew, K. Burke, and M. Ernzerhof, *Generalized Gradient Approximation Made Simple.* Phys. Rev. Lett. **77**, 3865-3869 (1996).

[111] S.G. Louie, S. Froyen and, M.L. Cohen, *Nonlinear Ionic Pseudopotentials in Spin-density-Functional Calculations.* Phys. Rev. B **26**, 1738-1742 (1982).

[112] M. Troulliers and J.L. Martins, *Efficient Pseudopotentials for Plane-Wave Calculations.* Phys. Rev. B **43**, 1993-1999 (1991).

[113] D. Vanderbilt, *Soft Self-Consistent Pseudopotentials in a Generalized Eigenvalue Formalism.* Phys. Rev. B **41**, 7892-7895 (1990).

[114] J. Junquera, O. Paz, D. Sánchez-Portal, and E. Artacho, *Numerical Atomic Orbitals for Linear-Scaling Calculations.* Phys. Rev. B **64**, 235111-235116 (2001)

[115] H. Bethe, and E. Salpeter, *A Relativistic Equation for Bound-State Problems.* Phys. Rev. **84**, 1232-1236 (1951).

[116] V. Saunders and J. van Lenthe,*The Direct CI Method.* Mol. Phys. **48**, 923-954 (1983).

[117] S. Ögüt, S. Louie, and J. Chelikowsky, *Reply to Comment on Quantum Confinement and Optical gaps in Si Nanocrystals* Phys. Rev. Lett. **83**, 1270 (1997).

[118] S. Ögüt, S. Louie, and J. Chelikowsky, *Quantum Confinement and Optical Gaps in Si Nanocrystals.* Phys. Rev. Lett. **79**, 1770 (1997).

[119] P. Giannozzi, S. Baroni, N. Bonini, M. Calandra, R. Car, C. Cavazzoni, D. Ceresoli, G.L. Chiarotti, M. Cococcioni, I. Dabo, A. Dal Corso, S. Fabris, G. Fratesi, S. de Gironcoli, R. Gebauer, U. Gerstmann, C. Gougoussis, A. Kokalj, M. Lazzeri, L. Martin-Samos, N. Marzari, F. Mauri, R. Mazzarello, S. Paolini, A. Pasquarello, L. Paulatto, C. Sbraccia, S. Scandolo, G. Sclauzero, A. P. Seitsonen, A. Smogunov, P. Umari, and R.M. Wentzcovitch, *QUANTUM ESPRESSO: a modular and open-source software project for quantum simulations of materials.* J. Phys.: Condens. Matter. **21**, 395502 (2009).

[120] D. Rocca, R. Gebauer, Y. Saad, and S. Baroni, *Turbo Charging Time-Dependent Density-Functional Theory with Lanczos Chains.* J. Chem. Phys. **128**, 154105-154119 (2008).

[121] E. Koch and A. Otto, *Optical absorption of benzene vapour for photon energies from 6 eV to 35 eV.* Chem. Phys. Lett. **12**, 476-480 (1972).

[122] J.B. Neaton, M.S. Hybertsen, and S.G. Louie, *Renormalization of Molecular Electronic Levels at Metal-Molecule Interfaces.* Phys. Rev. Lett. **97**, 216405-216410 (2006).

[123] C. Delerue, M. Lannoo, and G. Allan, *Excitonic and Quasiparticle Gaps in Si Nanocrystals* Phys. Rev. Lett. **84**, 2457-2460 (2000).

[124] R. Fukuda, and M. Ehara, *Theoretical Study on the Excited Electronic States of Coronene and Its π-Extended Molecules Using the Symmetry-Adapted Cluster-Configuration Interaction Method.* Bulletin of the Chemical Society of Japan **86**, 445-451 (2013).

[125] M. Bendikov, F. Wudl, and D.F. Perepichka, *Tetrathiafulvalenes, oligoacenenes, and their buckminsterfullerene derivatives: The brick and mortar of organic electronics.* Chem. Rev. **104**, 4891-4945 (2004).

[126] S. S. Zade and M. Bendikov, *Heptacene and beyond: the longest characterized acenes.* Angew. Chem. **122**, 4104-4107 (2010)

[127] M.M. Payne, S.R. Parkin, and J.E. Anthony, *Functionalized higher acenes: hexacene and heptacene.* J. Am. Chem Soc. **127**, 8028-8037 (2005).

[128] C.A. Ullrich, *Time-dependent Density-Functional Theory Beyond the Adiabatic Approximation: Insights from a Two-Electron Model System.* J. Chem. Phys. **125**, 234108-23116 (2006).

[129] D. Chae, T. Utikal, S. Weisenburger, H. Giessen, K. Klitzing, M. Lippitz, and J. Smet, *Excitonic Fano Resonance in Free-Standing Graphene.* Nano Lett. **11**, 1379-1382 (2011).

[130] C.M. Ramos-Castillo, J.U. Reveles, R.R. Zope, and R. de Coss, *Palladium Clusters Supported on Graphene Monovacancies for Hydrogen Storage.* J. Phys. Chem. C **119**, 8402-8409 (2015).

[131] A. Granja, J.A. Alonso, I. Cabria, and M.J. López, *Competition Between Molecular and Dissociative Adsorption of Hydrogen on Palladium Clusters Deposited on Defective Graphene.* RSC Adv. **5**, 47945-47953 (2015).

[132] M. Gaboardi, A. Bliersbach, G. Bertoni, M. Aramini, G. Vlahopoulou, D. Pontiroli, P. Mauron, G. Magnani, G. Salviati, A. Zuttel, and M. Ricco, *Decoration of Graphene with Nickel Nanoparticles: Study of the Interaction with Hydrogen.* J. Mater. Chem. A **2**, 1039-1046 (2014).

[133] T. Mashoff, D. Convertino, V. Miseikis, C. Coletti, V. Piazza, V. Tozzini, F. Beltram, and S. Heun, *Increasing the Active Surface of Titanium Islands on Graphene by Nitrogen Sputtering.* Appl. Phys. Lett. **106**, 083901-083905 (2015).

[134] C.M. Ramos-Castillo, J.U. Reveles, M.E. Cifuentes-Quintal, R.R. Zope, and R. de Coss, *Ti_4- and Ni_4-Doped Defective Graphene Nanoplatelets as Efficient Materials for Hydrogen Storage.* J. Phys. Chem. C **120**, 5001-5009 (2016).